TIME-VARIABILITY AND PRIMORDIAL BLACK HOLE EVAPORATION: ASTROPHYSICAL NEUTRINO STUDIES

A Dissertation
Presented to
The Academic Faculty

By

Pranav Mayank Dave

In Partial Fulfillment
of the Requirements for the Degree
Doctor of Philosophy in the
School of Physics

Georgia Institute of Technology

May 2023

TIME-VARIABILITY AND PRIMORDIAL BLACK HOLE EVAPORATION: ASTROPHYSICAL NEUTRINO STUDIES

Thesis committee:

Dr. Ignacio Taboada
School of Physics
Georgia Institute of Technology

Dr. Nepomuk Otte
School of Physics
Georgia Institute of Technology

Dr. David Ballantyne
School of Physics
Georgia Institute of Technology

Dr. Carlos Argüelles-Delgado
Department of Physics
Harvard University

Dr. John Wise
School of Physics
Georgia Institute of Technology

Date Approved: April 18, 2023

There is stardust in your veins. We are literally, ultimately children of the stars.

Jocelyn Bell Burnell

To gazing at the stars and wondering

ACKNOWLEDGEMENTS

This journey began by reading Stephen Hawking's 'A Brief History of Time' in high school, so firstly I would like to thank the multitude of scientists who make it possible for laymen to understand the complexities of this incredible universe we live in. I am forever indebted to the Physics Department at UMass Dartmouth and Georgia Tech for giving me the opportunity to learn and contribute to astrophysics. To my physics professors, Prof. Gaurav Khanna, Prof. Robert Fisher, Prof. J. P. Hsu, Prof. Brian Kennedy, Prof. Andrew Zangwill, and many more from whom I learned the importance of presenting complex, technical material in a clear and engaging way. I would also like to thank all my wonderfully curious undergraduate students that I had the opportunity to teach and learn from over the years as a TA, at UMass Dartmouth and Georgia Tech.

To my present and past group members here at Georiga Tech, namely Dr. Dirk Lennarz, Dr. Chris Tung, Dr. Chujie Chen, Hannah Griggs, and Bennett Brinson, among others for providing helpful suggestions and feedback in all areas of my life, as well as for providing comedic relief and making our day-to-day lives more fun. I would also like to thank my fellow IceCube colleagues, Dr. Will Luszszak, Dr. Lisa Schumacher, Dr. Hans Niederhausen, and Prof. Juanan Aguilar for their help in developing and reviewing `TAUNTON`. To Ivan Martinez-Soler, Dr. Kayla Leonard, and Prof. Carlos Pérez de los Heros for their constructive feedback and support for my PBH work.

Lastly, but most importantly, I would like to thank my advisor Prof. Ignacio Taboada. Without his generosity and patience over the past 7 years, this work would not be possible. Thank you for guiding me and helping me grow as a person. To my parents, Dr. Mayank Dave and Mrs. Bina Dave, thank you for inspiring and supporting me through the years. Thank you to my sister, Dr. Jui Dave, for being a role model and pushing me when needed. Thank you, Anna, for your dedication and sacrifice. Words cannot express the depth of my gratitude.

TABLE OF CONTENTS

LIST OF TABLES

LIST OF FIGURES

SUMMARY

Our current understanding of the universe stems from observations across the electromagnetic spectrum as well as additional messengers, such as gravitational waves, cosmic rays, and neutrinos. Notably, in 2013, the data collected by the IceCube detector at the geographic South Pole revealed a diffuse astrophysical flux of high-energy neutrinos [1]. After more than 12 years of operation, the class of sources that contribute to this diffuse neutrino flux is not known, mainly due to the significant challenges associated with reconstructing neutrino arrival directions and limited statistics. However, most recently in 2022, IceCube reported evidence of neutrino emission from NGC 1068, a nearby AGN and Seyfert II galaxy, using 8.7 years of observational data [2]. This time-integrated excess of 79^{+22}_{-20} neutrino events coincide spatially with NGC 1068 and are energetic and abundant enough to be identified over the expected background, provides a unique opportunity to ask: Is NGC 1068 a time-variable neutrino source? In this dissertation, `TAUNTON` , a new method to test for the time-variability of candidate neutrino sources is presented. As a non-parametric method, `TAUNTON` establishes if neutrino data are consistent with a steady time hypothesis. By applying `TAUNTON` on this 8.7-year sample, we can conclude that if NGC 1068 is a real neutrino source, IceCube data best describes it as a steady source. This method supplements IceCube's existing flare search methods that utilize a smaller background to identify a neutrino flare.

Hawking radiation elegantly unifies general relativity, quantum field theory, and thermodynamics. Primordial Black Holes (PBHs) formed due to density fluctuations in the early universe can offer a direct test of Hawking radiation. As the hole loses mass, $-dM/dt \propto 1/M^2$, over the age of the universe and evaporates, it can produce an observable burst in neutrinos and γ-rays among other elementary particles. Currently, there is no evidence of Hawking radiation or PBHs. In this dissertation, a search for evaporating PBHs is presented using high-energy neutrino data collected by IceCube for the first time. As no

significant emission was found, upper limits were placed on the local PBH abundance at $170,342\ \mathrm{pc}^{-3}\mathrm{yr}^{-1}$ for a search window of 0.43 days. For reference, the strongest limit on the local PBH burst rate density from any existing electromagnetic measurement is by the HAWC collaboration at $3,400\ \mathrm{pc}^{-3}\mathrm{yr}^{-1}$ at 99% confidence for a search window of 1 second. These high-energy multi-messenger searches for emission from individual PBH bursts, at the $10^{-2}\ \mathrm{pc}$ scale, complement existing efforts to confirm Hawking radiation.

CHAPTER 1
INTRODUCTION AND BACKGROUND

For centuries, astronomers have relied on electromagnetic radiation to observe the cosmos. From visible and infrared light to X-rays and γ-rays, these forms of radiation have given us extraordinary insight into the present and past thermal and non-thermal universe. The thermal universe, referred to by observations of light from objects with a temperature, includes the observation of stars, galaxies, and the cosmic microwave background radiation that forms the afterglow of the Big Bang some 13.8 billion years ago. The non-thermal universe is dominated by other processes, such as the acceleration of high-energy particles by strong magnetic fields or shock waves. For instance, high-energy electrons spiraling around magnetic field lines emit synchrotron radiation that can be detected in radio up to X-ray wavelengths. This emission depends on the magnetic field strength and the energy of the electron and has been used to study a nearby supernova remnant. X-ray and γ-ray telescopes can detect radiation emitted by particles that have been accelerated to extremely high energies, such as in supernova explosions or near black holes. This includes observations of extremely luminous regions in the centers of galaxies, powered by accretion onto supermassive black holes called Active Galactic Nuclei (AGNs). By studying the non-thermal universe, we can explore the most violent cosmic events in extreme environments to understand and validate a wide range of fields in physics, including particle physics, general relativity, and cosmology, that are impossible to recreate in a laboratory environment on Earth.

In addition to traditional astronomy, we can also observe the non-thermal universe through the detection of high-energy particles such as cosmic rays, neutrinos, as well as gravitational waves. Cosmic rays are high-energy atomic nuclei and subatomic particles that originate from outside our solar system, but their exact origins have remained a mys-

tery. These cosmic rays have been observed for over a century since confirmation by balloon flight experiments. In 2017, a large-scale anisotropy was reported in their arrival directions above $8\ \mathrm{EeV} = 1.28\ \mathrm{J}$ energy[1] indicating that the highest-energy cosmic rays are of extra-galactic origin [3]. Neutrinos, which are produced in the same astrophysical processes as cosmic rays, can travel vast distances without being absorbed or deflected by magnetic fields. Gravitational waves, which are tests of general relativity, have a similar property of being observable through intervening material. While cosmic rays suffer from this absorption and deflection, neutrinos and gravitational waves do not; modern technology and recent breakthroughs have now allowed for the detection of astrophysical neutrinos and gravitational waves. For instance, on 14th September 2015, the first direct detection of gravitational waves from the merger of two black holes of masses $35\ \mathrm{M}_\odot \mathrm{and}\ 30\ \mathrm{M}_\odot$ by the LIGO and Virgo collaborations tested general relativity in the strong-field regime [4]. On August 17, 2017, a binary neutrino star merger was observed in gravitational waves (GW170817) along with a prompt burst in γ-rays (GRB 170817A) [5]. We now enter the era of multi-messenger astronomy that allows us to add to our knowledge of the non-thermal universe.

A breakthrough in 2013 confirmed a novel approach to astronomy that relies on neutrinos to observe the non-thermal universe. Despite the challenges of conducting scientific research in such a remote and hostile environment at the geographic South Pole, IceCube has detected high-energy $\gtrsim \mathrm{TeV}$ neutrinos of extra-terrestrial origin [1], referred to as the diffuse astrophysical neutrino flux. Neutrinos are extremely light $\lesssim \mathrm{eV}$, subatomic particles that interact weakly with matter so the km^3 size of the IceCube detector allows for detection of these elusive particles at high-energies $\gtrsim \mathrm{GeV}$. In fact, on 23rd February 1987, a galactic supernova SN 1987A 51.4 kpc away provided the first confirmation of an extra-terrestrial neutrino source. These neutrinos were detected by several experiments around the world, including the Kamiokande II detector in Japan [6] and the IMB (Irvine-

[1] Equivalent to the kinetic energy attained by tossing a tennis ball

Michigan-Brookhaven) detector in the United States [7]. This is because $\sim 10^{58}$ neutrinos with a total energy of 10^{53} erg are expected to be produced in a few seconds following a supernova explosion. This burst of MeV neutrinos was observed approximately 2-3 hours before the visible light from the supernova reached Earth, and although only 19 neutrinos (out of $\sim 10^{28}$ that passed through the Earth) were observed during the event, it was a significant increase over the expected background. This landmark event has shaped our current understanding of core-collapse supernovae as this provided us with the first (and only so far) direct evidence of a supernova driven by the collapsing core of a dying star [8] [9]. The detection implied that there had been a proto-neutron star in existence for at least 10 seconds and declared the dawn of neutrino astronomy.

One of the many possibilities with neutrino astronomy is its potential to solve the long-standing mystery of the exact origins of cosmic rays. On 22nd September 2017, a highly energetic neutrino (~ 290 TeV) was detected by the IceCube experiment (dubbed IC170922A [10]), indicating its probable origin to be astrophysical in nature. Due to IceCube's automated alert systems that notified numerous telescopes across the globe within minutes, it was discovered that the blazar TXS 0506+056 (5.7 billion light-years away) exhibited increased emission in high and very high energy gamma rays. This detection of a neutrino coincident with a gamma-ray emitting blazar, while it was in an active phase, implied that blazars could potentially be a source of high-energy neutrinos. A time-dependent archival search in this direction with IceCube data revealed a 13 ± 5 neutrino excess over a 110-day period, prior to IC170922A, in 2014-2015 [11]. However, it was found that the diffuse astrophysical flux observed by IceCube can be accommodated by a sub-class of blazars[2] like TXS 0506+056 only up to $\sim 5\%$ [12]. This suggests that identifying the sources that produce this diffuse flux will be challenging and we do not yet know much about the class of sources that produces this diffuse flux.

Most recently in 2022, IceCube reported direct evidence of TeV neutrino emission

[2]That episodically produce neutrinos with the luminosity of the 2014 flare

from the nearby[3] AGN, NGC 1068 [2]. This *time-integrated* excess of 79^{+22}_{-20} neutrinos was observed using 8.7 years of data recorded from 2011-2020, in part by refining the data calibration and processing techniques, as well as improvements to the point-source search method used by IceCube. Interestingly, the inferred neutrino flux exceeds the potential γ-ray flux by at least one order of magnitude. Because the connection between neutrinos and γ-rays depends on the astrophysical environment, this suggests that γ-rays are heavily obscured around this AGN's core. The supermassive black hole located at the center of NGC 1068 enables the acceleration of high-energy particles that can produce neutrinos. In addition, X-ray photons are generated through a process called photon Comptonization from the accretion disk's hot plasma located above the disk, which is also known as the corona [13, 14, 15, 16]. This corona provides the necessary conditions for the production of neutrinos. However, at the same time, the plasma can be optically dense to γ-rays leading to suppression in their flux. Even though NGC 1068 is one of the closest and most well-studied galaxies across the electromagnetic spectrum, the observed neutrino emission has opened up new avenues in our understanding of AGNs, specifically NGC 1068 .

A natural follow-up question to the NGC 1068 neutrino emission arises: Is this emission time-variable or is NGC 1068 a steady source? Now that IceCube has two candidate neutrino sources, it is not obvious how to answer this question as there is some evidence for both, flaring and steady emission. In this dissertation, I present a new method, `TAUNTON` , that helps characterize current and future neutrino sources observed by IceCube. This characterization of the time-variability of neutrino sources using IceCube data is detailed in Chapter 6. By applying this method to the same 8.7-year data sample that identified evidence from NGC 1068 , `TAUNTON` concludes that the neutrino emission from NGC 1068 is consistent with a steady source. Other than the Sun in our solar system, this method establishes NGC 1068 as the first extra-terrestrial neutrino point source that can be expected to produce more observable neutrinos in the future. Additionally, this method supplements

[3] 14.4 Mpc away

the flare-search methods employed by IceCube as it gathers more data and identifies other objects in our universe as neutrino sources.

While IceCube has just begun to identify sources that contribute to the observed astrophysical diffuse flux, in this dissertation, I use high-energy neutrino data collected by IceCube to consider Stephen Hawking's proposal in 1974 that black holes (BHs) can radiate, lose mass, and eventually, *evaporate* [17]. Hawking radiation allows for the production of every particle in the standard model of particle physics in the vicinity of the BH, depending on its temperature or mass. This radiation causes an accelerating mass loss, $-dM/dt \propto 1/M^2$, and can be observable as the BH evaporates. A consequence of this mass loss is that black holes formed in the early universe, commonly referred to as primordial black holes (PBHs), can evaporate over the age of the universe. There is no current evidence to support the existence of Hawking radiation or PBHs. Additionally, dark matter (DM), estimated to constitute 85% of the matter in our universe, has been another long-standing mystery of modern astrophysics and PBHs have been previously considered to be DM candidates [18]. Various searches for Hawking radiation from PBHs have significantly constrained the fraction of DM that can be explained PBHs in our local universe. Alternatively, searches for nearby evaporating PBHs or individual PBHs have also been conducted using γ-ray telescopes. In particular, the High-Altitude Water Cherenkov (HAWC) observatory, has the strongest upper limit on the evaporating PBH abundance in our local universe: $3400\ \mathrm{pc}^{-3}\mathrm{yr}^{-1}$ at 99% confidence for a 1-second search window [19]. In this dissertation, I present a search for nearby evaporating PBHs in the northern celestial sky, $\delta > -5^\circ$, where IceCube's sensitivity to point sources is optimal. By predefining null-detection in this search, this method constrains the local PBH abundance to $170,342\ \mathrm{pc}^3\mathrm{yr}^{-1}$ at 99% confidence for a 0.43 day search window.

This dissertation is organized as follows. In Ch. 2, I provide a brief overview of particle astrophysics that is relevant to neutrino astronomy. In Ch. 3, I detail Hawking radiation from evaporating PBHs and how it can allow for a time-and-energy dependent neutrino

flux at Earth. In Ch. 4, I review neutrino physics and the detection principles of current and future neutrino detectors that can contribute to neutrino astronomy. In Ch. 5, I provide an overview of the IceCube detector as well as the methods used to create and analyze high-purity data samples used in this dissertation. In Ch. 6, I introduce the time-variability test, `TAUNTON` along with its performance for generic time-variability and present the results of applying this test to select sources in two data samples collected by IceCube, including NGC 1068. In Ch.7, I detail the time-dependent search for evaporating PBHs using the calculations in Ch. 3 on another sample collected by IceCube along with the results and discussion about the limits. In Ch.8, I conclude and present an outlook for neutrino astronomy.

CHAPTER 2
PARTICLE ASTROPHYSICS

2.1 Cosmic-rays

2.1.1 Introduction

Ionizing radiation observed on the Earth's surface was originally believed to come from radioactive γ-radiation in the planet's crust until Victor Hess showed the increasing levels of radiation with altitude aboard an atmospheric balloon in 1912 [20]. A 100 years after this legendary experiment was carried out, we know that cosmic rays are high-energy particles coming from outside the solar system with energies ranging from GeV - 100 EeV. While the composition of cosmic rays (CR) varies with energy, they are mainly dominated by hydrogen and helium nuclei.

There are several interesting and challenging questions that remain to be answered regarding cosmic rays: What is their spatial distribution in the sky? What are their sources? Which astrophysical environments allow them to accelerate to such a wide range of energies? How are these environments different or similar to other cosmic messengers (neutrinos, gravitational waves, photons)? How do they interact with the intergalactic magnetic fields and background radiation? What is the composition of cosmic rays at the highest energies? In order to address these questions, we first need to look at the cosmic-ray spectrum and the physical mechanisms which allow the production of high-energy cosmic rays.

2.1.2 Spectrum & Possible Sources

The energy spectra for several messengers are shown in Fig. 2.1, as measured by a variety of instruments, and the all-particle CR spectrum has some interesting features. The most dominant species are protons ($\sim 90\%$) and heavier nuclei, and the shape of its spec-

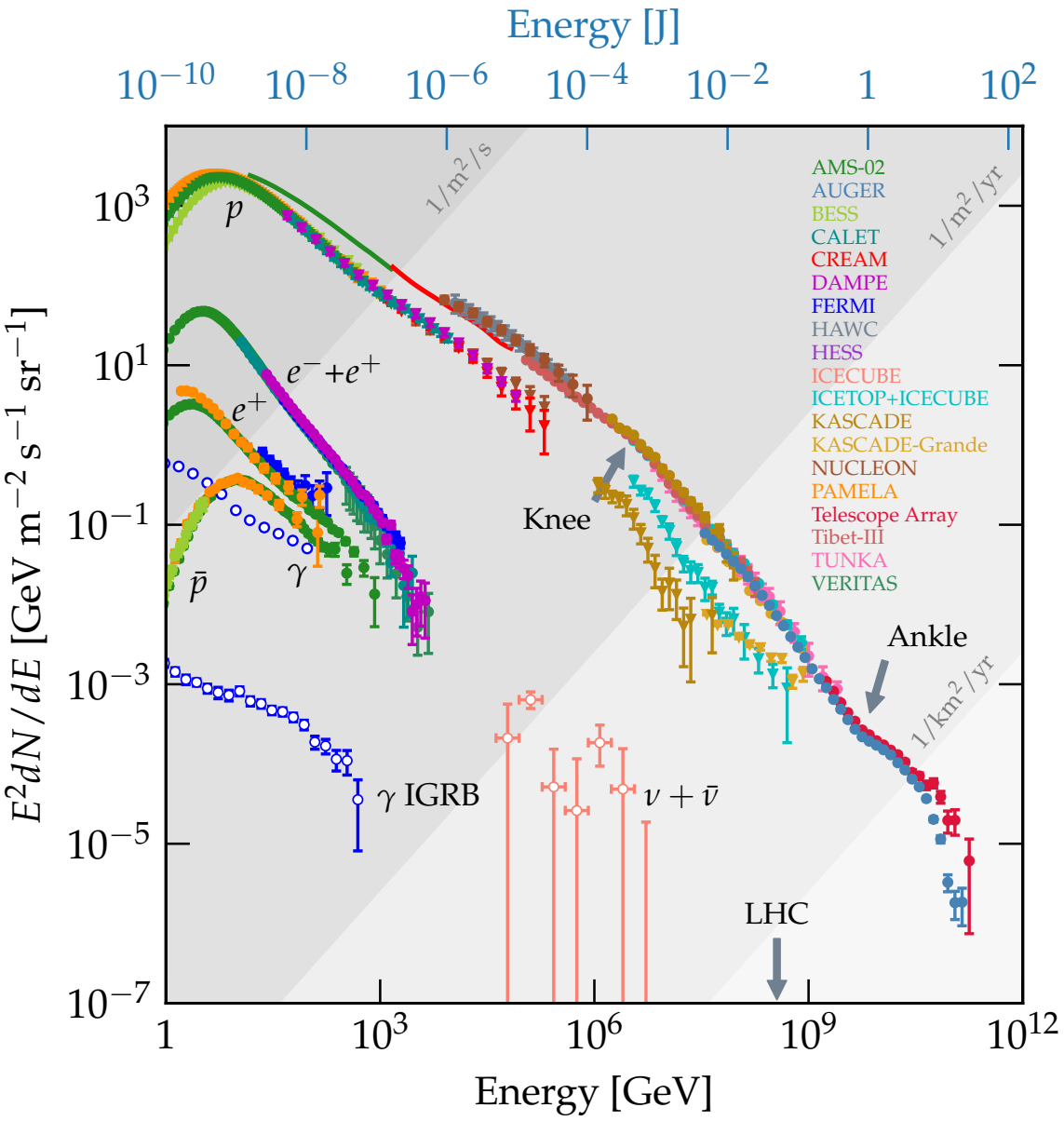

Figure 2.1: Energy spectrum, E^2dN/dE, of various cosmic messengers by a variety of instruments, including air-shower experiments as well as observatories deployed in space as described in the legend. This includes measurements of the isotropic diffuse γ-ray background by Fermi and astrophysical neutrino flux by IceCube. Reference rates of $EdN/dE = 1\ \mathrm{m}^{-2}\mathrm{s}^{-1}$, $1\ \mathrm{km}^{-2}\mathrm{s}^{-1}$, $1\ \mathrm{km}^{-2}\mathrm{yr}^{-1}$ are displayed as diagonal lines using a multiplicative factor: $E^2dNdE/4\pi$. This figure was created using an online repository of measurements and code [21].

trum has been of particular interest and the different features are under active investigation. Above a few GeV, the energy spectrum follows a power-law of the form $E^{-\gamma}$, such that the differential spectral index, γ, lies between 2.7 and 3.3. Suppression at the highest energies ($\gtrsim 50$ EeV) is attributed to either attenuation from the cosmic-microwave background (CMB) photons via pion photoproduction ($p + \gamma \rightarrow \Delta^+$) or a limit to the maximum energy at particle acceleration sites. The Δ^+ then decays into $p + \pi^0$ or $n + \pi^+$ and the resulting p or n lose energy as the pions decay further into γ-rays, muons, and neutrinos. As shown in Fig. 2.1, two changes to this slope occur around ~ 5 PeV (knee) and ~ 5 EeV (ankle) across the wide range of energies.

Our current understanding of the knee in the CR spectrum is that perhaps protons cannot be accelerated to higher energies beyond $\gtrsim 5$ PeV by galactic accelerators, since for instance a supernova remnant can only accelerate a proton upto a PeV [22]. That is given that a galactic accelerator can accelerate a proton up to maximum energy, $E_{\max}$, then for iron $Z = 26$ that would be $26 \cdot E_{\max}$ so more energetic comic-rays have to be heavier nuclei. This prediction can be checked by measuring the composition as a function of energy near the knee. The spectral hardening before the ankle is attributed to extragalactic sources since the radius of curvature for charged particles in our galaxy would be smaller than the distance to the galactic center:

$$\frac{R_L}{1\,\mathrm{kpc}} \simeq \frac{E/1\mathrm{EeV}}{B/1\mu\mathrm{B}} \tag{2.1}$$

Without going into the details of the acceleration mechanism, we can ask the question: What kind of sources can sufficiently contain and accelerate a cosmic ray up to 100 EeV? In order to effectively accelerate a charged particle, the size of the acceleration site, L, must be at least of the order of its Larmor radius, r_L:

$$L \geq r_L = \frac{pc}{ZeBc} \tag{2.2}$$

This relation is called the Hillas criterion since it places an upper bound on the maximum attainable energy of a cosmic ray, given the typical radius and magnetic field of the acceleration site. For instance, a supernova remnant (SNR) with a typical magnetic field of 30μG and size of 1 pc, can maximally accelerate a cosmic-ray upto 30 PeV since more energetic cosmic rays cannot be contained within the acceleration site. This is demonstrated for a range of astrophysical environments in Fig. 2.2. Note that besides containment, a valid acceleration site must have an effective acceleration mechanism which allows acceleration for the observed cosmic ray energies.

2.1.3 Acceleration Mechanism

Accelerating charged particles to ultra-relativistic energies poses an interesting theoretical challenge. In order to explain the CR spectrum, this acceleration mechanism must allow for the following features:

- A power-law energy spectrum of the form: $dN(E) \propto E^{-\Gamma} dE$, where $2 \lesssim \Gamma \lesssim 3$
- Acceleration of cosmic rays to 100 EeV energies
- Consistent with cosmic ray chemical abundance given the cosmic abundance of elements

In 1949, Enrico Fermi proposed a stochastic mechanism whereby a charged particle gains energy by repeated reflections from magnetic interstellar clouds [24]. This results in a 2nd order average energy gained per collision: $\left\langle \frac{\Delta E}{E} \right\rangle \propto (v/c)^{-2}$, where v and c are the speed of the cloud and particle respectively. While the resultant energy spectrum does follow a power-law, the mechanism is too slow in low density clouds and fails to satisfy the observed cosmic-ray spectrum [25, 26, 27]. Finally, in 1978, A. R. Bell formulated this diffusive shock acceleration mechanism which utilized the Fermi mechanism in first order [28, 29].

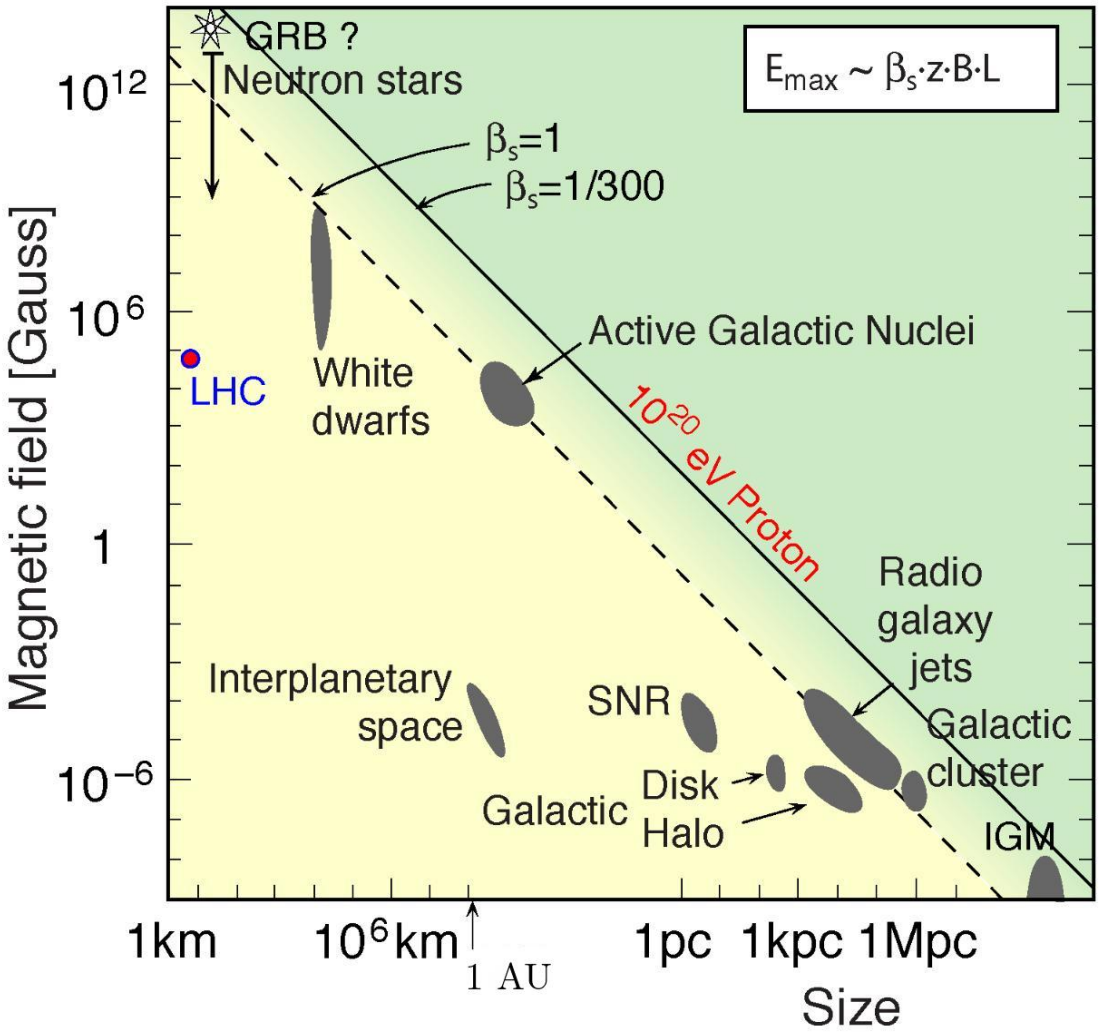

Figure 2.2: The 'Hillas' plot which constrains the maximum acceleration energy of a cosmic ray by $E_{\max} \propto \beta_s z B L$, where β_s is the effeciency, L the size, and B the magnetic field of the acceleration site. Z is the absolute value of the charge of the particle. The solid and dashed line correspond to maximum acceleration upto 100 EeV of a proton for a perfectly efficient ($\beta_s = 1$) and typical efficiency of $\beta_s = 1/300$. Larger, low B acceleration or a compact, high B accelerator can satisfy this constraint as demonstrated. This figure is taken from [23].

A shock is a discontinuity in temperature and mass density, either due to mass-energy interaction (deflagration or detonation) or high-speed collision between ejecta and the ambient medium. In the presence of strong shocks, a charged particle can gain energy to the first order by crossing the shock front. This type of acceleration mechanism is called first-order Fermi acceleration. In order to describe this process, let $E = E_0\beta^k$ be the energy of a charged particle after k collisions and P be the probability that the particle remains in the acceleration zone after one collision, such that the number of particles after k collisions are $N = N_0P^k$. Note that $\beta > 1$ for positive energy gain and $P < 1$ to allow for the possibility of the charged particle escaping. Eliminating k, we get:

$$\frac{N}{N_0} = \left(\frac{E}{E_0}\right)^{\ln P/\ln \beta} \tag{2.3}$$

Then

$$\frac{N}{N_0} = \left(\frac{E}{E_0}\right)^{-\alpha} \Rightarrow \frac{dN}{dE} \propto \left(\frac{E}{E_0}\right)^{-\gamma}, \tag{2.4}$$

$$\text{since} \qquad \alpha = -\ln P/\ln \beta \simeq \frac{1-P}{\beta - 1};\ \gamma = \alpha + 1 \tag{2.5}$$

For a supersonic shock in monoatomic gas, α is predicted to be 1 by the kinetic theory of gases. Consequently, the differential energy spectrum, γ can be found to be 2. However, the detected energy spectrum at Earth is steeper since the probability that the particle escapes is higher at higher energies:

$$\left|\frac{dN}{dE}\right|_{\text{Earth}} \propto \left(\frac{dN}{dE}\right)_{\text{source}} \times E^{-\delta} \propto \left(\frac{E}{E_0}\right)^{-\gamma-\delta} \tag{2.6}$$

This escape parameter, δ, can be estimated using measured ratios of primary to secondary cosmic rays to be $0.3 - 0.6$. Therefore, first order Fermi acceleration explains the general characteristics of the observed cosmic ray spectrum.

2.2 Neutrino and Gamma-ray Production

Neutrinos and gamma-rays point back to their source for identification, unlike cosmic-rays, and they can all have an overlap of sources which is valuable in this era of multimessenger astronomy. While photons cannot be directly accelerated, high-energy photons can be produced in radiative or collisional processes of high-energy charged particles. Consequently, high-energy photons can be produced by purely leptonic models (synchrotron, inverse compton) of production and as secondary products of hadronic interaction ($pp,\ p\gamma$). This section will cover the hadronic interaction models for high-energy neutrino and gamma-ray production.

2.2.1 Proton-nucleon collisions (pp interaction)

In this beam dump process, let's assume a beam of protons collides with a molecular cloud or interstellar material at energies much higher than the pion mass. The particles interact with each other or undergo decay repeatedly until their energy levels fall below the threshold for further interactions, leaving decay as the only possible outcome. Consequently, a particle shower develops that produces pions and kaons, among other particles [30]. For pions, due to isospin symmetry, about the same number of $\pi^0,\ \pi^+,\ \pi^-$ are produced. Each π^0 decays into 2 gamma-rays, whereas the charged pions decay into a neutrino and muon, which further decays into a neutrino, antineutrino, and an electron. This results in 3 neutrinos per charged pion, or 3 neutrinos for every gamma-ray.

$$p + p \rightarrow N(\pi^0 + \pi^+ + \pi^-) + X \tag{2.7}$$

$$\pi^0 \rightarrow \gamma + \gamma \tag{2.8}$$

$$\pi^+ \rightarrow \mu^+ + \nu_\mu \rightarrow e^+ + \nu_e + \bar{\nu}_\mu + \nu_\mu \tag{2.9}$$

$$\pi^- \rightarrow \mu^- + \bar{\nu}_\mu \rightarrow e^- + \bar{\nu}_e + \nu_\mu + \bar{\nu}_\mu \tag{2.10}$$

This suggests a source flavor ratio of $N_{\nu_e} : N_{\nu_\mu} : N_{\nu_\tau} = 1 : 2 : 0$, but this could be suppressed for the electron neutrino flavor if the muon emits via synchrotron before it decays as on average it lasts longer than a pion [31]. Additionally, each neutrino on average has $1/4$ the energy of the pions as opposed to $1/2$ for the photons [23]. More importantly, high-energy neutrinos can be accompanied by very high-energy (VHE) γ-rays from such sites, only if the site is not opaque to these VHE γ-rays.

2.2.2 Photoproduction ($p\gamma$) interaction

For environments where the target photon density and cross-section are much higher than the matter density, this interaction becomes more important for a beam of protons. This happens mainly via the Δ resonance:

$$p + \gamma \to \Delta^+ \to p + \pi^0 \tag{2.11}$$

$$p + \gamma \to \Delta^+ \to n + \pi^+ \tag{2.12}$$

The cross-sections for the two processes are approximately $2 : 1$ in favor of the $p\pi^0$ channel. As we saw in the pp-channel, neutral pions decay to 2 gamma-rays and charged pions decay to 3 neutrinos. Additionally, this process occurs only beyond the threshold for producing a Δ^+, $4E_p\epsilon \gtrsim m_\Delta^2$, where ϵ is the energy of the target photons. Approximately, the energy of the gamma-rays produced is $E_\gamma \sim E_p/10$ and the energy of the resultant neutrinos is $E_\nu \sim E_p/20$. This relates the resultant neutrino to photon luminosities: $L_\nu/L_\gamma \sim 3/8$ since $3/4$ of the π^+ energy is deposited in neutrinos and $1/2$ of the π^0 energy is deposited in gamma rays.

If the site of production is optically thick or has dense material along the line of sight to Earth, neutrinos might not be accompanied by gamma rays. More interestingly, if the proton energy spectrum can be described by a power-law, an approximate relation can be

derived [23] between the neutrino and gamma-ray fluxes:

$$E_\nu^2 \frac{dN_\nu}{dE_\nu}(E_\nu) \sim \frac{3}{4}\, K\, E_\gamma^2 \frac{dN_\gamma}{dE_\gamma}(E_\gamma), \tag{2.13}$$

where $K = 2$ for pp-interaction and $K = 1/2$ for $p\gamma$-interaction.

2.3 Atmospheric Neutrinos

Cosmic-ray interactions in the atmosphere produce atmospheric neutrinos and muons. This collision of energetic protons and nuclei with the air molecules creates a cascade of secondary particles, which further interact, decay, or reach the ground. The atmospheric neutrino production below $\lesssim 100$ GeV is dominated by the charged pion decay: $\pi^+ \to \mu^+ + \nu_\mu \to e^+ + \nu_e + \nu_\mu + \bar{\nu}_\mu$. At higher energies, upto $\lesssim 100$ TeV, the contribution from kaon decay increases. At GeV energies, atmospheric neutrinos more or less follow the parent $E^{-2.7}$ cosmic ray spectrum. This is demonstrated in Fig. 2.3 for various experiments.

At the $\sim$ TeV energy, however, it has softened to $E^{-3.7}$ due to pion energy losses in the atmosphere. For kaon-induced neutrinos, the spectrum is similar at $\sim$ TeV energy. The flavor ratios for the conventional component favor the ν_μ channel heavily in energy range $\lesssim 100$ TeV [32]: $N_{\nu_e} : N_{\nu_\mu} : N_{\nu_\tau} = 1 : 19 : 0$. The energy spectra for this component are also a function of the zenith angle since the mesons in more inclined showers tend to decay rather than interact.

At energies $\gtrsim 10^5$ GeV, kaons are known to significantly attenuate and the decay from short-lived mesons ($D^0, D^\pm, D_s, \lambda_c$) dominates the channel for atmospheric neutrinos [33]. The flavor ratios in this prompt channel is: $N_{\nu_e} : N_{\nu_\mu} : N_{\nu_\tau} = 12 : 12 : 1$. Since the composition of cosmic-rays and small-χ QCD processes are relatively unknown, this semi-leptonic decay of charmed particles into prompt leptons involve large uncertainties in comparison to the conventional channel. These prompt neutrinos (or muons) have not been observed yet and is an active area of research in IceCube [34].

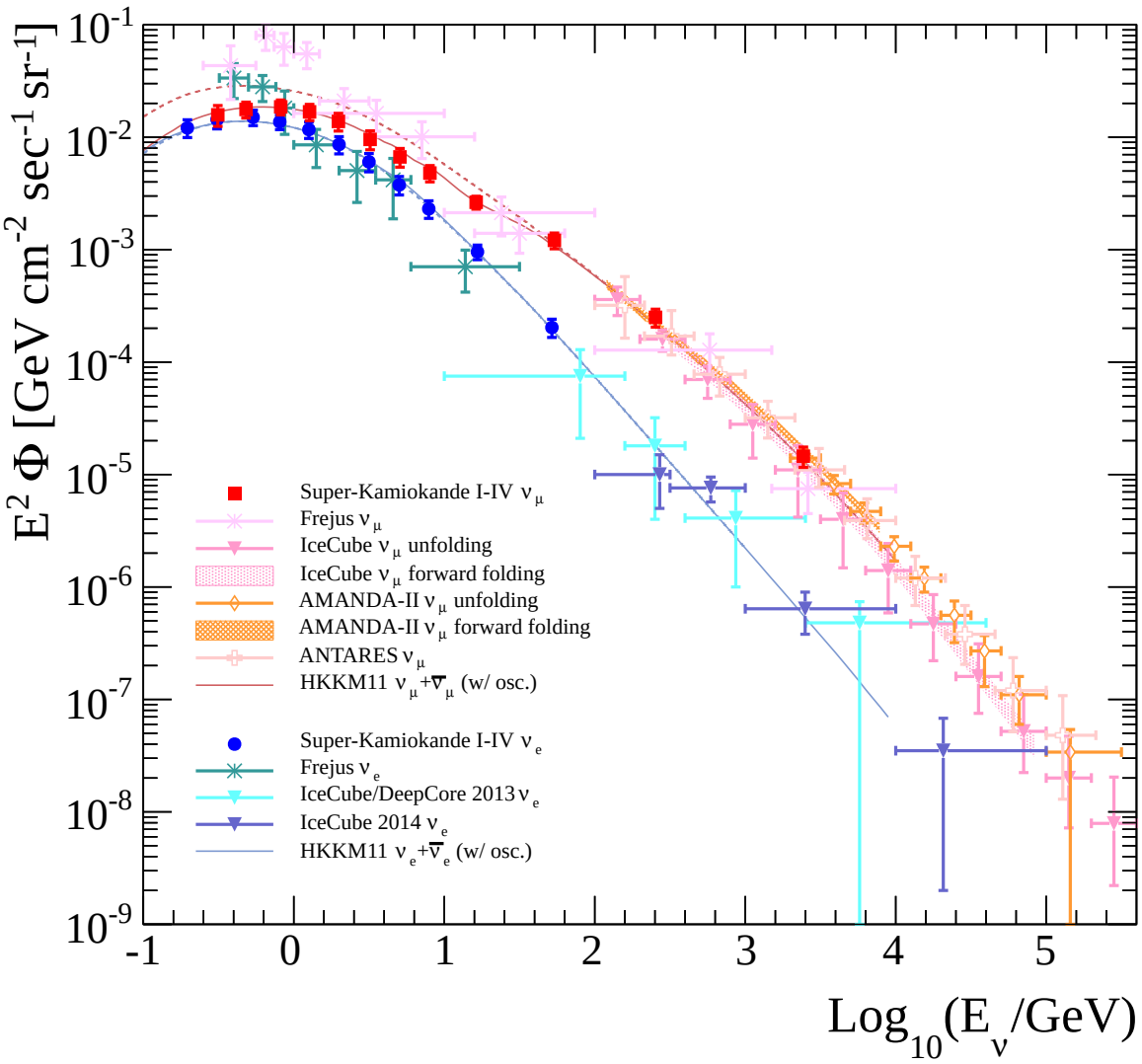

Figure 2.3: Atmospheric neutrino flux measured by various experiments as described in the legend. This figure is taken from [35].

2.4 Neutrino Sources and Outlook

Neutrinos as cosmic messengers provide a unique insight into the high-energy universe, providing the ability to point back to their source unlike cosmic rays, and providing information about the optically thick environments at cosmic accelerators. Additionally, not only are neutrinos produced in thermonuclear reactions that burn hydrogen to helium but also provide a way for the interior of a star to cool by transporting energy away from the core. We know neutrinos can be produced at the following sites:

1. Stars which generate thermonuclear energy, such as the Sun [36]
2. Neutron stars to provide cooling of astrophysical objects [37, 38]
3. Most violent phenomena including the Big Bang, supernovae, and Active Galactic Nuclei (AGNs) [39, 40, 41]
4. By-product of cosmic ray collisions either at the site of production or while propagating [41, 42]
5. Annihilation of dark matter particles or Hawking radiation from black holes [43, 17]

While IceCube is most sensitive to neutrinos in the TeV range, neutrino sources can emit over a wide range of energies; from cosmic background neutrinos at $\sim 10^{-2}$ eV to solar neutrinos upto a MeV, atmospheric neutrinos from cosmic ray air showers in the GeV - TeV range, to a blazar producing a 300 TeV neutrino [10]. More recently, neutrino production from Active Galactic Nuclei (AGNs) has been of interest due to evidence of time-integrated emission from NGC 1068 [2]. Due to the relevance of these studies to this dissertation, I shall briefly discuss AGNs in the context of neutrino sources to conclude this chapter, however AGNs themselves are an extremely rich and diverse set of objects. This diversity is commonly referred to as the AGN zoo. See [44] for a recent review of AGNs across the electromagnetic spectrum.

2.4.1 Active Galactic Nuclei (AGNs)

It is believed that supermassive black holes (SMBHs), $10^6\ \mathrm{M}_\odot \lesssim M_{\mathrm{BH}} \lesssim 10^{10}\ \mathrm{M}_\odot$, exist at the centers of most large galaxies including the Milky Way. The centers of these galaxies that are extremely luminous, $L_{\mathrm{bol}} \approx 10^{48}\ \mathrm{erg/s}$, are called Active Galactic Nuclei (AGNs). The accretion of matter onto SMBHs produces activity across the electromagnetic spectrum. Particularly, the Eddington limit provides the maximum luminosity of a star to balance the inward gravitational pull with the outward radiation pressure:

$$L_{\mathrm{edd}} = 1.38 \times 10^{38} \left(\frac{M_{\mathrm{BH}}}{\mathrm{M}_\odot} \right) \mathrm{erg/s} \tag{2.14}$$

The accretion of matter onto the SMBH has difficulty losing angular momentum and consequently forms an accretion disk. In $\sim 10\%$ of AGNs, this accretion process leads to the formation of collimated outflows of gas and radiation known as jets, which can extend for hundreds of thousands of light-years. The formation of these jets, perpendicular to the accretion disk, is believed to be due to the interaction between the accretion disk and a strong magnetic field. AGNs can be broadly classified based on their radiative efficiency L/L_{edd} and relativistic jet strength, along with identifying specific features in their spectral energy distributions (SED)[44]. In particular, the subset of AGNs where the jet is directly pointed towards Earth are called *blazars*. While this jet can provide the aforementioned beam dump to produce neutrinos, the disk can also provide a site for CR acceleration. In particular, for the disk-corona model for an AGN, the accretion disk itself is surrounded by a corona of hot, magnetized plasma. This corona can be the site of the cosmic-ray acceleration, that can produce neutrinos. The corona is believed to be responsible for the hard X-ray component of the AGN spectrum that is produced through a process known as Comptonization via upscattering of low-energy photons. Intense neutrino emission has been expected to be produced in AGN coronae once hadrons are accelerated together, as

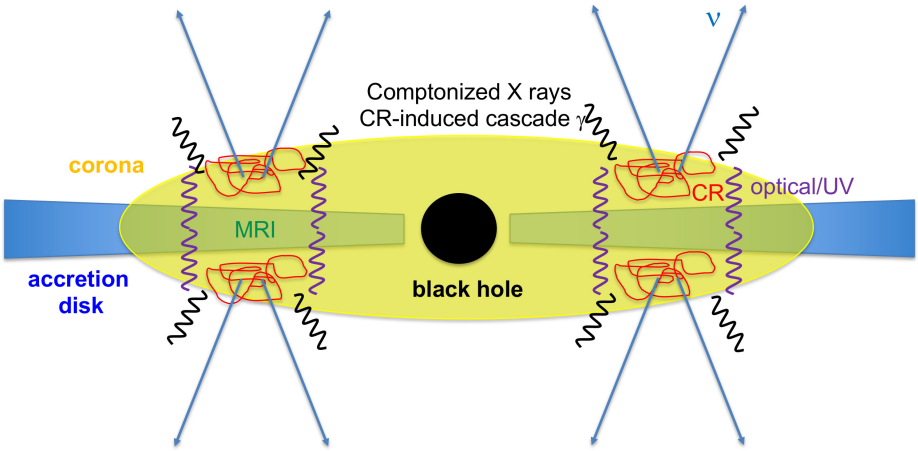

Figure 2.4: A schematic diagram of the disk-corona model for AGNs that allows for intense neutrino production in the vicinity of the disk. This figure is taken from [46].

shown as a schematic in Fig. 2.4. See [45] [46] for recent models that address neutrino production from the disk-corona model.

CHAPTER 3

NEUTRINOS FROM PRIMORDIAL BLACK HOLES

3.1 Introduction

The no-hair theorem postulates that black holes (BHs) can be described solely by their charge, angular momentum, and mass. In other words, a BH contains no information on how it reached a physically allowable charge, angular momentum, or mass. Stellar evolution allows the creation of BHs if the stellar remnant has a mass $\gtrsim 2-3\,M_{\odot}$ [40, 47]. Furthermore, we know supermassive BHs ($\sim 10^{6}-10^{10}\,M_{\odot}$) exist at the centers of massive galaxies [48] and their formation and evolution are active areas of research. BHs, across a wide range of masses, have been of considerable interest over the past century. Notably, in 1916, Karl Schwarzschild provided a spherically symmetric solution to the Einstein field equations describing the gravitational field of a point mass. This solution, referred to as a Schwarzschild BH, is a black hole that has neither electric charge nor angular momentum (spin). The Schwarzschild radius that defines the event horizon (containing the region of space that cannot affect any observer) is given by:

$$r_s = \frac{2GM}{c^2} \tag{3.1}$$

In 1974, Stephen Hawking proposed that thermal radiation due to quantum gravitational effects near the event horizon of a BH would cause it to lose mass [17]. The black hole temperature, which determines the instantaneous spectrum of Hawking radiation, and the remaining lifetime of the black hole are a function of the black hole's mass. Furthermore, the temperature of the black hole increases rapidly towards the end of the life of the black hole, leading to a burst in radiation. Consequently, black holes of initial mass $< 10^{15}$ g

would completely evaporate over the age of the universe. Fluctuations in the early universe could form such small black holes. Over the last decade, primordial black holes (PBHs) have been considered to be dark matter candidates. Assuming a narrow initial mass distribution, black holes can only be consistent with a dark matter hypothesis if they are in the ranges $10^{16} - 10^{17}$ g (asteroid mass scale); $10^{20} - 10^{24}$ g (sublunar mass scale) and $10 - 10^{3}$ $M_{\odot}$ (intermediate-mass black hole or IMBH) [18]. The latter mass range has recently received a lot of interest due to the unexpected detection of tens of solar mass black hole mergers by LIGO/VIRGO [4]. PBHs that have already evaporated have cosmological consequences, however, they do not contribute directly to currently existing dark matter. For broad initial mass distributions, PBHs with initial mass of $\sim 10^{15}$ g, that are currently evaporating, remain of interest [18]. Particularly, searches for emissions from *individual* PBH evaporation have been carried out by various experiments.

A recent study by Fermi-LAT [49] searched for GeV gamma rays from PBHs over their remaining months to a few years of existence when their mass had been reduced to $6 \times 10^{11}\,\mathrm{g}$. Because Fermi-LAT is sensitive to PBHs at a distance of ~ 0.03pc, the study took into account the proper motion of PBHs. Fermi LAT sets the local density rate for evaporating PBHs at $\dot{\rho} < 7.2 \times 10^{3}$ pc^{-3}yr^{-1} for a search duration of 1.26×10^{8} seconds. More recently, HAWC [19] placed the best limit at $\dot{\rho} < 3.4 \times 10^{3}$ pc^{-3} yr^{-1} for a burst in $> \mathrm{TeV}$ photons lasting 10 seconds. Milagro, the predecessor of HAWC, placed [50] an upper bound of $\sim\ 4 \times 10^{4}\,\mathrm{pc}^{-3}\mathrm{yr}^{-1}$ on the same time scale and energy as HAWC. Imaging Air Cherenkov Telescopes VERITAS [51] and H.E.S.S. [52] that operate in the $> 100\ \mathrm{GeV}$ range have also conducted searches and placed limits at $\sim 2 \times 10^{4}\,\mathrm{pc}^{-3}\mathrm{yr}^{-1}$ and $\sim 3 \times 10^{4}\,\mathrm{pc}^{-3}\mathrm{yr}^{-1}$ for the 30-second duration respectively.

3.2 Hawking Radiation

According to Hawking, the instantaneous rate of particle production, per spin (s) or helicity state, in the energy range $(E, E + dE)$ is given by [17, 53, 54]:

$$\frac{d^2N}{dEdt} = \frac{\Gamma}{2\pi\hbar}\left[\exp\left(\frac{E - n\hbar\Omega - e\phi}{\hbar\kappa/2\pi c}\right) - (-1)^{2s}\right]^{-1} \tag{3.2}$$

where $\Omega,\ \phi,\ \kappa$ are the angular momentum, electric potential, and the surface gravity of the BH respectively, while Γ and s are the absorption probability and spin of the emitted species. It has been shown that a BH would lose its spin and charge well before the remainder of the mass ($\sim M_i/10$) evaporates [55, 56] so we shall consider the chargeless, spinless case ($\Omega = 0,\ \phi = 0$). The surface gravity of the hole is simply $\kappa = GM/r_s^2$, where r_s is the Schwarzschild radius. Additionally, a temperature for the BH can be defined as $kT = \hbar c^3/8\pi GM$. Using these relations for a non-spinning chargeless BH, we can rewrite Eq. 3.2 as:

$$\frac{d^2N}{dEdt} = \frac{\Gamma}{2\pi\hbar}\left[\exp\left(\frac{E}{kT}\right) - (-1)^{2s}\right]^{-1} \tag{3.3}$$

Due to the inverse relation between the mass and temperature, the BH loses mass and accelerates its temperature rise, and one can use the emission rate to calculate the temperature of the BH as a function of the time remaining to evaporation, τ. This is demonstrated in Fig. 3.1 using `BlackHawk`, which is a public Hawking radiation code [57, 58]. There are two relations of interest in this accelerating mass-loss mechanism:

$$kT = 7.5\left(\frac{1.4\times10^9\ \mathrm{g}}{M}\right)\ \mathrm{TeV} \tag{3.4}$$

$$\tau = \left(\frac{M}{1.4\times10^9\ \mathrm{g}}\right)^3\ \mathrm{s} \tag{3.5}$$

In other words, a non-spinning, chargeless PBH of mass 1.4×10^9 g evaporates in one second and has a temperature of 7.5 TeV, while another PBH with 10 times the mass would evaporate in 1000 seconds and have a temperature of 750 GeV. While the Hawking radiation spectrum is not a delta function, the temperature of the BH does dictate the order

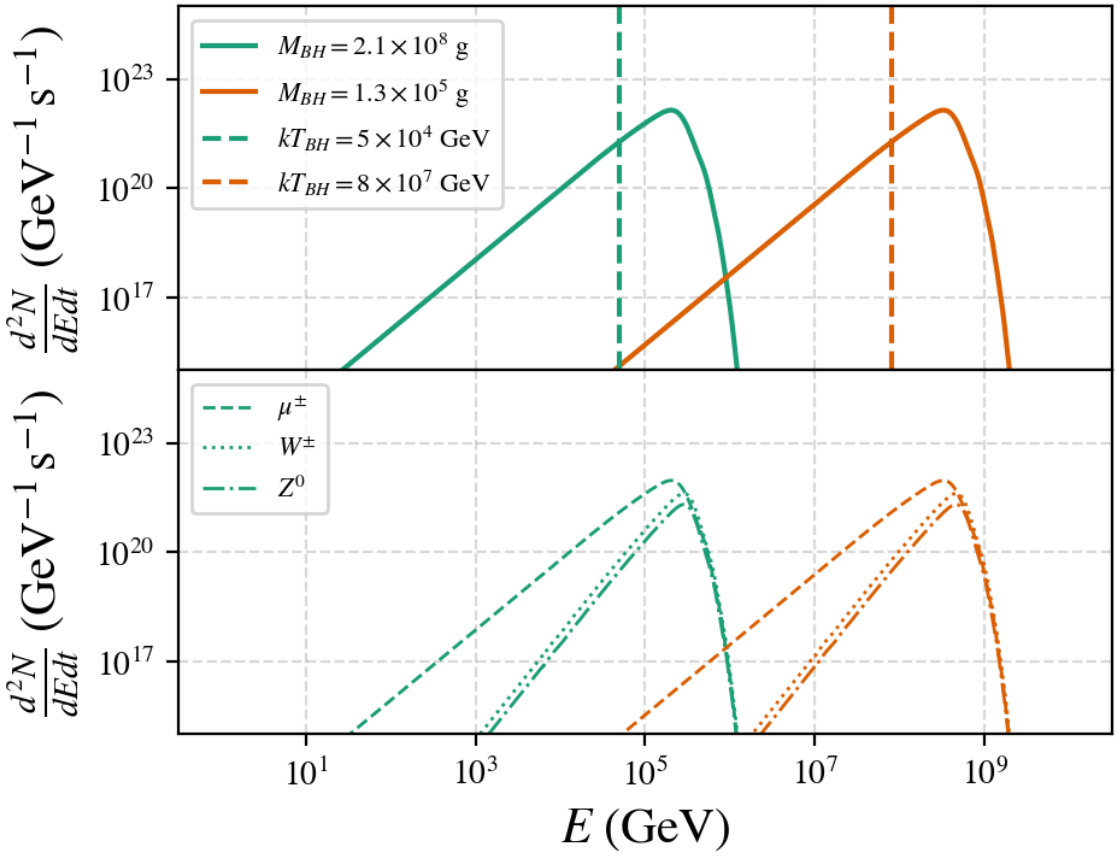

Figure 3.1: Instantaneous rate of Hawking radiation from two BHs with masses 1.3×10^5 and 2.1×10^8 g demonstrated for select elementary particle species: neutrinos (top), muons and $W^{\pm}$, Z^0 bosons (bottom). This type of emission is referred to in the text as *direct* particle production as opposed to by-products of decay and hadronization from unstable species. This calculation is performed by `BlackHawk` which is a public Hawking radiation code [57] [58]. I created this plot using the `matplotlib` package in `PYTHON`.

of magnitude of the peak in emission flux and is therefore an important factor in searching for PBHs. This form of emission described by Eq. 3.3 and shown in Fig. 3.1 defines *direct* neutrino production from a PBH. Additional neutrinos are produced by hadronization and decays, which define the *indirect* neutrino production from a PBH.

3.2.1 Indirect Neutrino Production

Direct quarks and gluons from Hawking radiation can hadronize, which can further decay into neutrinos. For instance, a charged pion can decay into 3 neutrinos as we saw in §2.2.1. I use the public dark matter decay code, `HDMSpectra` [59] to compute the final indirect neutrino emission rate after calculating the direct emission rate from `BlackHawk`. A popular particle physics code, `PYTHIA` lacks full electroweak corrections above 500 GeV primary (direct) so I compared HDMSpectra with PYTHIA to find consistent results below this energy range.

The decays are calculated using the fragmentation function method (`HDMSpectra.FF`), given the initial and final particle species and the initial energy. Another important parameter in calculating decay spectra with `HDMSpectra` is the range of allowable final particle energies. This is addressed by conveniently labeling the ratio of final to initial energy as x. The minimum possible value for x is a parameter aptly named $x_{\rm min}$ in `HDMSpectra.FF` and the allowable minimum is 10^{-6}, that is `HDMSpectra` calculates the decay/annihilation spectrum, dN/dx, upto a maximum of 6 orders of magnitude in energy below the primary (initial) energy. However, we do not have experimental data to confidently calculate dN/dx to such low secondary energies, so a lower $x_{\rm min}$ is more inaccurate [59].

The convolution of the decay spectra with the primary (initial particle) instantaneous Hawking radiation gives us the indirect instantaneous Hawking radiation rate:

$$\frac{d^2N_{f,i}}{dE_f dt}\left(E_f, M_{\rm BH}\right) = \int_{\min(E_i)}^{\max(\rm E_i)} \frac{d^2N_i}{dE_i dt}\left(E_i, M_{\rm BH}\right) \frac{dN^{i\to f}}{dE_i}\, dE_i \tag{3.6}$$

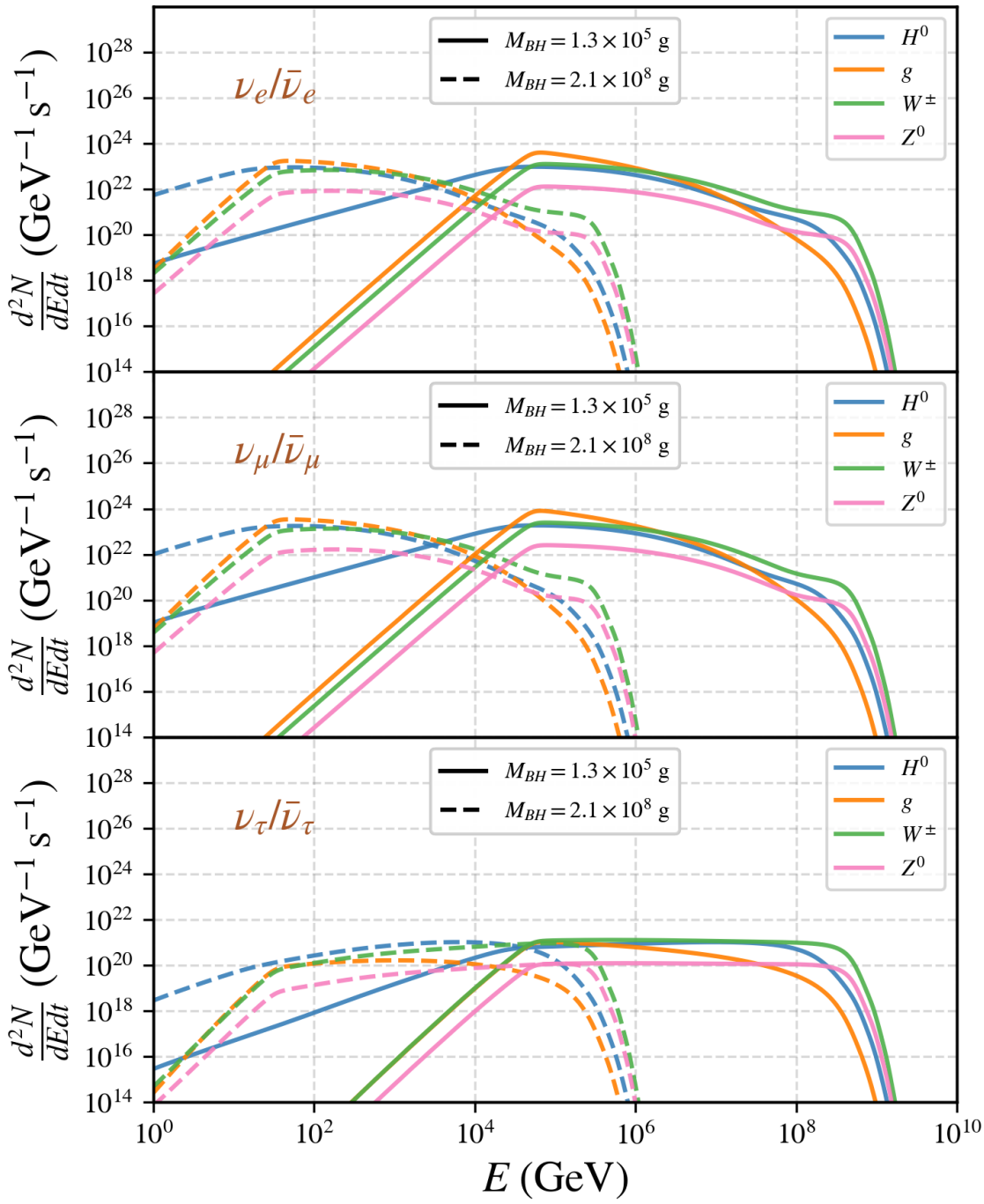

Figure 3.2: Per flavor, neutrino and anti-neutrino indirect Hawking spectrum rate from two PBHs, including contributions from H^0, g, $W^\pm$, and Z^0 that are indicated by the four colors in the legend. The solid and dashed lines correspond to different PBHs with masses 1.3×10^5 g and 2.1×10^8 g respectively while each panel corresponds to a final neutrino flavor as labeled. I calculated this using `BlackHawk` and `HDMSpectra` [57] [58] [59]. I created this plot using the `matplotlib` package in `PYTHON`.

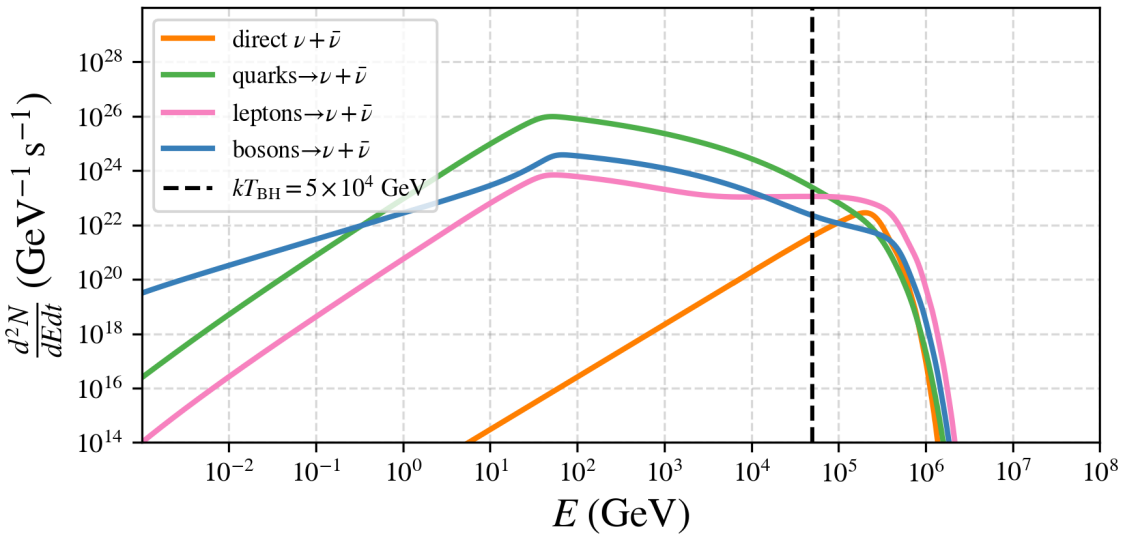

Figure 3.3: Total all-flavor instantaneous neutrino + anti-neutrino-rate spectrum rate of Hawking radiation from a BH with mass 2.1×10^8 g and temperature 5×10^4 GeV. This includes indirect $\nu+\bar{\nu}$ from all elementary particle species, including quarks (green), charged leptons (pink), and bosons (blue). While the direct component is competitive at energies greater than the temperature of the BH, the indirect component largely affects emission below the BH temperature. I calculated this using `BlackHawk` and `HDMSpectra` [57] [58] [59]. I created this plot using the `matplotlib` package in `PYTHON`.

Since we are only interested in neutrinos from Hawking radiation, we have six possible final particle species: $f \in \{\nu_e, \bar{\nu_e}, \nu_\mu, \bar{\nu_\mu}, \nu_\tau, \bar{\nu_\tau}\}$, while the initial particle species can be other elementary particles which can produce neutrinos namely quarks, q, charged leptons, ℓ, or bosons b (along with their anti-particles): $i \in \{q, \ell, b\}$. Additionally, $\min(E_i)$, $\max(E_i)$ are ideally 0 and ∞ respectively, but you typically have some limitations computationally. In this particular case, the upper bound is given by $x_{\min}$ since $x = E_f/E_i$. The lower bound is set by the minimum energy of an emitted particle for `BlackHawk` at 1 GeV. These individual contributions to the indirect, instantaneous neutrino rate can be compared across flavors, as shown in Fig. 3.2 for select primary/direct species like Higgs boson, gluons, and $Z^0/W^\pm$ bosons for two BH masses of 1.3×10^5 g and 2.1×10^8 g.

An interesting feature of Fig. 3.2 is that the indirect component from each primary/direct elementary particle rises below the black hole temperature. This is mainly due to the multiplicity of neutrinos from those specific primary species. However, due to limitations in our

knowledge of the decay rates, extremely low $x_{\min} < 10^{-6}$ are prohibited by `HDMSpectra`. To generate these plots, I use the recommended $x_{\min} = 10^{-4}$, which means the spectra would fall off approximately 4 orders of magnitude below the temperature of the black hole.

Finally, we can sum up the individual contributions to the total indirect neutrino + anti-neutrino spectrum rate:

$$\left.\frac{d^2 N_{\nu+\bar{\nu}}}{dEdt}\right|_{\text{indirect}} = \sum_{f\in\{\nu,\bar{\nu}\}} \sum_{i\in\{q,l,b\}} \frac{d^2 N_{f,i}}{dE_f dt} \tag{3.7}$$

The different components are demonstrated for a 10^8 g BH in Fig. 3.3.

3.3 Time-Integrated Emission

In this section, we consider integrating the direct and indirect neutrino emission from a nearby evaporating PBH in time-bins, as well as oscillating all neutrino flavors to ν_μ. Consider a non-spinning, evaporating PBH as its mass decreases and the temperature rises. Each "snapshot" in this process can be considered independently, that is a PBH with temperature, say 10^5 GeV will emit neutrinos directly and indirectly regardless of what its temperature was a day ago. In order to calculate the time-integrated emission, the total neutrino emission is calculated for each of these snapshots. In order to sample this evaporation properly, the snapshots are sampled in log-space of time to evaporation as per Eq. 3.5. We create 1000 snapshots of an evaporating PBH in log space of time to evaporation from a maximum of 10^8 seconds to a minimum of 10^{-12} seconds. Each snapshot contains per-flavor ($\nu_\alpha = \nu_e,\ \nu_\mu,\ \nu_\tau$) spectrum rate of neutrinos and anti-neutrinos, and can be labeled as $d^2N^{\nu_\alpha,i}/dEdt$ for the i-th snapshot. The time-integrated, per-flavor, neutrino spectrum would then be:

$$\frac{dN^{\nu_\alpha}}{dE} = \int_{\tau_i}^{\tau_f} \frac{d^2N^{\nu_\alpha,\,i}}{dEdt}\, dt \tag{3.8}$$

Each pair of τ_i and τ_f forms the aforementioned time-bins and is coarsely binned in comparison to the snapshots themselves to ensure that multiple snapshots are integrated in a single time-bins. For a point-source PBH search, we use 29 time-bins log-spaced from 10^{-8} to 10^{6} seconds, with the longest bin of up to 11.57 days. This is because typically we expect to be sensitive to a PBH burst up to ~ 0.001 pc or $\sim 3 \times 10^{13}$ km. Assuming a typical proper velocity at that distance to be v_d =300 km/s, one can deduce that the angular displacement of a PBH at that distance over a timescale of Δt =15 days is 0.7° ($\theta = v_d \Delta t/d$). This angular displacement becomes larger than the typical angular resolution of a muon-neutrino in IceCube for longer timescales ($>$ 2 weeks) and therefore breaks the point-source assumption.

For each pair of time-bin, (τ_i, τ_f), we can oscillate the per-flavor neutrino spectrum to ν_μ at Earth. This is done by using the most recent fits for PMNS matrix parameters (Nufit 5.1) for normal-ordering (NO) with Super-Kamiokande atmospheric data [60]. This oscillation is carried out by performing the following matrix multiplication:

$$\left.\frac{dN^{\nu_\alpha}}{dE}\right|_{\text{Earth}} = \frac{1}{4\pi d_{\text{ref}}^2} \sum_{\beta=e}^{\tau} \sum_{i=1}^{3} |U_{\alpha,i}|^2 |U_{\beta,i}|^2 \left.\frac{dN^{\nu_\beta}}{dE}\right|_{\text{PBH}}, \tag{3.9}$$

where $\alpha, \beta \in \{e, \mu, \tau\}$ and $U_{\alpha,i}$ are elements of the PMNS matrix while d_{ref} is the distance between Earth and the PBH. This is performed for muon neutrinos and anti-neutrinos in Fig. 3.4 by taking an reference distance from Earth to PBH of $d_{\text{ref}} = 0.01$ pc as per Eq. 3.9. The interesting feature for this spectrum is the change in shape around 10^3 GeV. Before this change, the sprectrum is fairly hard ($\propto E^{-0.8}$), while it is softer ($\propto E^{-3}$) after the change. The spectral "break" has been explored in the case of $\gamma-$rays as well and

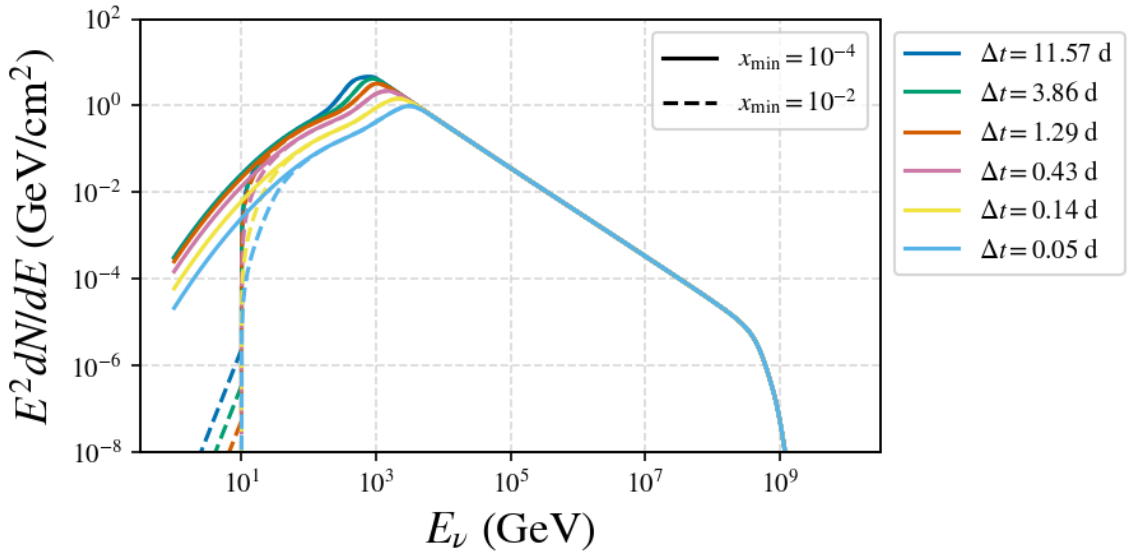

Figure 3.4: Total time-integrated muon neutrino and anti-neutrino spectrum at Earth from an evaporating PBH 0.01 pc away, using NuFit 5.1 normal-ordering best-fit parameters as per [60]. Each color represents a time-window corresponding to the time to evaporation i.e. longer time windows are inclusive of shorter time windows. The effect of `HDMSpectra` parameter $x_{\min}$ is demonstrated for values of 10^{-4}(solid) and 10^{-2}(dashed). The underlying direct and indirect spectrum rates across the evaporation stages are calculated using `BlackHawk` and `HDMSpectra` respectively [57] [58] [59]. I created this plot using the `matplotlib` package in `PYTHON`.

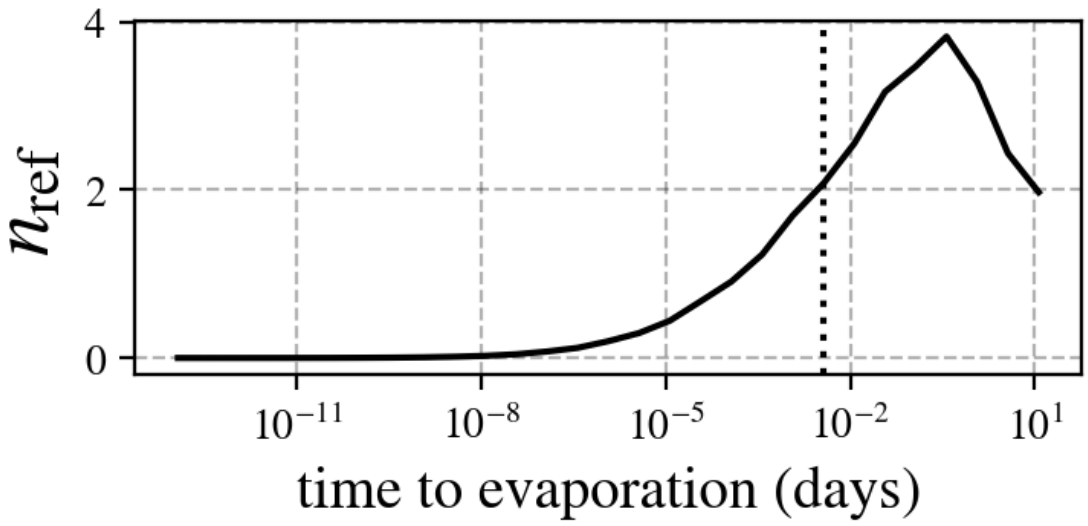

Figure 3.5: The total number of muon neutrinos expected in IceCube, n_{ref}, from a PBH evaporation event occurring 0.01 pc away at $\delta = 32°$. This is calculated by integrating the muon neutrino flux from PBH at Earth with the effective area of IceCube. The vertical dashed line indicates the 90% containment and the corresponding time to evaporation is 316 seconds. The chosen declination is for demonstrative purposes and this containment is robust up to an order of magnitude at other northern celestial sky declinations. I created this plot using the `matplotlib` package in `PYTHON`.

typically this shape is parameterized for use in searches for PBH bursts [19, 49, 50, 52]. This flux can be integrated with the effective area of a neutrino detector, such as IceCube, to calculate n_{ref} as a function of time to evaporation. For instance, 90% of events in IceCube can be expected to be observed after 316 seconds for a PBH evaporating 0.01 pc away at declination $\delta = 32°$. This time, translated to the temperature by Eq. 3.5, yields a PBH temperature of 1.1 TeV. For a 10 TeV indirect neutrino from a muon, via muon decay ($\mu^- \to \nu_\mu + \bar{\nu}_e + e^-$), the direct muon would have a Lorentz factor of $\gamma = 3 \times 10^5$, that translates to a muon decay time in the lab frame of 0.6 seconds. Essentially, for the purposes of detecting neutrinos in IceCube from PBH evaporation upto 0.05 days, these muons can be assumed to instantaneously decay. All other standard model particles considered here decay faster than the muon so this assumption is valid for $W^\pm$, Z^0, H^0, $\pi^\pm$, etc.

CHAPTER 4
NEUTRINO PHYSICS AND DETECTION

Neutrinos are weakly-interacting fermions, named to suggest they are small, electrically neutral particles. In fact, they are the lightest of all the non-zero rest mass elementary particles, travel very close to the speed of light, and are the most peculiar particles in the Standard Model. The traditional picture is that they have three flavors, corresponding to each charged lepton (electron, muon, tau lepton) and have an anti-particle for each flavor totaling to six types of neutrinos ($\nu_e,\ \bar{\nu}_e,\ \nu_\mu,\ \bar{\nu}_\mu,\ \nu_\tau,\ \bar{\nu}_\tau$). This chapter will summarize the discovery of neutrinos as a new particle in §4.1, while neutrino oscillations are briefly explained in §4.2. Neutrino interactions with matter are covered in §4.3 which involve the basis of current large-scale neutrino detectors, and finally these detection methods are explored for various current and future large-scale neutrino detectors in §4.5.

4.1 Discovery

In the early 1930's there was quite a bit of interest in the process of beta decay, particularly to explain the observed continuous beta energy spectrum. If an electron is the only product of beta decay as the atomic number (Z) of the atomic nucleus is increased by one, the beta energy spectrum should have a well-defined value. Additionally, the atomic mass number (A) is unchanged during beta decay, that is the nuclear spin remains unchanged. However, the exiting beta particle (electron) carries one-half spin so angular momentum is not conserved. Wolfgang Pauli proposed a resolution to this conundrum by suggesting a light, neutral particle named "neutron" resided in the nucleus and accompanied the electron during a beta decay [61]. Pauli's "neutron" was subsequently renamed "neutrino" by Enrico Fermi but was only confirmed experimentally $\sim$ 25 years later since it became clear that the small cross-section of neutrino interaction with matter meant this detection would be

notoriously difficult.

In 1956, Clyde Cowan and Frederick Reines experimentally confirmed the existence of neutrinos [62]. The basis for this experiment was observing the inverse beta decay: $\bar{\nu}_e + p \rightarrow n + \bar{e}$, wherein the exiting anti-electron annihilates with a nearby electron to produce two observable photons, while the neutron is detected by getting captured by a nuclei and observing the resultant photon. A large flux of anti-electron neutrino would be needed to overcome the small interaction cross-section, estimated at the time to be $\sim 10^{-42}$ cm^{-2}, which a nearby nuclear reactor would be able to provide. After moving the experiment to the Savannah River Plant in South Carolina in 1955, they were able to confirm this decay channel and provide the first experimental evidence of neutrinos.

4.2 Oscillations

In 1961, Danby et. al. performed an experiment by striking aluminum targets with energetic neutrinos to show that the neutrinos accompanying muons in pion decay, $\pi \rightarrow \mu + \nu$, were different that the ones from beta decay [63]. This second discovery of neutrino is now called muon neutrinos ν_μ, whereas the ones from beta decay were (anti)-electron neutrinos $\bar{\nu}_e$. This led to the notion of describing neutrinos by their leptonic counterpart as "flavors". In the late 1960s, the solar neutrino flux was measured by R. Davis et. al. due to nuclear reactions in the Sun [64]. A number of experiments followed suit with different energy thresholds and concluded that the solar neutrino flux was significantly less than the predicted amount [65]. This is known as the solar neutrino problem and was resolved by understanding neutrino flavor oscillations.

Neutrino oscillation is a quantum mechanical phenomenon, by which a neutrino can spontaneously change it's flavor. Each observable flavor of neutrinos can then be considered a superposition of its (mass) eigenstates of the propagation operator, and vice-versa. For the simplistic 2-flavor case, say we have two flavor eigenstates ($\nu_e,\ \nu_\mu$) and two mass eigenstates ($\nu_1,\ \nu_2$), we can assume a mixing angle (θ_{12}) to demonstrate the transformation

between the eigenstates:

$$\begin{pmatrix} \nu_e \\ \nu_\mu \end{pmatrix} = \begin{pmatrix} \cos\theta_{12} & -\sin\theta_{12} \\ \sin\theta_{12} & \cos\theta_{12} \end{pmatrix} \begin{pmatrix} \nu_1 \\ \nu_2 \end{pmatrix} \tag{4.1}$$

The oscillation probability ($\nu_\mu \rightarrow \nu_e$) for this 2-flavor case would then be:

$$P_{\nu_\mu \rightarrow \nu_e} = \sin^2 2\theta_{12} \ \sin^2 \left[1.27 \ \frac{(m_2^2 - m_1^2)\, L}{4E_\nu} \ \frac{[\mathrm{GeV}]}{[\mathrm{eV}^2]\ [\mathrm{km}]} \right] \tag{4.2}$$

For this 2-flavor case, we additionally have the probability of a neutrino to retain its flavor, $P_{\nu_\mu \rightarrow \nu_\mu} = 1 - P_{\nu_\mu \rightarrow \nu_e}$. It is important to note that in Eq. 4.2, the mixing angle ($\sin^2 2\theta_{12}$) determines the amplitude of the oscillation, while Δm^2 influences the oscillation length given a fixed distance traveled per energy, L/E_ν. Additionally, in 1989 the observation of the energy distribution of Z^0 resonance in the Large Electron-Positron Collider (LEP) and Stanford Linear Accelerator Center (SLAC) experiments determined that there were 3 standard neutrino flavors [66]. This established that there were 3 generations of fermion families.

We will now consider the standard picture of neutrino oscillations with 3 flavors, wherein we have $\nu_e \Leftrightarrow \nu_\mu,\ \nu_e \Leftrightarrow \nu_\tau,\ \nu_\mu \Leftrightarrow \nu_\tau$. In 1997, the Super-Kamiokande (Super-K) group reported the first clear evidence of this oscillation. Note that, just like the 2-flavor case, a non-zero, finite Δm^2 is required for neutrinos to oscillate and this study by Super-K indicated that neutrinos need to have non-zero mass [67]. The 3-flavor oscillation is described by the 3x3 lepton mixing matrix, or the Pontecorvo–Maki–Nakagawa–Sakata (PMNS) matrix [60]:

$$U_\nu = \begin{pmatrix} 1 & 0 & 0 \\ 0 & c_{23} & s_{23} \\ 0 & -s_{23} & c_{23} \end{pmatrix} \begin{pmatrix} c_{13} & 0 & s_{13}e^{-i\delta} \\ 0 & 1 & 0 \\ -s_{13}e^{i\delta} & 0 & c_{13} \end{pmatrix} \begin{pmatrix} c_{12} & s_{12} & 0 \\ -s_{12} & c_{12} & 0 \\ 0 & 0 & 1 \end{pmatrix}, \tag{4.3}$$

where $s_{ij} = \sin\theta_{ij}$, $c_{ij} = \cos\theta_{ij}$, and δ is the CP violating parameter. This matrix is then used in a way similar to the 2-flavor case:

$$|\nu_\alpha\rangle = \sum_{i=1}^{3} U^*_{\alpha i} |\nu_i\rangle , \tag{4.4}$$

where α, i are the row and column elements of U^*_ν respectively. Additionally, the oscillation probability is similar:

$$P_{\alpha\to\beta} = |\langle\nu_\beta(L)|\nu_\alpha\rangle|^2 \left| \sum_{i=1}^{3} U^*_{\alpha i} U_{\beta i} e^{-i\frac{m_i^2 L}{2E_\nu}} \right|^2 \tag{4.5}$$

While the neutrino cross-section is extremely small, a weak potential in dense medium (Earth, Sun) can affect neutrino oscillations by coherent forward scattering of ultra-relativistic electron neutrinos. This matter effect, known as the Mikheyev–Smirnov–Wolfenstein (MSW) effect, produces effective mass and it may seem those massless neutrinos could gain mass in the matter but it can be shown that massless neutrinos cannot even oscillate in matter [68]. That is, ν_e, $\bar{\nu}_e$ can interact with e^- via W exchange while no other neutrino can. This creates an effective potential of ν_e with respect to other neutrino flavors when propagating through matter.

Currently, all three mixing angles θ_{ij}, two Δm^2, and the CP violation phase, δ are known from global-fit results such as `NuFIT` [60]. While δ can have non-zero best-fit values, CP violations have not yet been observed in neutrino oscillations. Additionally, there are two non-equivalent orderings possible:

- $m_1 << m_2 < m_3$ which is referred to as Normal Ordering (NO)

- $m_3 << m_1 < m_2$ which is referred to as Inverted Ordering (IO),

with the latest studies favoring NO slightly. The latest constraint to the electron neutrino mass is < 0.8 eV/c^2 as per the KATRIN experiment [69] by measuring beta decay from tritium, so this is an active area of research as well. In addition to these three standard neutrino flavors, the possibility for a fourth flavor of neutrino, called a sterile neutrino, exists. A sterile neutrino is a type of neutral lepton that does not undergo ordinary weak interactions, except for those that are induced by mixing which is referred to as 3+1 neutrino mixing in literature. This type of neutrino is present in most extensions of the standard model, and in principle can have any mass. This possibility is currently being investigated [70, 71] and there is no evidence yet to support its existence.

4.3 Neutrino-Matter Interactions

Neutrinos only interact via weak interaction and gravity with matter. In order to understand the detection of neutrinos, we need to first look at how neutrinos interact with nucleons via the weak interaction. Additional emphasis will be made on how these interactions can be detected in a medium such as water or ice and how they can aid neutrino astrophysics. In this section, I will give an overview of the main channels of neutrino interaction with a nucleon. This classification is made by the charge of the mediating boson ($W^{\pm}$ or Z^0) in the interaction. At incoming neutrino energies of $\gtrsim 20$ GeV, the neutrino interacts with a quark instead of the whole nucleon, breaks apart the nucleon, and causes a hadronic shower. This type of interaction is called Deep Inelastic Scattering (DIS) and also follows the previously mentioned classification depending on the charge of the mediating boson. Additionally, I will discuss the $\bar{\nu}_e e^-$ resonance at 6.3 PeV, also known as Glashow resonance [72].

4.3.1 Neutral Current (NC)

As shown in Fig. 4.1a, when a neutrino of flavor $l \in \{e,\ \mu,\ \tau\}$ interacts with a nucleon via a mediating Z^0 boson, it produces a hadronic shower along with another neutrino (of the

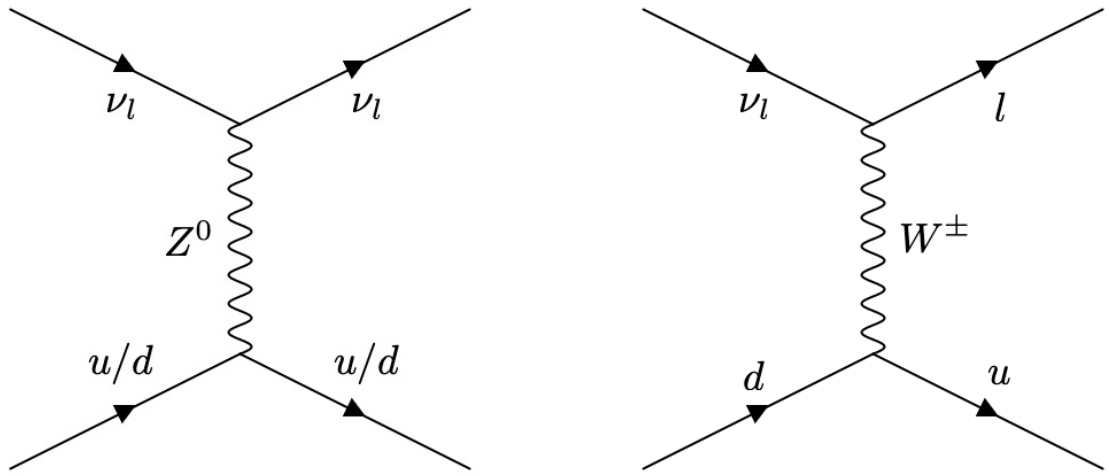

(a) Neutral Current (NC) interaction

(b) Charged Current (CC) interaction

Figure 4.1: Example Feynman diagrams of a neutrino interaction with a quark. This figure was made using an online tool for creating Feynman diagrams.

same flavor as the incoming neutrino) as follows:

$$\nu_l + N \rightarrow \nu_l + X \tag{4.6}$$

In this type of interaction, a fraction of the energy of the incoming neutrino is used in the interaction, and the outgoing neutrino escapes with the rest of the energy. For DIS NC interactions, the nucleon is broken apart, and a single hadronic shower follows. As we shall see in the next section, §4.4, this can be observed in water/ice via Cherenkov radiation.

4.3.2 Charged Current (CC)

As shown in Fig. 4.1b, when a neutrino of flavor $l \in \{e,\ \mu,\ \tau\}$ interacts with a nucleon via a mediating $W^\pm$ boson, it produces a hadronic shower and an outgoing charged lepton (of the same flavor as the incoming neutrino) as follows:

$$\nu_l + N \rightarrow l^\mp + X \tag{4.7}$$

The charged lepton produced in a CC interaction carries $\sim 80\%$ of the energy. In the case of an energetic $\nu_\mu/\bar{\nu}_\mu$ interacting with a nucleon, N, the outgoing $\mu^\pm$ can travel several kilometers inside a medium (water/ice) before decaying. As we shall see in the next section, §4.4, this muon emits Cherenkov radiation in water/ice which can be detected. More interestingly, at very high energies this muon is almost collinear with the incoming muon neutrino, and the angle between them can be parameterized by $\sim 0.7^\circ(E_\nu/\mathrm{TeV})^{0.6}$. This is particularly useful to provide good angular resolution for large-scale neutrino detectors. Additionally, for a DIS CC interaction producing a $\mu^\mp$, X is the hadronic shower so in order to "reconstruct" this type of interaction in water/ice, both the charged lepton and a hadronic shower need to be accounted for.

Similarly, when $\nu_e/\bar{\nu}_e$ interact with a nucleon via the CC channel, an electron/positron is produced. In a medium, this generates an electromagnetic shower and the outgoing electron/positron does not travel very far. In the case of a DIS CC interaction producing an $e^\mp$, a hadronic shower is also produced along with an electromagnetic shower, which can be difficult to differentiate from NC interactions in water/ice. Finally, a $\tau^\mp$ lepton can also be produced in a CC interaction which varies in decay length based on its energy (50 m for 1 PeV, 500 m for 10 PeV). In the case of a DIS CC interaction producing a $\tau^\mp$, the tau decay can produce a hadronic or leptonic shower, so two hadronic showers some distance apart in water/ice can be an identifying signature for tau neutrinos.

4.3.3 Glashow resonance

In 1960, Sheldon Glashow proposed a resonant formation of a $W^\pm$ boson when a 6.3 PeV (anti) electron-neutrino interacts with an electron [72]. In 2021, the IceCube neutrino detector reported a shower of high-energy particles with an astrophysical origin and energy of 6.05 ± 0.72 PeV. This provided the first evidence of this resonant effect [73]. Since the

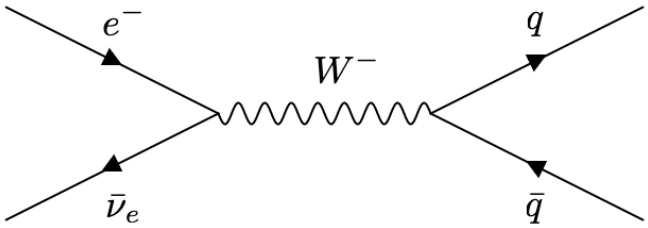

Figure 4.2: An example Feynman diagram for Glashow resonance, where the W^- produces secondary particles such as quarks. This figure was made using an online tool for creating Feynman diagrams.

$W^{\pm}$ has various branching decay modes, this interaction can be generally described as:

$$\bar{\nu}_e + e^- \rightarrow W^- \rightarrow X, \tag{4.8}$$

where X can be a pair of quarks as shown in Fig. 4.2. The standard model cross-section of this process is maximized for $E_{GR} = M_W^2/(2m_e)$, where $M_W = 80.38$ GeV is the rest mass of the W^- and $m_e = 0.511$ MeV is the rest mass of the electron. Identifying Glashow resonance interaction events can be extremely useful for neutrino astrophysics since they have to be produced by an $\bar{\nu}_e$, and therefore can be used as a discriminating tool between pp and $p\gamma$ interactions (see §2.2.1, §2.2.2). Since it is extremely difficult for water/ice-based neutrino detectors to separate neutrinos from anti-neutrinos, Glashow resonance interaction events can provide a $\bar{\nu}_e$ flux as well as verify the energy calibration of a detector.

4.4 Cherenkov Radiation

A charged particle traveling in a dielectric medium faster than the phase velocity of light in that medium emits radiation, which is called Cherenkov Radiation. This phenomenon was discovered by physicist Pavel Cherenkov in 1934. A popular analogy is a sonic boom for traveling faster than the speed of sound. This occurs because the charged particle asymmetrically polarizes the dielectric medium, causing a change in the electric field. The electric

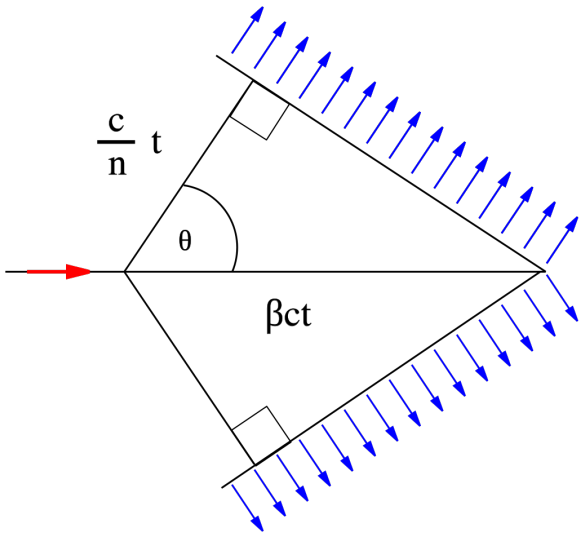

Figure 4.3: An illustration of Cherenkov radiation emitted by a charged particle moving in a dielectric medium with refractive index n at speed $v_p = \beta c$. Note that the radiation is conical and this illustration is a 2D slice. Figure from wikimedia commons, under the Creative Commons Attribution-Share Alike 2.5 Generic license.

field then drives the emission of light waves, which radiate away from the particle in a cone-shaped pattern.

Say, we have a charged particle moving through a dielectric medium at a speed $v_p > c/n$, where c is the speed of light in vacuum and n is the index of refraction in the dielectric medium. In this situation, the charged particle would emit Cherenkov radiation at an angle given by trigonometry:

$$\theta = \cos^{-1}\left(\frac{ct/n}{\beta ct}\right) = \cos^{-1}\left(\frac{1}{\beta n}\right), \tag{4.9}$$

where $\beta = v_p/c$ as illustrated in Fig. 4.3. We can consider the limiting case where the charged particle is moving at the speed of light in the medium to calculate the energy threshold. This special case is satisfied when $\beta_{tr} = 1/n$, and the threshold energy, E_{tr}, of

the charged particle is:

$$E_{tr} = \gamma mc^2 = mc^2 \sqrt{\frac{1}{1-\beta_{tr}^2}} \tag{4.10}$$

$$E_{tr} = mc^2 \frac{n}{\sqrt{n^2-1}} \tag{4.11}$$

In a medium such as water ($n = 1.33$) or ice ($n = 1.31$), the typical threshold energy is 1.52 or 1.55 times the rest mass of the particle. On the other end of the energy spectrum, there exists a maximum angle for an ultra-relativistic particle $\beta \sim 1$. For instance, in water, this maximum angle is $\approx 43°$. Additionally, the intensity of Cherenkov radiation, that is the number of photons per unit length of particle path and per unit of radiation wavelength, is given by the Frank-Tamm formula:

$$\frac{d^2N}{dx\, d\lambda} = \frac{4\pi^2 z^2 e^2}{hc\lambda^2}\left(1 - \frac{1}{n^2\beta^2}\right), \tag{4.12}$$

where the charge of the particle is $q = ze$. In a medium of ice and $\beta \to 1$, this intensity is ~ 200 photons/cm. Note that the intensity is inversely proportional to λ^2, which means Cherenkov radiation prefers shorter wavelengths. Typically, the emitted radiation has a range of ultraviolet to visible light wavelengths, with the exact range depending on the refractive index of the medium and the velocity of the particle. For example, in water, the Cherenkov radiation emitted by high energy electrons has a wavelength range of about 200-600 nm, which is in the ultraviolet to blue light range. In air, the wavelength range is slightly longer, from about 300-800 nm, encompassing ultraviolet to violet light.

This unique phenomenon allows the prospect to detect neutrinos since neutrino-matter interactions produce charged particles as we saw in §4.3. Typically, an array of light detectors (photomultipliers tubes or PMTs) is deployed in ice/water, optimized to detect Cherenkov radiation from neutrino-matter interactions. The arrival time and the number of Cherenkov photons from different PMTs allow for the reconstruction of the original neu-

trino direction and energy. However, neutrinos are not the only source of charged particles on Earth. We know that cosmic rays produce a shower of particles when they interact with the upper atmosphere (see §2.3). For instance, cosmic rays can produce energetic muons that travel to the surface (thanks to time dilation) before decaying. This atmospheric muon would also be detected by Cherenkov radiation and would constitute as "background" for a neutrino detector (array of PMTs) hoping to detect astrophysical or atmospheric neutrinos deployed near the surface. In order to suppress this background of atmospheric muons, most neutrino detectors are deployed deep underground. Additionally, understanding the optical properties of the medium (absorption, scattering) in which a neutrino detector is deployed is extremely useful, as this directly affects the arrival time of Cherenkov photons in the PMTs.

4.5 Current & Future Detection Methods

As we saw in the previous section, a neutrino detector can reduce atmospheric muon contamination by being deployed underground as well as detect neutrinos by detecting Cherenkov photons in a dielectric medium (ice/water) via PMTs. For this dielectric medium of ice/water, in the optical band, scattering and absorption of Cherenkov photons are mainly dominated by impurities. In this section, I shall briefly summarize the optical properties of ice to detect neutrinos (for IceCube) before moving on to the detection principles of current and future detectors.

The refractive index of ice is 1.31, which is slightly lower than that of water (1.33), which means that light travels slightly faster in ice than in water. Secondly, ice is largely transparent to visible light, with minimal absorption in the visible spectrum. However, it does absorb some ultraviolet (UV) and infrared (IR) light. Additionally, ice scatters light to a certain extent and the amount of scattering depends on the size, shape, and arrangement of the ice crystals. Ice also has a property known as birefringence, which splits light into two separate polarized rays that travel at different speeds through the material. This can

cause light to be partially or completely reflected, leading to the phenomenon of ice halos. Finally, antarctic ice is generally optically clear, with minimal cloudiness or impurities. However, the clarity can be affected by the presence of air bubbles, which scatter light and cause the ice to appear cloudy. All of these properties combine to affect neutrino event reconstruction in IceCube, as we shall see in the next chapter.

4.5.1 Super-Kamiokande

Super-**K**amiokande (Super-K) is a large underground neutrino detector located in Japan. It is designed to detect neutrinos through Cherenkov radiation emitted by charged particles produced when neutrinos interact with water. The detector consists of a cylindrical tank of purified water surrounded by photo-multiplier tubes (PMTs) which detect Cherenkov photons. Super-K has helped to make significant contributions to our understanding of neutrinos, including the discovery of neutrino oscillation (resolving the solar neutrino problem) and the measurement of the atmospheric neutrino oscillation parameters [67]. Super-K has also placed constraints on the possible existence of proton decay and searched for signals of dark matter. While Super-K's sensitivity diminishes at high-energy to perform neutrino astronomy, it will be able to detect a galactic supernova [74].

4.5.2 AMANDA

The **A**ntarctic **M**uon **a**nd **N**eutrino **D**etector **A**rray (AMANDA) project served as a precursor to IceCube Neutrino Observatory at the South Pole. Its goal was to attempt to search for astrophysical neutrinos, by spreading out the photomultiplier tubes (PMTs) in a larger detector volume deep in the ice (depth of 1.5 - 2 km below the surface) and thereby being able to detect higher energy neutrinos than Super-K. At 400 nm wavelength (for a typical Chereknov photon), they reported the absorption and scattering length in ice to be 110 m and 20 m respectively [75]. However, the optical ice properties vary with depth, due to horizontal "sheets" of ice that accumulated due to climate variations cause an increase in dust

concentration. Some of the reconstruction and analysis methods developed for AMANDA are used by IceCube today and it proved that the antarctic ice is a possible medium to detect neutrinos.

4.5.3 ANTARES

The ANTARES neutrino telescope finished deploying in the Mediterranean Sea in 2008 and is the first operational undersea neutrino telescope [76]. It consists of 900 PMTs, deployed in 12 lines to form a grid. Each line contains 25 storeys, which in turn contains 3 PMTs. The detector volume covers 10 Megaton of water, which is 0.01 km^3. Due to its geographic location, it provided the best sensitivity to neutrino sources (below hundreds of TeV) in the southern hemisphere. After 16 years of operation, it was decommissioned in February of 2022 as the focus shifted towards a larger network of neutrino detectors in the Mediterranean Sea.

4.5.4 KM3NeT

KM3Net is a planned cubic-kilometer neutrino telescope in the Mediterranean Sea. It has two components: ARCA near Sicily, Italy and ORCA near Toulon, France. ARCA, or **A**stroparticle **R**esearch with **C**osmics in the **A**byss, targets high-energy neutrino astrophysics with sensitivity in the range of GeV to PeV. Currently, in its first phase of deployment, ARCA is a 0.1 km^3 detector that is already taking data with the next phase planned to reach 1 km^3 detectable volume. Thanks to its geographic location in the northern hemisphere and sensitivity, it will be able to see the galactic plane in neutrinos and neutrino point sources in our galaxy in the future. If the γ-ray emissions from galactic point sources are purely of hadronic origin, KM3NeT will be able to detect them within a few years of observation. These sources include Vela X (a nearby Pulsar Wind Nebula), Vela Jr and RX J1713.7-3946 (young shell-type Supernova Remnants) and the galactic center [77]. ORCA, or **O**scillation **R**esearch with **C**osmics in the **A**byss, will focus on oscillation studies of at-

mospheric neutrinos in the GeV range.

4.5.5 Baikal-GVD

Baikal-GVD is an under-construction **G**igaton **V**olume **D**etector in Lake Baikal, Russia that will be another cubic-kilometer deep underwater Cherenkov detector. It has begun taking data and reached $0.4\ \mathrm{km}^3$ detector volume [78]. Its aim is to search for high-energy incoming neutrinos between several TeV and tens of PeV. At Cherenkov photon wavelengths of 480-500 nm, the effective absorption length is ~ 22 m and the effective scattering length is ~ 70 m. In late 2022, they reported an observation of the diffuse cosmic neutrino flux [79].

4.5.6 P-ONE

The **P**acific **O**cean **N**eutrino **E**xplorer is a proposed segmented and scalable neutrino detector to be installed at Cascadia Basin at a depth of 2660 meters as a part of Ocean Networks Canada (ONC). ONC forms one of the world's largest and most advanced cabled ocean observatory [80], thereby making it a promising site for a cubic-kilometer scale neutrino telescope. The site is currently being investigated for its optical properties by deploying pathfinder missions.

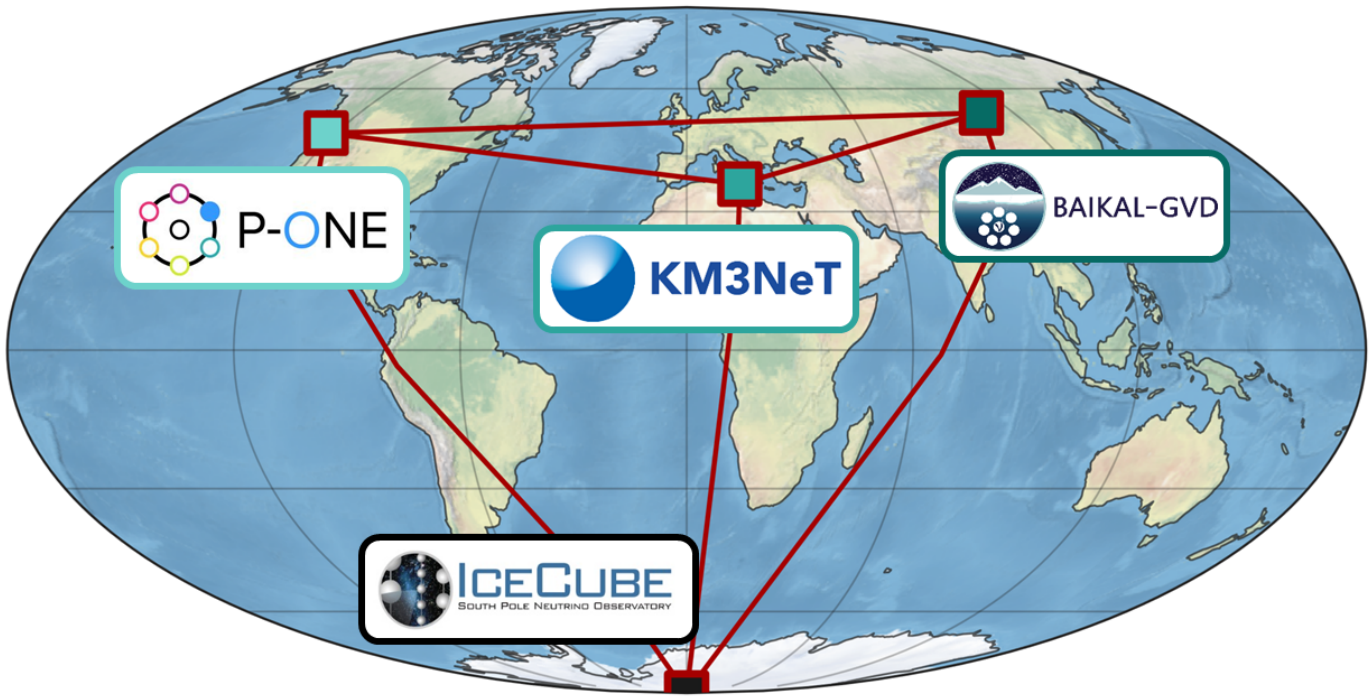

Figure 4.4: Map of current and future neutrino telescopes. Figure taken from ICRC 2021 proceeding by the P-ONE [80]

CHAPTER 5

ICECUBE

Situated at the geographic South Pole, IceCube is a cubic kilometer of antarctic ice that serves as a high-energy neutrino detector via the deployment of numerous PMTs (photo-multiplier tubes) in an array. The detection principle of neutrinos in the ice is via Cherenkov radiation of relativistic, charged by-products of neutrino interaction with matter. Full deployment of the detector finished in 2010/2011. IceCube consists of three sub-detectors, namely the In-Ice Array (§5.1.1), DeepCore (§5.1.2), and IceTop (§5.1.3). In this chapter, I will provide an overview of the detector and how different high-level data samples used for point-source analyses are processed.

5.1 Detector Configuration

The basic detection unit of the IceCube detector is a digital optical module (DOM). It contains a 10" PMT and other circuitry that helps digitize the PMT signal [81]. These DOMs are deployed in the antarctic ice, at a depth of 1.45-2.45 km below the surface, via 86 vertical strings in a hexagonal array. The IceCube detector also includes a denser core (DeepCore) optimized for lower neutrino energies as well as a surface array (IceTop) used to veto downgoing particles as shown in Fig. 5.1.

5.1.1 In-Ice Array

The primary in-ice array consists of 78 strings, each containing 60 DOMs, with a vertical separation of 17 m and a horizontal separation is 125 m. This design was chosen to optimize the detector for TeV-PeV neutrinos since that is the energy range where the atmospheric background contamination falls off in comparison to the astrophysical (signal). Additionally, the motivation for the horizontal string spacing is the absorption length of

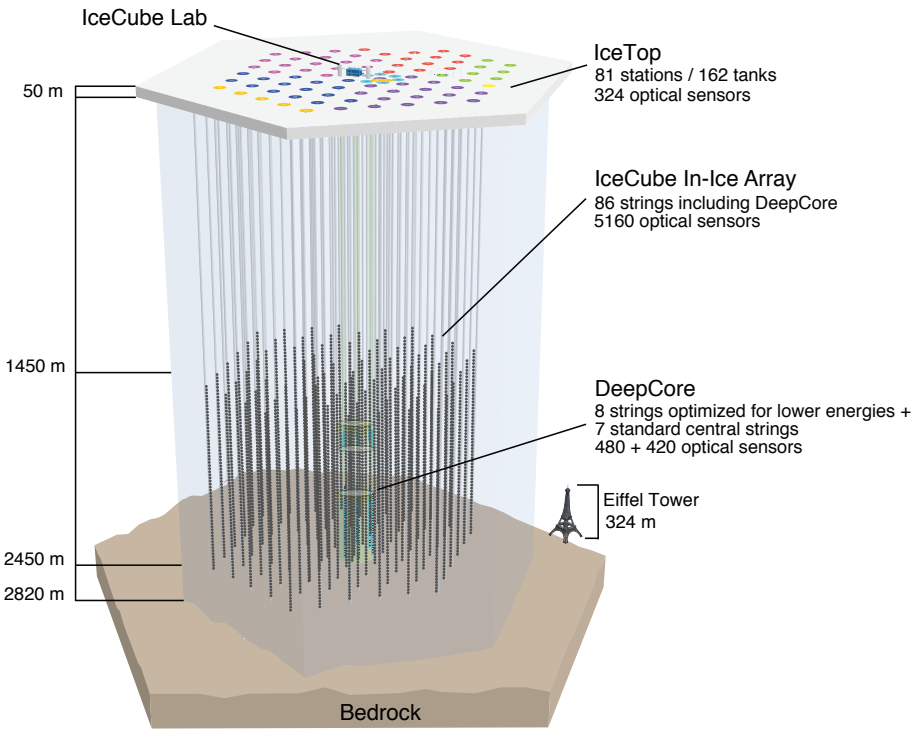

Figure 5.1: A schematic layout of the IceCube Neutrino Observatory at the South Pole. This figure, provided by the IceCube collaboration, was taken from [81].

Season	Code Name	IceCube strings	DeepCore strings	IceTop stations	Total DOMs
2004/05	IC1	1	0	4	76
2005/06	IC9	8	0	12	528
2006/07	IC22	13	0	10	820
2007/08	IC40	18	0	14	1136
2008/09	IC59	18	1	18	1212
2009/10	IC79	15	5	15	1260
2010/11	IC86-2011	5	2	8	452
Total		78	8	81	5484

Table 5.1: Deployment schedule of the IceCube detector along with seasonal code names indicating the detector configurations. All seasons after the full 86-string deployment in 2011 have IC86-20XX as their code names.

typical (400 nm) Cherenkov photons in the antarctic ice. This entire array is at a depth of 1.45-2.45 km below the surface of the ice and contains a cubic kilometer of ice volume. The layers of ice above this array act as a shield against the atmospheric $\mu^{\pm}$ which constitutes as background for astrophysical neutrinos as explained at the end of 4.4.

5.1.2 DeepCore

DeepCore is a denser core of 8 additional strings plus nearby in-ice strings, optimized for lower neutrino energies in the GeV-TeV range. It can be thought of as a compact Cherenkov detector. While the DeepCore PMTs have a higher quantum efficiency (HQE) of 40% more than the standard IceCube DOMs, the noise levels it receives are also higher. The DeepCore strings have a horizontal spacing of 72 m. Two sets of DOMs are deployed in these strings, above and below the dust layer from 2 - 2.1 km. The top set of 10 DOMs serves as a veto cap with 10 m vertical spacing while the bottom set of 50 HQE DOMs has reduced vertical spacing of 7 m below the dust layer. The rest of the IceCube detector also serves as a veto for downgoing atmospheric $\mu^{\pm}$. The main physics goals of DeepCore are:

- studying atmospheric neutrino oscillation
- detecting low-energy astrophysical neutrino sources, such as choked GRBs
- searches for dark matter annihilation and physics beyond the standard model

5.1.3 IceTop

IceTop is an extensive air shower array on the surface of the IceCube site. In its final configuration, the array covers a 1 km^2 area, with 81 stations, 78 of them located on top of each IceCube string and the rest are distributed in the inner region of the IceCube array. Each station consists of a pair of cylindrical ice-filled tanks separated from each other by 10 m on average. The PMT of each DOM in the tanks faces downward and are installed on the top of the tank. Each tank is lined inside with reflective material. The effective

threshold for IceTop is about 500 TeV for a trigger requirement of five or more stations. The local coincidence between two tanks at a station is used to discriminate signal showers from random noise coming from uncorrelated photons, electrons, or muons. Its physics goals are:

- studying the primary cosmic-ray energy spectrum
- calibrating IceCube event reconstructions
- vetoing atmospheric $\mu^{\pm}$ background

5.2 Ice Properties

Before we investigate how IceCube collects data, we need a detour to understand the Antarctic ice as photon propagation is a key part of Cherenkov radiation. Just like astronomers like to call anything heavier than helium a metal, IceCube likes to call any impurity in the ice "dust" so I shall use a similar definition. Understanding the distribution of these impurities is important for a Cherenkov detector since this affects the primary optical properties of ice, namely absorption and scattering of photon propagation. The foremost issue is air bubbles in the ice, and in order to deal with them IceCube DOMs are deployed below a depth of 1.45 km. At this depth, the pressure compresses air bubbles into clathrates of similar index of refraction as the ice and a 1969 study found that this accounts for the disappearance of gas bubbles at depths greater than 1.2 km [82]. Additionally, we know that the depth-dependent ice layers correspond to the Earth's climate history of the past $\sim 120,000$ years, so one can imagine a composite of ice layers (which need not be flat) of similar dust concentrations.

The optical properties affected by dust are studied via dust-logger devices and in-situ calibration using LED flashers within the IceCube array, to get a better handle on the optical properties of ice, which are critical to describe Cherenkov photon propagation. This is conducted by *flasher runs* to calibrate the detector. Each DOM has 12 LEDs that emit light

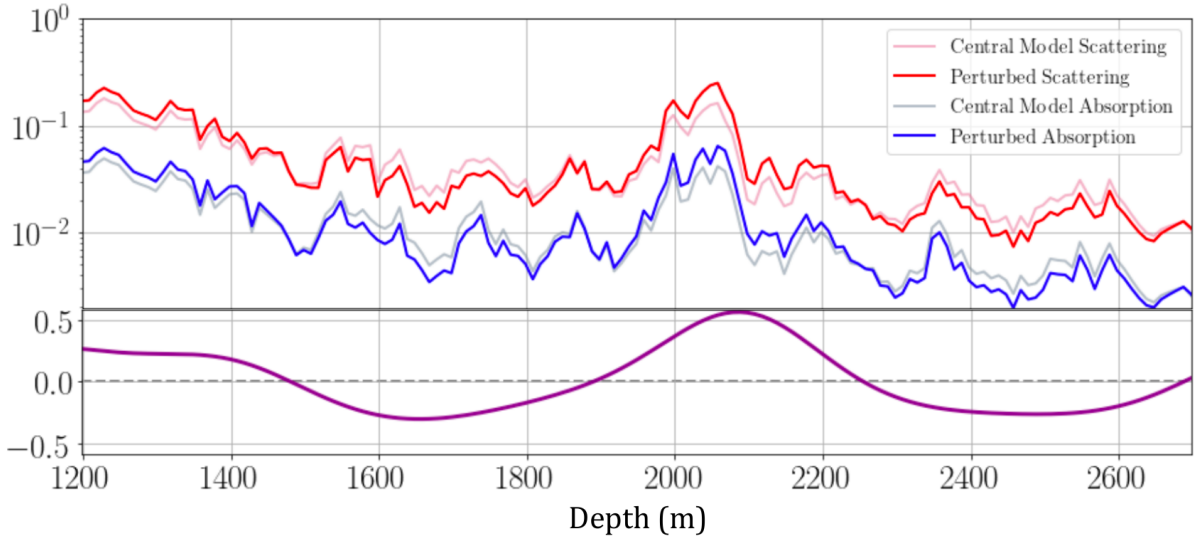

Figure 5.2: A relatively large perturbation in ice properties that illustrates depth-dependent features. The solid blue and red lines in the top panel provide the depth dependence of the absorption and scattering coefficients from an IceCube ice model. In contrast, the shaded lines represent an example of the aforementioned perturbations. The bottom panel is an example perturbed model used in a recent study. Note that the in-ice array extends at a depth of 1.45 - 2.45 km. This figure is taken from [83].

at frequencies expected by Cherenkov radiation. During these calibration runs the light yield across an array of DOMs is recorded when the LEDs from each DOM emit photons. The properties of the ice (such as absorption and scattering coefficients) are estimated in a simulation and can be fitted to the observed results as a function of DOM position. Gustav Mie, in 1908, formulated the scattering of plane waves by a sphere [84] and Mie scattering is accounted for by (south pole) ice models, such as SpiceMie [85]. The dust particles, modeled as a sphere, are similar or larger in size to the wavelength of light so effect of Mie scattering is important. A noticeable feature of the optical properties of South Pole ice presented in Fig. 5.2 is the peak at $\sim$ 2 km depth, which implies many impurities. These impurities are believed to originate from the previous to last glacial maximum, as cold periods expose more land and thereby increase impurities in the rain or snow [86]. Finally, not only are impurities depth-dependent but there also exists an azimuthal anisotropy [83].

Ice Model	**Year**	**Comments**	**Model error**
WHAM	2011		42%
SPICE 1	2009		42%
SPICE 2, 2+, 2x, 2y	2010	added ice layer tilt	29%
SPICE Mie	2011	fit to scattering function	29%
SPICE Lea	2012	fit to scattering anisotropy	20%
SPICE (Munich)	2013	7-string, LED unfolding	17%
SPICE3 (CUBE)	2014	LLH fixes, DOM sensitivity fits	11%
SPICE 3.0 (2015)	2015	improved RDE, ang. sens. fits	10%
SPICE 3.1, 3.2	2016	85-string, correlated model fit	$<$10%
SPICE HD, 3.2.2	2017	direct HI and DOM sens., cable, DOM tilt	–
SPICE EMRM	2018	absorption-based anisotropy single	–
SPICE BFR	2020	birefringence-based anisotropy LEDs	–

Table 5.2: A table summarizing the development of various South Pole ice models developed by the IceCube collaboration over the past decade. Older models that were developed going back to AMANDA (§4.5) days are not included. Model errors include precision in charge prediction. Tabulated data taken from [87].

Another noteworthy form of impurity in the ice comes from deploying the detector. As large holes were drilled in the ice to lower the strings with DOMs, the melt water was left to refreeze and secure the placement of the detector. The refrozen ice in the drill hole, of

diameter $\sim$ 60 cm, is referred to as *hole ice* (HI). In order to best understand the qualities of the hole ice, a camera system was installed on string 80 to monitor the refreezing of the ice. It was found that in the first few days, freezing occurred on the edge of the hole. It took 15 days for the hole to freeze completely. During this natural freezing process, it was found that the inner 16 cm layer contained air bubbles that were pushed to the center. Our understanding of the Antarctic ice has increased dramatically over the past couple of decades and ice models have been updated to include the important physical effects, such as birefringence [88], which are listed in Table 5.2. These ice models have been adjusted to include ice layer tilts, and include improvements to relative DOM efficiency (RDE), angular sensitivity fits, and direct hole ice (HI) sensitivity.

5.3 Event Classification

As a Cherenkov detector deep in the antarctic ice, IceCube observes a variety of events. These events are topologically different (based on the interaction being observed) and contain an abundance of cosmic-ray muon background. In this section, we shall consider two types of events, namely tracks and cascades, that relate to the charged current (CC) and neutral current (NC) neutrino interactions discussed in §4.3. This classification is made based on the track length of the particles. Since we want to work backward and infer the properties of the interaction based on this distribution, this is a particularly useful way to think about events in IceCube. Note that, charged particles observed from neutrino interactions in the ice or from cosmic-ray air showers, can produce identical imprints in the detector. Additionally, events might not be easily discernible between two topological types if they are low-energy, so in this section, I will only consider high-energy events that can be visually distinguished.

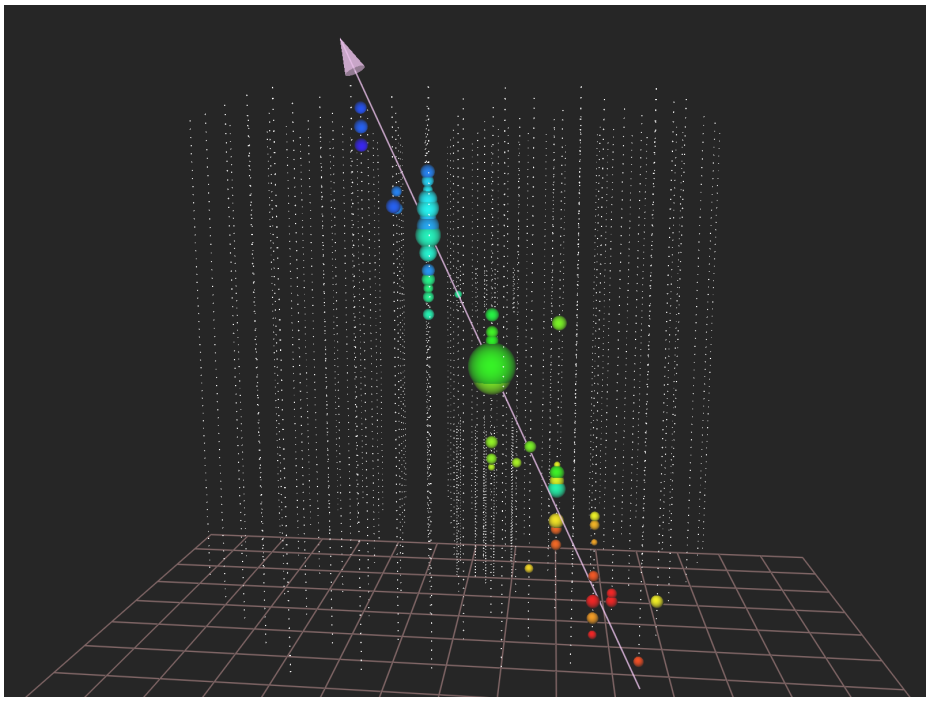

(a) Example track event

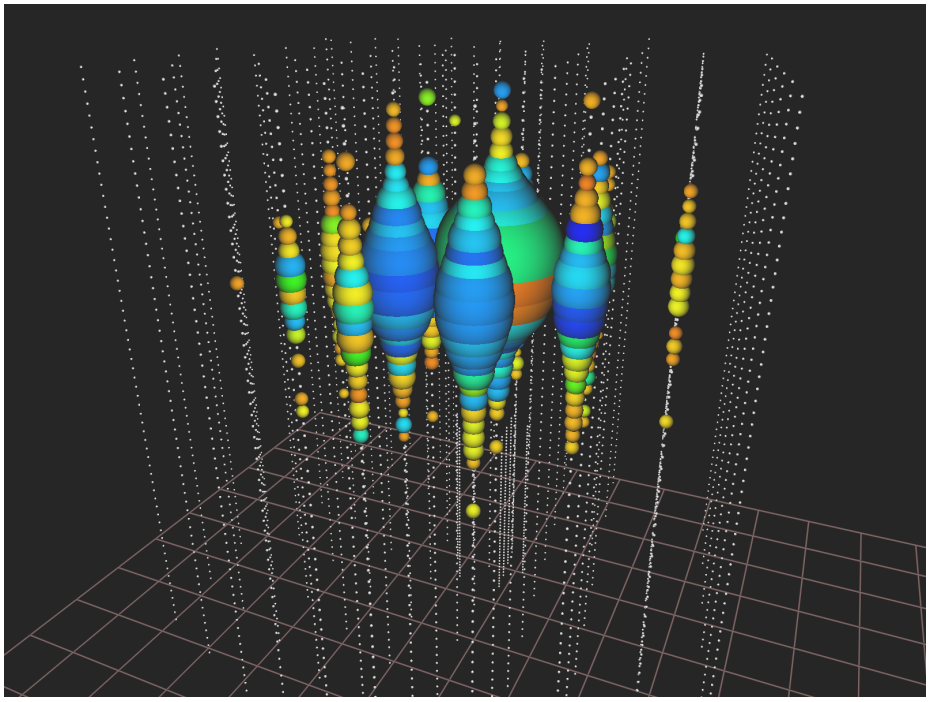

(b) Example cascade event

Figure 5.3: Simulated high-energy neutrino events in the IceCube detector. Each DOM that observes Cherenkov photons is colored across a spectrum of early (red) to late (blue) as a representative timing guide, while the size indicates the charge. The simulated neutrinos generating these distributions undergo different interactions to produce topologically different timing pulses across the DOMs. For the track event (top), a representative arrow is drawn indicating the direction of the original neutrino that produced the muon-track. I created these figures using IceCube software.

5.3.1 Tracks

High-energy muons are able to travel several kilometers before decaying or stopping, which means they produce a *track* of light in the ice while traveling faster than the speed of light. An example of this track-like feature is demonstrated in Fig. 5.3a, including an arrow that represents the path of a muon through the detector. Now, these muons may be produced by a CC-interaction of a neutrino in the ice (see §4.3) or in a cosmic-ray shower which serves as a large background for IceCube. For instance, muons at TeV energies lose energy in the deep antarctic ice via ionization and stochastic losses such as bremsstrahlung, photo-nuclear scattering, and pair production. This can be approximated on average by an analytical approximation as:

$$-\langle dE_\mu/dx \rangle = a + bE_\mu, \tag{5.1}$$

where a is the ionization loss while b is the sum of the stochastic losses. Typical numbers for a muon in ice are $a = 0.246\ \mathrm{GeV/m}$, $b = 0.432\ \mathrm{m}^{-1}$ as per [89]. The muon energy, E_μ, can be estimated by observing the energy losses across the detector. Typically, the range of $1\ \mathrm{TeV}$ and $100\ \mathrm{TeV}$ muons in the ice are $1.8\ \mathrm{km}$ and $10\ \mathrm{km}$. Consequently, these long lever arms of muon tracks are critical for the angular reconstruction of events in IceCube and the typical angular resolution is $\sim 1^\circ$ at 1 TeV and $\sim 0.1^\circ$ at 1 PeV.

Track-like events in IceCube have the added advantage of increasing the effective detector volume. This is because neutrino interactions that occur in the ice outside the physical detector volume can produce a muon that travels through the detector. However, not all energy losses of the muon track can be established in this case, and the reconstructed muon energy is a lower limit to the real muon energy. Therefore, neutrino energy estimation for such an event can have higher uncertainties. Within this subset, there are also the so-called *corner clippers*, which are track-like events going through the detector near the corners.

These kinds of events are notorious for reconstruction algorithms as the lever arms are now reduced, and energy losses occur before and after the muon entered the detector.

5.3.2 Cascades

Electron or tau decay products produced within the detector volume typically have an interaction length that is smaller than the inter-string spacing. For electrons, the interaction length is $\sim 40\ \mathrm{cm}$ in ice whereas for taus, the decay products create a cascade. Therefore the electromagnetic or hadronic shower they create and the consequent distribution of Cherenkov photons arriving in the DOMs are globular shaped. This type of event is called a *cascade* in IceCube. In contrast to track-like events, which are formed due to individual leptons, cascade-like events are created due to an electromagnetic shower that radiates Cherenkov photons spherically from the original interaction vertex. An example of a cascade event is demonstrated in Fig. 5.3b. The amount of light generated per interaction is proportional to the number of shower particles, which in turn is reflective of the original energy for charged current (CC) ν_e, ν_τ interactions. Neutral current (NC) interactions behave similarly, although an outgoing neutrino escapes with a fraction of the original neutrino energy. This means that *contained* cascade events can have their energies reconstructed up to an accuracy of $\sim 10\%$ [90].

While cascade events in IceCube can have better energy reconstruction than tracks, their angular resolution is relatively poor due to spherical symmetry. Therefore cascade events can have angular uncertainty of $\sim 5 - 20^\circ$ and are typically avoided to perform astrophysical point-source studies. However, cascade events are extremely useful for studies of the astrophysical diffuse neutrino flux. For instance, cascades composed of 76% of a 37-neutrino sample across 3 years that was used to identify a high-energy astrophysical neutrino flux for the first time in 2014 [42]. Additionally, above PeV energies, τ particles travel a considerable distance before decaying which is more than the inter-string spacing in IceCube. As a result, high-energy τ's can be identified by a *double-bang* feature wherein

the first bang corresponds to the deep-inelastic scattering (DIS) ν_τ-interaction vertex while the second corresponds to the τ-decay. Interestingly, for a DIS CC ν_τ interaction, if the interaction vertex is outside the detector volume then the τ-decay may look like a μ-track. Additionally, other types of neutrinos can produce a double-bang event in IceCube, such as the Glashow resonance (§4.3.3), and understanding the complexities behind double-bang cascade events also help constrain non-standard astrophysical neutrino-flavor ratios [91].

5.4 Data Acquisition

Armed with the knowledge of how neutrino interactions can be observed with IceCube, we now turn our focus to IceCube's data acquisition system. As a Cherenkov radiation detector, these interactions are observed by a cubic-kilometer network of DOMs in the antarctic ice. Additional triggers and filters are employed as a part of IceCube's data acquisition system to reduce noise and transmit data via satellite to the Wisconsin IceCube Particle Astrophysics Center (WIPAC) from the IceCube Lab (ICL) located at the South Pole. This transmission has a cap of $\sim 100\ \mathrm{GB}$ per day as further processing and analyses are performed at WIPAC. An overview of this extensive and challenging process will be given in this section.

5.4.1 Digital Optical Modules (DOMs)

The fundamental light sensor and data acquisition unit of IceCube is a DOM, as shown in Fig.5.4. This piece of equipment allows for near-autonomous operation after being deployed in the ice. It contains a 10"-inch Hamamatsu downward-facing PMT that is responsible for converting the incoming Cherenkov photons into an analog waveform that represents the PMT electrical current [92]. A 13 mm optical gel is inserted between this PMT and the glass housing it resides in. This glass housing is constructed to withstand the high pressure deep in the antarctic ice. A mu-metal grid of wires is built around the PMT to reduce Earth's magnetic field effects while providing minimal obstruction to its light yield.

The downward-facing orientation of the PMT is chosen in order to maximize IceCube's signal-to-background differentiation, as per expectations from simulations. Additionally, each DOM contains circuit boards within the spherical glass housing that help measure, calibrate, and transmit data as well as communicate with its nearest neighbors.

The 10"-inch Hamamatsu PMTs are designed to detect Cherenkov photons from charged particles (due to neutrino interaction with matter) in the 10 GeV - 10 PeV energy range, from up to 500 meters away. The PMTs have peak quantum efficiency around 25% (34% for HQE) near 390 nm. These PMTs operate at a gain of 10^7 and their waveforms can have amplitudes from $1\ \mathrm{mV}$ - $2\ \mathrm{V}$. Additionally, their widths can be $12\ \mathrm{ns}$ - $1500\ \mathrm{ns}$ so in order to accommodate such a large variety of signals, every DOM includes multiple digitizers with overlapping dynamic range and sampling seeds. After a photon enters the DOM, if the PMT registers a signal greater than 1/4 photo-electrons (PE) then an initial IceCube *hit* is triggered. This hit time as well as the PMT waveform is saved and sent to the surface at the ICL after approximately 1 second. The ICL independently monitors this hit rate every $1.6\ \mathrm{ms}$ in order to be sensitive to a sudden increase in low-energy ν_e events by a Galactic supernova. These PMTs observe noise that is mainly dominated by dark noise at $\sim 300\ \mathrm{Hz}$ for temperatures between -40° and -20°. The aforementioned 0.5"-inch, low-potassium glass housing also serves as a suppression to this ^{40}K decay noise.

Twisted quad cables power and connect each DOM to cables that run up to the ICL. A separate wire connects each DOM to its nearest or next-to-nearest neighbor within that string to check for local coincidences (LC). Included in each DOM are LED flashers that are used for calibration purposes as well as circuitry to help process and digitize the PMT waveforms. The main board of each DOM was designed at the Lawrence Berkeley National Laboratory and controls all devices inside the DOM, while also providing necessary DC power to its subsystems [93]. It is primarily responsible for the digitization of PMT waveforms, PMT gain calibration, and temporarily storing the data while communicating with the ICL. It can also uniquely identify each DOM, exchange timing pulses with the

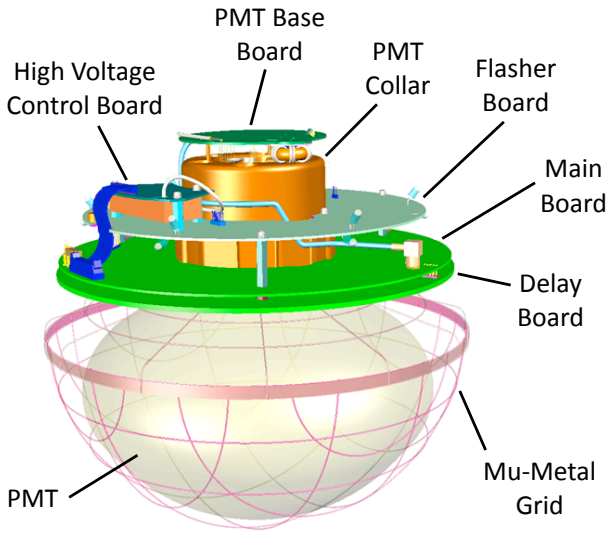

Figure 5.4: A functional diagram of a digital optical module (DOM) that forms the basic detection unit of IceCube. Each DOM is equipped with features that enable it to run calibration tests, measure light deposition information, and transmit information to/from the detector base. This figure is taken from [81].

ICL to calibrate its internal clock, as well as exchanging LC pulses with adjacent DOMs. If the condition for a hit is triggered, then the PMT waveform will be digitized by an Analog Transient Waveform Digitizer (ATWD) as well as a fast Analog-to-Digital Converter (fADC) by the main board. An ATWD is unavailable while digitizing the PMT waveform so each main board has two ATWDs that alternate to minimize deadtime and record for 427 ns at a sampling rate of 300 Msps. The fADC records for a longer duration of 6.4 μs at a sampling rate of 40 Msps. Photons from $\gtrsim 100$ m may arrive over a broader time interval due to the optical scattering of the ice and such signals are also lower in amplitude. So this information is captured in the continuously sampling fADC.

5.4.2 IceCube Triggers

One of IceCube's operation goals is to maximize the detector uptime or the fraction of time the detector is sensitive to neutrino interactions. Therefore, a set of online systems at the detector site oversee the data flow. This consists of a number of steps of data reduction and

selection from photon detection by PMTs in the ice to candidate physics event selection. Each PMT is prone to noise from thermionic emission, luminescence in the glass housing, and radioactive decay among others, and DOM hits are mostly due to dark noise at a rate of 600 Hz. We expect that this noise is *independent* for each DOM. So the first step in data reduction takes place in the DOM, using a Local Coincidence (LC) condition. The PMT dark noise rate is dramatically reduced by requiring a Hard Local Coincidence (HLC), which requires nearest or next-to-nearest DOMs to observe a hit within a configurable time window, set at ± 1 μs. For HLC, the PMT waveform is sent up to the ICL while for other types of hits, called Soft Local Coincidences (SLC), only the time-stamp and charge information is stored.

IceCube triggers typically look for clusters of HLC hits in space and time. The fundamental trigger for IceCube is an algorithm that searches for a multiplicity of HLC hits, known as the Simple Multiplicity Trigger (SMT). This requires $\geq N$ HLC hits within a sliding time window of several μs. This trigger is extended until there is a period of time identical to the initial trigger window where no HLC hits from the relevant DOMs are observed. For instance, the SMT8 trigger applies over a pre-set trigger window of 5 μs for the in-ice DOMs. That is, at least 8 HLC hits have to be recorded for a collection of in-ice DOMs over a period of 5 μs. The SMT8 trigger rate for IceCube is ~ 2.1 kHz, and along with other such triggers brings the online event rate down to $2.5 - 2.9$ kHz. This amounts to ~ 1 TB of raw data per day, while the satellite transmission cap is at 100 GB of data per day. So the data rate at ICL is further reduced by employing additional filters and compression algorithms, each optimized for different data event selection purposes. This filtering is referred to as online filtering as it is performed in realtime at the ICL such as a `MuonFilter` (upgoing tracks to reduce downgoing atmospheric muon background). Due to the high online event rate, event reconstruction algorithms employed at the ICL are often quick and rudimentary to preserve time and computing resources. The transmitted data also contains information about the configuration of the detector over 8-hour periods,

known as runs. This is important for more detailed offline reconstruction algorithms as it uses the detector monitoring information to properly calibrate the data. Offline filtering and reconstructions are performed on the data after they are transmitted and stored on servers.

5.5 Event Reconstruction

The data collected by IceCube includes the energy deposited and the PMT waveforms, with the relevant timing information of these deposits. In order to perform high-level analyses, this data needs to be reconstructed into particle information. A useful thought experiment is to drop objects of different shapes in a bucket of sand, and then guess the object dropped based on the distribution of the sand in the bucket. IceCube uses different methods to reconstruct event information of varying complexity and purpose that intrinsically depend on the kind of event that occurred in the detector. In this section, we shall look at a few important ones relevant to track-like events for point-source studies.

5.5.1 LineFit

By ignoring local ice properties, a quick and rudimentary reconstruction of the lepton (inducing Cherenkov radiation) produced by neutrino interaction can be performed [75]. This reconstruction ignores the geometry of Cherenkov radiation and assumes a plane wave of light propagating perpendicular to the produced lepton momentum. Consider DOMs located at position $\vec{r}_i$ such that the arrival time of photons at that location is t_i. We can then minimize a χ^2 to fit the Cherenkov velocity $\vec{v}$ and the vertex position $\vec{r}$:

$$\chi^2 = \sum_{i=1}^{N_{\text{hit}}} \left(\vec{r}_i - \vec{r} - \vec{v}t_i\right)^2 \tag{5.2}$$

Note that this assumes that light travels a 1D path through the detector such that $\vec{r}_i \approx \vec{r} + \vec{v}t_i$. This can be solved analytically:

$$\vec{r} = \langle \vec{r}_i \rangle - \vec{v} \cdot \langle t_i \rangle \,, \;\; \vec{v} = \frac{\langle \vec{r}_i t_i \rangle - \langle \vec{r}_i \rangle \cdot \langle t_i \rangle}{\langle t_i^2 \rangle - \langle t_i \rangle^2}, \tag{5.3}$$

where $\langle \vec{r}_i \rangle = \frac{1}{N_{\rm hit}} \sum_i^{N_{\rm hit}} \vec{r}_i$ denotes the weighted mean of the DOM positions by the number of hits. This procedure has been improved to penalize late pulses and DOM hits too far away from the event [94]. While the accuracy of this reconstruction is not extraordinary, and it is not used for further event selection it does provide a quick initial seed or guess for more detailed reconstruction techniques used by IceCube.

5.5.2 SplineMPE

A more detailed event reconstruction includes information about the local ice properties and the geometry of Cherenkov radiation [75]. It includes supposing an initial seed for the neutrino direction that can be quickly obtained by, say the line-fit reconstruction. These reconstructions can be generalized to the problem of estimating a set of unknown parameters $\{\vec{a}\}$, e.g. track parameters, given a set of experimental observations $\{\vec{x}\}$. Then, the parameters are determined by a likelihood maximization technique such that:

$$\mathcal{L}(\vec{x}|\vec{a}) = \prod_i p(\vec{x}_i|\vec{a}), \tag{5.4}$$

where $p(x_i|\vec{a})$ is the PDF of the measured value x_i given true event parameters $\{\vec{a}\}$. For tracks, $\vec{a} = (\vec{r}_0,\ \hat{p},\ t_0)$ such that $\vec{r}_0 = (x_0,\ y_0,\ z_0)$ provides the coordinates for any position along the track and $\hat{p} = (\theta,\ \phi)$ are the angular coordinates for the track in the detector. To simplify this discussion, we can assume that the Cherenkov photons observed by the DOMs are due to an infinitely long muon track and forms a cone (see Fig. 4.3 for the Cherenkov geometry). Under this assumption, the muon passes through $\vec{r}_0$ at time t_0 along a direction $\hat{p}$. For this infinite-track assumption, a simplistic reconstruction method would

rely only on the arrival times of the first photo-electron (PE) at each DOM. Assuming this PE undergoes minimal scattering, this type of reconstruction is referred to as single-photo-electron (SPE) reconstruction. An analytical function can be constructed based on the distribution of residuals, $t_{\rm res} \equiv t_{\rm hit} - t_{\rm geo}$, which is the difference between the observed hit time and the time expected from a direct photon[4] [95]. A simple parameterization of this analytical function is often referred to as the Pandel function in literature and describes this timing distribution more accurately; while the LineFit reconstruction does not take time delays into account at all.

Ideally, the $t_{\rm res}$ distributions should be a delta function. However, in a realistic experimental situation, this distribution is broadened and distorted by several effects including jitter, Gaussian noise, and dark noise. For a high-energy muon passing through the detector, each DOM can detect multiple PEs and this information can be vital to reconstruct the event. This modified likelihood that incorporates the Pandel function integrated analytically over $t_{\rm res}$ is based on the multi-PE (MPE) time PDF, and is called the $\mathcal{L}_{\rm MPE}$. This model includes the ice model parameters to calculate how scattering affects the arrival time distributions. Photon transport simulations are computed based on the ice model, such as SpiceMIE, by tabulating the timing distributions and light yield for different configurations. These photon tabulations are used by a `photo-spline` package that fits a multi-dimensional spline [96]. This spline can be computed analytically using the photon tables and is directly used in $\mathcal{L}_{\rm MPE}$ to form the SplineMPE reconstruction technique.

5.5.3 Paraboloid

In general, reconstruction techniques are expected to deviate from the true neutrino directions that interact and trigger the detector. For high-level analyses, it is important to have an estimate of this angular uncertainty on a per-event basis, within a certain confidence level. One such method that is used in IceCube to estimate the angular uncertainty of the

[4]Muon to DOM without scattering

reconstruction is Paraboloid. As we saw with SplineMPE, event reconstructions in IceCube are often likelihood-based, and the resulting best-fit event parameters offer minimal insight without an evaluation of the uncertainties in those parameters. The Paraboloid method evaluates this angular uncertainty estimate by utilizing the $1\ \sigma$ contour around the likelihood maximum. This contour, when projected to a 2D angular space, typically zenith and azimuth, forms an elliptical shape. That is, this 2D slice of a paraboloid likelihood map is an ellipse. The axes of this ellipse, σ_1 and σ_2, are then used by this method to evaluate a per-event average angular uncertainty estimated circular error as follows:

$$\sigma_{\mathrm{err}} = \sqrt{\frac{\sigma_1^2 + \sigma_2^2}{2}} \tag{5.5}$$

Upon comparing this estimated error to the actual error for simulations, it was found that it is systematically underestimated. This is because this method assumes normal uncertainties in the ice model parameters used to perform the reconstruction. Additionally, this estimate cannot take into account the offset between the incoming neutrino and outgoing muon that forms the track-like event in the detector. Consequently, a *pull-correction* is performed wherein σ_{err} is scaled and adjusted based on simulations. Pull-correction is performed by fitting the ratio of muon track error and true error, as a function of the reconstructed energy, to take into account systematic and kinematic uncertainties.

5.5.4 Energy Reconstruction

As demonstrated previously in §5.3.1, it is challenging to reconstruct the true neutrino energy for tracks mainly because information about the neutrino interaction is unknown. For instance, a track could be a cosmic-ray-induced muon or a CC neutrino interaction near the detector. Therefore *through-going* tracks can have energy losses that are unaccounted for outside the detector and the energy estimate is only a lower limit on the true neutrino

energy. Additionally, the muon energy must be estimated from the properties of the deposited light such as the differential energy loss rate, or dE/dx. Cascade events, on the other hand, that are contained within the detector have better energy uncertainty estimates of up to 15%.

For tracks, energy estimates are calculated assuming that the total light yield from the detected photons is directly proportional to the event energy [90]. At low energies ($\lesssim 100$ GeV), the range of muons in ice is short enough to use a calorimetric approach as almost all of the muon energy is deposited in the detector. For high-energy muons, the expected light output of simulated events ("template") has to be evaluated by segmenting the track as individual sources. In general, the number of detected photons is expected to follow a Poisson distribution with mean $\lambda = \Lambda E$. This is done to compare the observed mean being λ for energy deposition E to the template expectation of Λ photons per-unit energy. By including the contribution from noise hits as ρ, the mean number of expected photons is:

$$\lambda = \Lambda E + \rho \tag{5.6}$$

Since the expected number of photons observed per DOM is low, we utilize Poisson statistics to form a likelihood. For the observation of k_i photons at the i^{th} DOM, this likelihood is given by:

$$\mathcal{L} = \prod_i \frac{\lambda_i^{k_i}}{k_i!} \cdot e^{-\lambda_i} \tag{5.7}$$

$$\mathcal{L} = \prod_i \frac{(\Lambda_i E + \rho)^{k_i}}{k_i!} \cdot \exp\left(-\Lambda_i E + \rho\right) \tag{5.8}$$

A maximization of this likelihood is performed to estimate the most probable energy

scaling E given the distribution of observed photons at each DOM, which is then used to estimate the energy of the muon when it enters the detector. This technique is referred to as the MuE algorithm that has been improved by applying a kernel function $G(\lambda_i,\ \lambda_j)$ and a modified likelihood [90]:

$$\mathcal{L} = \prod_j \int_0^\infty G(\lambda_i,\ \lambda_j) \cdot \frac{\lambda_i^{k_i}}{k_i!} \cdot e^{-\lambda_i}\, d\lambda_i \tag{5.9}$$

5.6 Event Simulation

As previously described, IceCube uses Monte Carlo simulations to evaluate the performance of several data acquisition tasks, as well as for high-level analyses. These simulations have been developed over the years to take into account several factors including the atmospheric muon and atmospheric neutrino backgrounds, as well as their propagation through the ice as well as the Earth including the atmosphere. The air-shower simulation code, CORSIKA, is used to generate the atmospheric muon backgrounds [97]. Neutrino event simulations are done by GENIE [98] and Neutrino Generator (NuGen). The latter is a modification to the ANIS simulation code [99]. NuGen only considers deep inelastic scattering process for the neutrino-matter interaction. While this works for most high-energy neutrino events above $\gtrsim$ 100 GeV, GENIE is used for simulating lower-energy neutrino events in the detector as it also includes other scattering interactions.

Because all analyses presented in this dissertation use high-energy neutrino data, NuGen simulations are of particular interest. These use the preliminary Earth model [100] to evaluate the propagation and interaction of high-energy neutrinos through the Earth. Because the neutrino interaction probability is so low, these simulations use importance sampling. Each simulated neutrino is forced to interact and a weight, that includes the interaction and propagation probabilities, is calculated. This final weight, called OneWeight, can then be applied to the simulated events with the appropriate signal (astrophysical) or back-

ground (atmospheric) spectra to calculate the observable flux. Background events are also simulated using `NuGen` for atmospheric neutrinos and `CORSIKA` for atmospheric muons. Muon propagation through the ice is simulated using the Muon Monte Carlo (`MMC`) code [101]. Photon propagation and detection are done by `CLSim` or Photon Propagation Code [102] [103]. Finally, real-time trigger filters and noise are applied to the simulated data, allowing an analysis to be replicated with the simulation of both signal and background.

5.7 Data Samples

The analyses presented in this dissertation utilize three high-level IceCube data samples, that prioritize event selections for ν_μ-induced track-like events in slightly different ways. This is because track-like events offer a better angular resolution, compared to their cascade counterparts as we saw in §5.3, and better angular resolution allows for the astrophysical point-source searches. However, atmospheric muons and atmospheric neutrinos, induced by cosmic-ray air showers dominate the data transmitted via satellite from ICL (IceCube Lab at the South Pole) to WIPAC (Wisconsin). For events that are anticipated to have already passed through the Earth, there is a significant presence of muon contamination caused by inaccurately reconstructed event directions. To identify potential astrophysical neutrino sources, the final selection of events for the samples presented here meets the following requirements: a) maximize the number of astrophysical neutrino events, b) minimize the interference of background events, and c) ensure high-quality direction reconstructions.

For each data sample utilized in this dissertation, the selection begins at the SMT8 trigger level with quick reconstructions (SPE, LineFit) applied at the South Pole, along with the `MuonFilter` that brings the rate down to ~ 40Hz as referred to in §5.4.2. The frequency of events passing through the `MuonFilter` is low enough for daily satellite transfer. This is crucial for offline analysis and allows for more sophisticated reconstructions to be carried out for subsequent online analysis. If an event passes at least one filter, the set of extracted

Data Sample (IC86 config.)	Livetime (years)	Start (UTC)	Stop (UTC)	Northern sky event rate (per year)	Uptime
GFU (v02p05)	7.17	2011-05-13	2018-10-14	1.25×10^5	96.5%
PS Tracks (v04p01)	8.72	2011-05-13	2020-05-29	9.1×10^4	96.3%
Northern Tracks (v05p00)	8.73	2011-05-13	2020-05-29	7.6×10^4	96.4%

Table 5.3: A summary of the pre-curated, high-level data samples observed by the IceCube detector used for analyses presented in this dissertation. The northern celestial sky is defined as declinations above $\delta > -5^\circ$, as per the Earth's geometry and location of the detector at the South Pole. Sample names and version numbers, referred to internally within the collaboration, are provided for reference.

pulses is transmitted via a satellite link, which has a bandwidth allocation of approximately 100 GB per day, to WIPAC. Additionally, as an extra precaution against processing errors, the raw waveforms for every triggered event are stored on hard disks at ICL and sent to WIPAC once a year.

After a few seasons of data collection, the final-level data samples are updated internally for high-level analyses within the IceCube collaboration. These updates include, for instance, an updated ice model for more accurate event reconstructions, additional data as they are processed, or bug fixes in the processing scripts. The primary requirement of all analyses in this dissertation, along with the aforementioned ones for point-source searches, is to include time dependence by utilizing event timing information. So each sample was chosen to meet an additional requirement, which is little to no gaps between the data collecting seasons for the final level samples. All samples analyzed in this dissertation have near-continuous sampling across the data-taking period. These samples are summarized in Table 5.3 and are mainly dominated by ν_μ-induced tracks.

While there are minimal differences between the samples and their event selections are based on Boosted Decision Trees (BDTs). The Gamma-ray Follow Up (GFU) sample has a slightly looser BDT cut than the Point-Source Tracks (PS Tracks) for instance, consequently the former has a higher event rate. Additionally, the IceCube collaboration has performed different types of point-source searches with each of these samples and their

corresponding event selections. While the sensitivity of a point-source search depends on the method being applied, for now, the performance of each sample can be evaluated by considering two quantities:

- Effective area: For a specified astrophysical flux of neutrinos, the effective area provides a direct way to evaluate the data selection and calculate the number of observable neutrinos from that source. That is, the effective area refers to the surface area that a detector with perfect efficiency would have. For identical detector configurations, different data selection schemes can be evaluated by this quantity. Typically, it is a function of the neutrino energy and the declination of the source, and relates to the flux in the following way:

$$N_\nu = \text{livetime} \cdot \int_{E_\nu} A_{\text{eff}}(E_\nu,\ \delta) \frac{d\Phi_\nu}{dE_\nu}\, dE_\nu \tag{5.10}$$

- Angular resolution: For simulated neutrino events that undergo the same selection criteria as the data sample, the angular separation of the true neutrino direction to the reconstructed one should be low $< 10^\circ$. For simulated true neutrino coordinates, $(\delta_{\text{true}},\ \alpha_{\text{true}})$ and reconstructed coordinates $(\delta_{\text{reco}},\ \alpha_{\text{reco}})$, this separation is:

$$\Psi(\text{true}, \text{reco}) = \cos^{-1}\left[\sin\delta_{\text{true}} \sin\delta_{\text{reco}} + \cos\delta_{\text{true}} \cos\delta_{\text{reco}} \cos\left(\alpha_{\text{true}} - \alpha_{\text{reco}}\right)\right] \tag{5.11}$$

5.7.1 GFU

The selection criteria for the GFU sample were originally designed by Dr. Thomas Kintscher as a part of their Ph.D. dissertation [104]. While the primary goal was to build an effective online data selection method for γ-ray follow-up studies, it adds the `GFUFilter` on top of the `OnlineL2` filter. The latter reduces the event rate down to ~ 6 Hz from the `MuonFilter`, by adding a SplineMPE reconstruction to the event and performing addi-

tional muon rejection. The `GFUFilter` uses separately trained BDTs (north/south) to for performance cuts. The final-level (sometimes referred to as the GFU-Offline) sample is predominantly composed of track-like events. It uses the SplineMPE direction and MuEX energy reconstruction methods while utilizing the Paraboloid angular uncertainty estimation that was described in 5.5. The data are dominated by atmospheric neutrinos in the northern celestial sky ($\delta > -5^{\circ}$). Most recently, this data sample was utilized by Dr. Chun Fai Tung to search for periodic neutrino sources as a part of their Ph.D dissertation [105].

By applying identical event selections and reconstructions to Monte Carlo (MC) simulations of neutrino events, the performance of this data sample is shown in Fig. 5.5. Firstly, as the effective area is a function of declination and neutrino energy, it is evaluated for equal $\sin\delta$ bins in the northern hemisphere as a function of simulated true neutrino energy in Fig. 5.5a. The rise in the effective area is indicative of IceCube's performance for high-energy neutrino sources, as the data are severely background dominated at lower energies $\lesssim 100$ TeV. Additionally, the northernmost declination bins contain events passing through more of the Earth's core so the survival probability is lower due to Earth's attenuation at higher neutrino energies. As previously discussed, it is important to evaluate the sample's angular error using MC simulations and this is shown for the northern sky in Fig. 5.5b. Note that this error does not include systematic effects due to uncertainty in the ice properties used for the reconstructions.

5.7.2 PS Tracks

The selection criteria for the point-source (PS) Tracks sample were originally designed by Dr. Stefan Coenders [106], and updated by Dr. Tessa Carver [107] as a part of their Ph.D. theses. This selection is maintained by Dr. Michael Larson at the University of Maryland. The primary goal was to create an all-sky sample of ν_{μ}-induced tracks optimized for point-source searches. It has a slightly reduced event rate compared to the GFU sample due to tighter BDT cuts in the northern and southern celestial sky. Another difference is that the

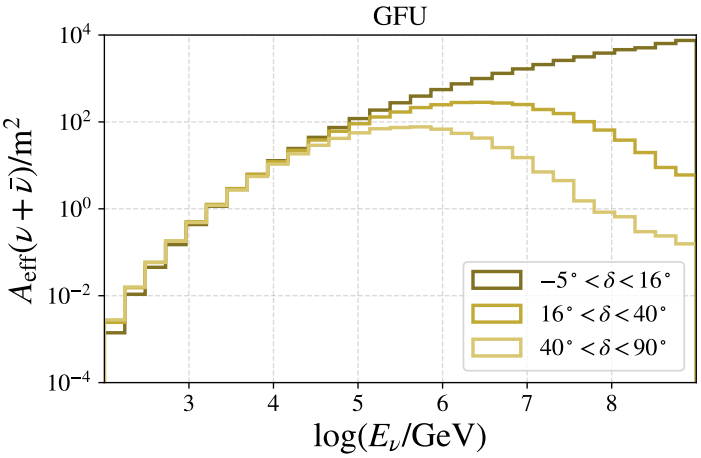

(a) Effective area

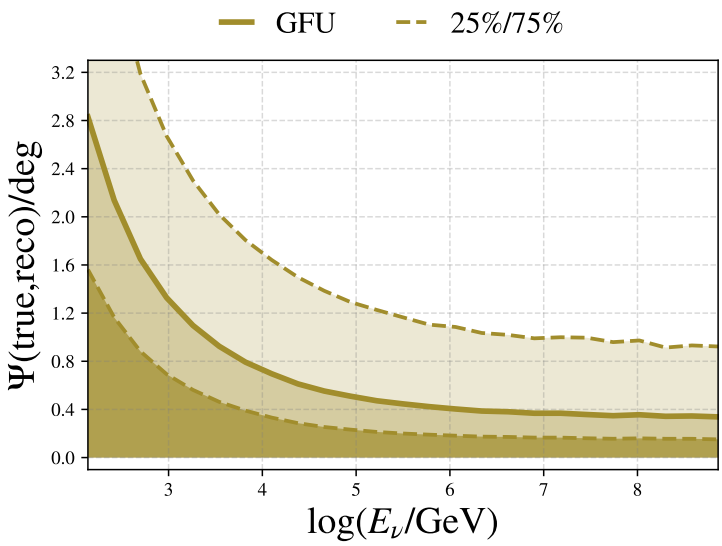

(b) Angular error

Figure 5.5: Point-source performance metrics for simulated events that pass the same selection criteria as the GFU sample summarized in Table 5.3. The top panel displays the GFU effective area as a function of simulated true neutrino energy, in equal $\sin\delta$ bins in the northern celestial sky. The bottom panel displays the distribution of the GFU angular error as a function of simulated true neutrino energy, with the median in solid and the $25\% - 75\%$ quantiles in dashed lines. I made these plots using IceCube software.

SplineMPE reconstruction is applied again by using the previous iteration's likelihood map as a seed. This sample also uses the MuEX energy reconstruction method. In 2021, this selection was employed as part of IceCube's public data release from 2008-2018 [108]. This data release was internally versioned as PS Tracks v03p02. The analysis presented in this dissertation utilizes PS Tracks v04p01 and contains 2 additional years of data. The notable changes are the reprocessing of data collected after 2011, including revisions to the calibration of the PMT charge response and newer glacial ice models [109] [2]. A prior version of this sample, PS Tracks v03p00 (2008-2018), was analyzed by Dr. Tessa Carver to find a time-integrated astrophysical signal excess over the background at 2.9σ level for the Seyfert II galaxy NGC 1068 .

The performance of this updated data selection criteria is shown in Fig. 5.6, similar to the GFU sample previously 5.7.1. This utilizes simulated events that have identical event selections and reconstructions as the PS Tracks (v04p01) sample referred to in Table 5.3. Compared to the GFU sample, while the angular uncertainty is slightly higher for the lowest energy events, it is comparable for simulated true neutrino of $\geq 10^3$ GeV. In fact, it performs slightly better at the higher neutrino energies of $\geq 10^7$ GeV as seen in Fig. 5.6b. As systematic effects due to uncertainties in the ice properties are not included, the angular error is underestimated. To tackle this, a 0.2° floor is applied by all high-level IceCube point-source searches, including the ones presented in this dissertation. The main advantage of this sample over the GFU sample is the extended years of data available, particularly from 2018-2020.

5.7.3 Northern Tracks

The selection criteria for the Northern Tracks sample were originally developed by Dr. René Reimann [110], and recently updated and maintained by Dr. Hans Niederhausen. The primary goal of this selection criteria was to have a high-purity northern sky sample of ν_μ-induced tracks, that can also be used for measurements of the diffuse astrophysical neutrino

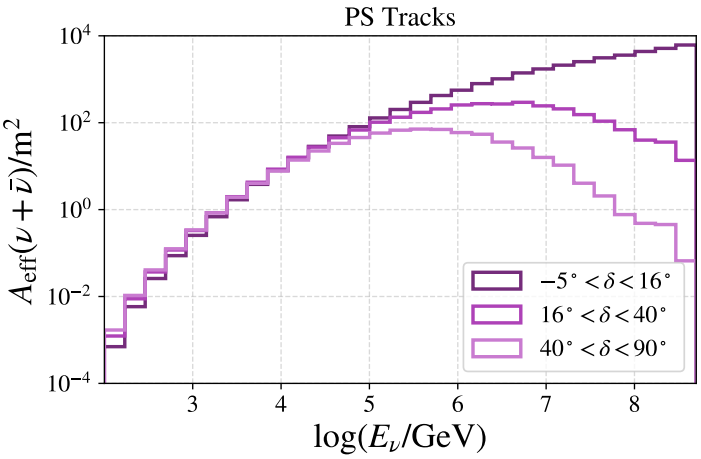

(a) Effective area

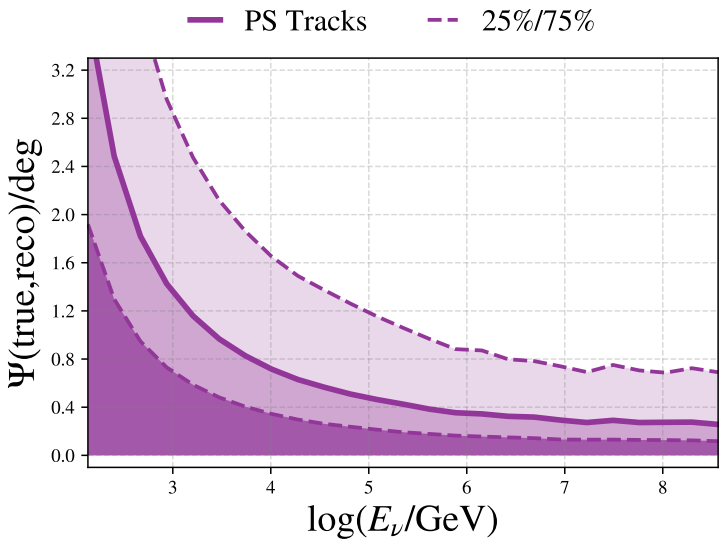

(b) Angular error

Figure 5.6: Point-source performance metrics for simulated events that pass the same selection criteria as the PS Tracks sample summarized in Table 5.3, similar to Fig. 5.5. I made these plots using IceCube software.

flux. The updated selection uses a new and improved muon energy estimator using Deep Neural Network (DNN) [111], and replaces a traditional likelihood-based muon energy estimator referred to as `TruncatedEnergy` [90]. The DNN energy estimator also uses more timing information at the DOMs as opposed to only using the total deposited charge at the DOMs, and particularly improves the energy estimation of the muon at low energy ($\leq 10^3$ GeV), while also having a smaller spread around the true muon energy as shown in Fig. 5.7.

More recently, IceCube reported evidence of time-integrated neutrino emission from NGC 1068 [2] that used an improved Northern Tracks sample, versioned internally as v05p00. This result served as the primary motivation for choosing this data sample for my time-variability analysis presented in Chapter 6. Additionally, the angular uncertainty estimation was improved for this sample by using a BDT instead of the regular Paraboloid method. This BDT was trained using `LightGBM` [112] and used 17 variables. The variables used to train the BDT on simulated data included total energy and stochasticity of the muon track's energy losses, the position in the detector where most photons were deposited, the declination of the muon track, the pull-corrected paraboloid angular uncertainty estimate, among others. To summarize, not only was the energy estimation improved but also the angular uncertainty estimation compared to the PS Tracks and GFU data samples. As we shall see in 5.8.2, improvements were also made to the point-source likelihood method by utilizing a new IceCube framework, `SkyLLH` [113] for the aforementioned NGC 1068 result with this sample.

5.8 Point-Source Methods: Unbinned Maximum Likelihood Search Method

Maximum likelihood estimation (MLE) is a statistical method used to estimate the parameters of a statistical model or hypothesis by finding the parameter values that maximize the likelihood ($\mathcal{L}$) function of the observed data. The basic idea of implementing a hypothesis test with MLE is to compare the likelihood of the observed data given the assumed

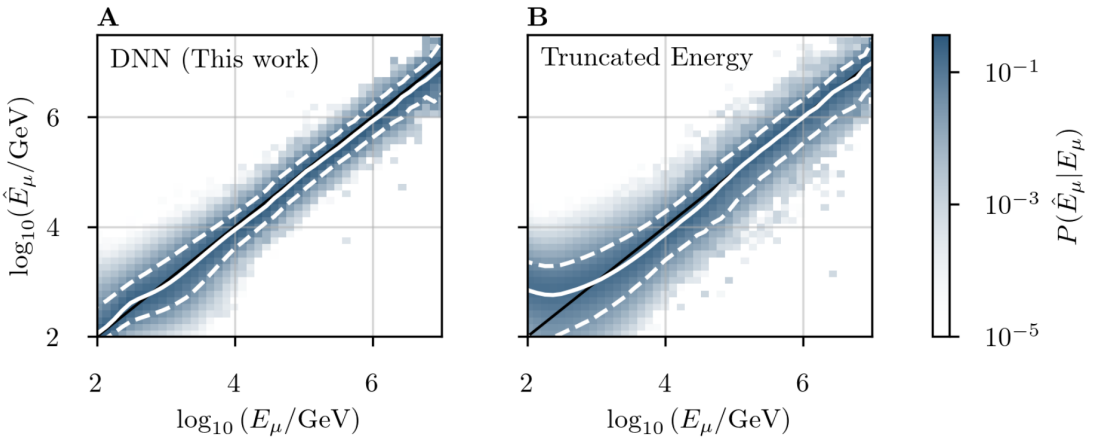

Figure 5.7: Comparison of muon-track energy estimation methods for the improved Northern Tracks sample, by using simulated muons in the IceCube detector. The true muon energy is plotted on the x-axis and compared to the reconstructed muon energy on the y-axis, with the diagonal black line representing an ideal estimation, $E_\mu = \hat{E}_\mu$. The improved estimation using a Deep Neural Network is shown in the left panel, while the right panel shows a previously applied likelihood-based estimating method called `TruncatedEnergy`. The figure is taken from a recent IceCube study that showed evidence of neutrino emission from NGC 1068 [2].

model or hypothesis (the "alternative" hypothesis) to the likelihood of the observed data given a simpler or more restrictive model (the "null" hypothesis). Hypothesis testing using MLE assumes that the likelihoods of the alternative (H_1) and null (H_0) hypotheses are well-defined and that the models are correctly specified. In this section, I will describe the procedure of applying this statistical method to find a point source with IceCube data [114].

At any given point in the celestial sky, we can define a test statistic to measure the two hypotheses using a standard log-likelihood ratio test statistic:

$$\lambda = \mathrm{TS} = 2\log\left[\frac{\mathcal{L}\left(\mathrm{data}|\mathrm{H}_1\right)}{\mathcal{L}\left(\mathrm{data}|\mathrm{H}_0\right)}\right] \tag{5.12}$$

The hypotheses for any given celestial coordinates are defined as follows:

- H_0: Data consists solely of background (atmospheric neutrino events)
- H_1: Data consists of background as well as signal (astrophysical neutrino events from a neutrino point-source)

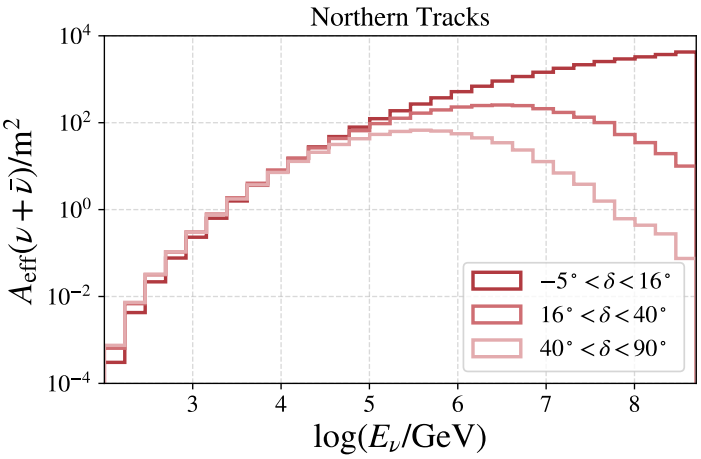

(a) Effective area for the Northern Tracks sample described in Table 5.3.

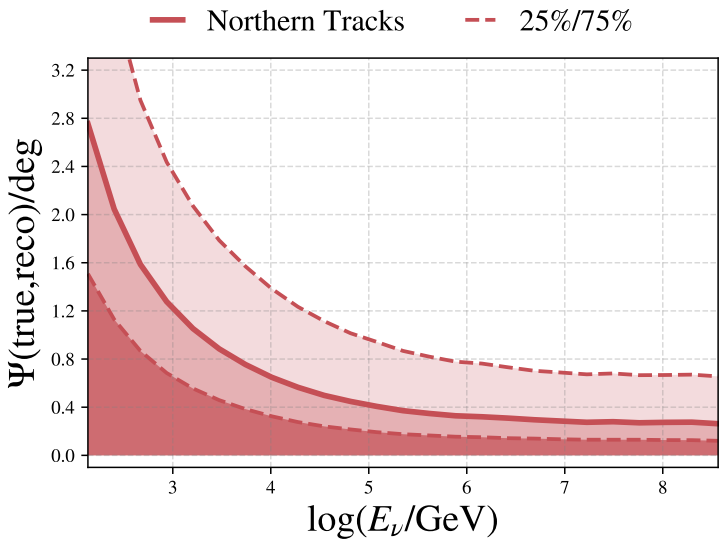

(b) Angular error for the Northern Tracks sample described in Table 5.3.

Figure 5.8: Point-source performance metrics for simulated events that pass the same selection criteria as the Northern Tracks sample summarized in Table 5.3, similar to Fig. 5.5. I made these plots using IceCube software.

Larger values of λ indicate that the data are less-compatible with the background-only hypothesis (H_0). See that H_0 is a subset of H_1 where no signal exists, so these are nested hypotheses. This added structure allows us to invoke Wilk's theorem [115], and reduce computational time for background-only trials, as we will see later.

5.8.1 Likelihood

We want to set up the likelihood with relevant information which can distinguish between background and signal. This includes spatial, energetic, and arrival time information for each event observed by IceCube as described below:

- Angular Distribution: We expect signal events to cluster near the direction of the astrophysical neutrino source
- Energy Distribution: We expect the differential energy spectrum of the signal from Fermi acceleration mechanisms to be close to E^{-2}, while the background is $\sim E^{-3.7}$ above 1 TeV
- Timing Distribution: We expect a characteristic timing profile for signal (flare, periodic, burst), while the background is mostly constant

Additionally, we can define the parameters of our likelihood as the number of signal events (n_s), and the number of background events (n_b), such that $N = n_s + n_b$ is the total number of events. Poisson fluctuations can be included with an extra term in our likelihood, but let us continue with this simplistic case. Additional parameters can be specified which specify H_1, such as the energy and timing distributions. These parameters typically depend on the signal model and can be simple (e.g. single spectral index for a power-law flux, the time window of search) or a bit more complex (e.g. broken power-law requiring two parameters, periodic signal requiring two or more parameters), but the basis of most point-source analyses is built on keeping at least one n_s free parameter.

$$\mathcal{L}(n_s, \ldots) = \prod_{i=1}^{N} \left[\frac{n_s}{N} \mathcal{S}_i + \frac{n_b}{N} \mathcal{B}_i \right] \tag{5.13}$$

$\mathcal{S}_i$, $\mathcal{B}_i$ are signal and background PDFs respectively which are built based on the aforementioned distinguishing properties. Typically, this is written as a product of the individual spatial, energy, and time PDFs:

$$\mathcal{S}_i = \Theta_i^s \cdot \mathcal{E}_i^s \cdot \mathcal{T}_i^s \tag{5.14}$$

$$\mathcal{B}_i = \Theta_i^s \cdot \mathcal{E}_i^b \cdot \mathcal{T}_i^b \tag{5.15}$$

Consider the case where a $\vec{x}_s = (\alpha_s, \delta_s)$ is the source location, $\vec{x}_i = (\alpha_i, \delta_i)$ is the reconstructed direction of the muon track (produced by a neutrino), E_i is the reconstructed muon energy and the source flux is modeled by an unbroken power-law with one parameter: $dN/dE \propto E^{-\gamma}$. We will revisit the temporal PDFs later but let's consider a **time-integrated point-source search**, but this specific scenario has two fit parameters, namely $n_s,\ \gamma$, for a hypothesized source location $\vec{x}_s$ and the PDFs are as follows:

$$\mathcal{S}_i(E_i, \vec{x}_i) = \Theta_i^s(\vec{x}_i | \vec{x}_s, E_i) \cdot \mathcal{E}_i^s(E_i, \sin\delta_i, \gamma) \tag{5.16}$$

$$\mathcal{B}_i(E_i, \vec{x}_i) = \Theta_i^s(\vec{x}_i | \mathrm{bkg}, E_i) \cdot \mathcal{E}_i^b(E_i, \sin\delta_i) \tag{5.17}$$

5.8.2 Spatial PDFs

The spatial part of the signal PDF is based on the assumption that the angular uncertainty of an event (σ_i), which is calculated during the reconstruction (see §5.5.3), corresponds to a 1σ (68%) probability region for the event direction. This true point-spread function (PSF) of neutrino events can be approximated by a 2D Gaussian (Rayleigh distribution). While this works fairly well for high-energy events ($E_i > 10$ TeV), it has been shown that

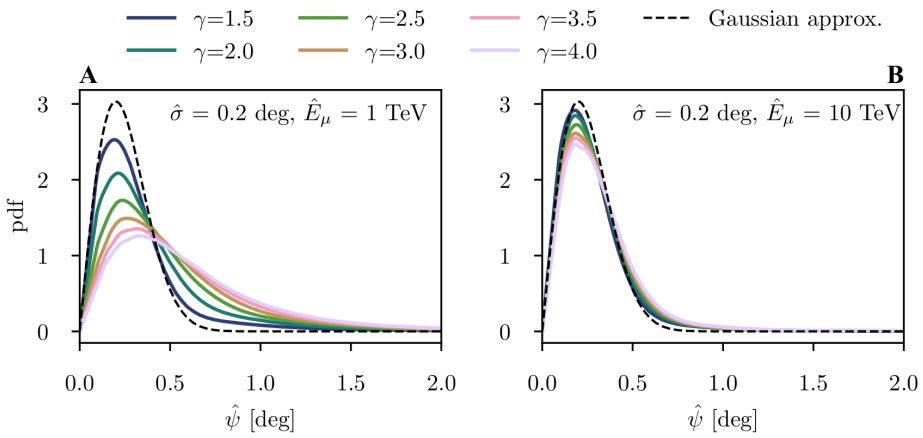

Figure 5.9: A comparison of point-spread functions (PSFs) as functions of spectral index γ using KDEs. These distributions of angular distances (ψ), given an angular uncertainty of $\sigma = 0.2°$, are shown for 1 TeV (left) and 10 TeV (right) muon energy and multiple spectral-index γ. The 2D Gaussian (Rayleigh distributions) are shown in a dashed-black line. The figure is taken from a recent IceCube study that showed evidence of neutrino emission from NGC 1068 [2].

the spatial PDFs can be carefully crafted by an index-dependent Kernel Density Estimation (KDE) that describe low-energy events with a softer index better [2]. This is shown in Fig. 5.9 and the non-Gaussian tails are inadequately described for a 1 TeV muon track.

This treatment of using KDEs to evaluate the spatial PDFs has been applied for the 8.7-year Northern Tracks sample using a new IceCube framework, `SkyLLH`, [113][2] and is an important step towards improving future point-source searches. For the sake of completeness, let us consider the 2D Gaussian PDF:

$$\Theta^s(\vec{x}_i|\vec{x}_s, E_i) = \frac{1}{2\pi\sigma_i^2(E_i)} \exp\left(-\frac{|\vec{x}_s - \vec{x}_s|^2}{2\sigma_i^2(E_i)}\right) \tag{5.18}$$

$$\Theta^b(\vec{x}_i|\vec{x}_s) = \frac{\mathcal{P}_b(\sin\delta_i)}{2\pi} \tag{5.19}$$

The background spatial PDF only depends on the declination component, δ_i, of the event direction. For sufficiently long time scales, the spatial PDF for the background is uniform as the Earth's rotation smears any R.A. dependency.

5.8.3 Energy PDFs

The effective area of IceCube varies with the declination (δ_i) and energy (E_i) of events. The atmospheric background energy spectra are known and expected to be constant, that is the background energy PDF ($\mathcal{E}^{\downarrow}$) is evaluated by choosing appropriate binning in $\sin\delta$ and $\log(E_{\rm reco})$ for a given data sample. The signal energy PDF is modeled by an unbroken power law with a free parameter, γ, and is non-trivial to construct. For a given astrophysical source flux: $dN/dE \propto E^{-\gamma}$, a map is generated with *fixed* spectral indices in the range $[1, 4]$ that weighs each event to populate a 2D PDF as a function of declination and energy relative to the background PDF. This 2D map evaluates the relative signalness of events as a function of declination and energy, for multiple indices in the aforementioned range. When evaluating the likelihood of a point source, a single spectral index (typically $\gamma = 2$) is used in the energy PDF calculation. That is, the likelihood maximization procedure then interpolates between these maps when fitting γ.

5.8.4 Test Statistic

We now return our focus to the test statistic (TS) as defined in Eq. 5.12. In order to evaluate the TS, we need a search location in the celestial sky to compare two aforementioned hypotheses: H_0 and H_1. For a point-source search utilizing the likelihood described in Eq. 5.13, we can rewrite Eq. 5.12 in terms of the free parameters as:

$$\mathrm{TS} = 2\log\left[\frac{\mathcal{L}(\hat{n}_s, \hat{\gamma})}{\mathcal{L}(n_s = 0)}\right] \tag{5.20}$$

That is, the ratio of the maximum likelihood functions with the best-fit parameters $n_{\rm fit} = \hat{n}_s$ and $\gamma_{\rm fit} = \hat{\gamma}$ over the likelihood function of background only where $n_s = 0$, is defined as the test statistic for time-integrated point-source searches in IceCube. In order to perform this maximization procedure, typically events are selected in a $10^\circ \times 10^\circ$ box

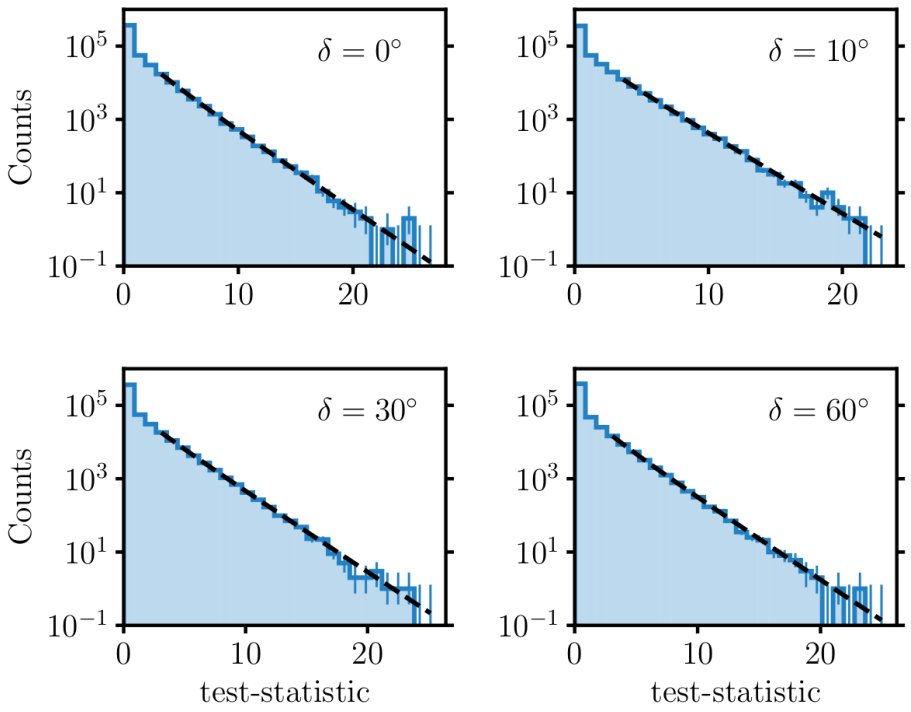

Figure 5.10: Example background-only TS distributions at test declinations for a time-integrated point-source search. The figure is taken from a recent IceCube study that showed evidence of neutrino emission from NGC 1068 [2].

around the search location, to ensure efficient use of time and computational power. Note that the signal spatial PDF (Θ^s) ensures that events outside this region do not contribute much to this likelihood maximization. For a selection of events and a source location, a minimization of $-\mathrm{TS}$ yields the best-fit parameters. The parameters are typically constrained in the minimization procedure, such that $n_s \geq 0$ and $\gamma \in [1, 4]$. The minimization is performed by using the `L-BFGS-B` algorithm offered by the `scipy` package [116] or `migrad` algorithm offered by the `iminuit` package [117] [118]. Over the years, different IceCube packages have been developed to perform this calculation, including `SkyLab`, `csky`, and `SkyLLH`, that offer added functionality and have been extensively tested so that they yield compatible results for a time-integrated point-source search[5].

To test the null hypothesis, a background-only sample is used where it is known that there are no point sources (ns=0). To create such a sample, the true (reconstructed) event

[5]For identical data samples and search location

information, except for the right ascension (RA), is used. Assuming the event selection is uniform in RA and background-dominated, a random RA value between 0 and 360 degrees is assigned to each event. This process scrambles any events clustered around a point-like neutrino source, which are assumed to be few in number and have a negligible impact on the total number of events within a certain declination bin. After assigning random RA values to all events, the data is considered scrambled and blind to any astrophysical neutrino signal. One background trial consists of one copy of the data sample with scrambled RA values. To create multiple background trials, new random RA values are assigned to each event, and the scrambling process is repeated for each trial. To search for an astrophysical signal in the sample, the true RA event information is used to unblind the data.

To test the performance of such a search, a known astrophysical signal corresponding to the signal hypothesis $\mathcal{H}_1$ can be injected before unblinding the data. This is achieved by generating a background trial as per the aforementioned RA scrambling and adding simulated muon neutrino events based on the spectrum of the signal hypothesis. The likelihood method remains identical for blind background trials, blind background trials with injected signal, and unblinded data. After maximizing the likelihood to calculate a TS, larger TS values correspond to cases where the signal hypothesis is much more likely than the background-only hypothesis. However, $\mathrm{TS} = 0$ from the best fit can occur due to $n_s = 0$. It is statistically expected that there will be roughly an even split between over-fluctuations and under-fluctuations around $\mathrm{TS} = 0$. The former could be due to random spatial clustering or high-energy events in the tested source direction, and it should follow a χ^2-distribution with n degrees of freedom according to Wilk's theorem [115]. Since such a search includes n_s and γ as free parameters, there is a partial correlation between them. That is, a higher n_s typically requires a softer spectrum to fit the same data, which results in a degree of freedom between 1 and 2. Typically, the TS under-fluctuations are set to 0 because the minimizer does not allow fits of $n_s < 0$. As a result, there is a large peak in the distribution where $\mathrm{TS} = 0$, often referred to as the delta in the χ^2 distribution.

The TS obtained is used to determine a *p-value*, which estimates the probability of finding an equal or larger TS value than that of the observed data, assuming a background-only scenario at a specific location. The resulting value is then compared to a TS distribution generated from background trials at the same declination. The probability that the observed result could be attributed to background alone is equal to the fraction of the distribution above the observed TS value. This can be determined either by directly taking the fraction of background trials or by integrating a fit function of the distribution. Sample χ^2 fits along with the background-only TS distributions are shown in Fig. 5.10. Additionally, a per-event $\log(\mathcal{S}/\mathcal{B})$ is a useful quantity to rank the contribution of events to the time-integrated TS. This is calculated by evaluating the signal and background PDFs for Eq. 5.17 by using the best-fit spectral index in the energy term. This ranking is particularly useful for evaluating time-dependent analyses and will be referred to in upcoming chapters.

CHAPTER 6

TAUNTON - A SINGLE-HYPOTHESIS TEST FOR ARBITRARY TIME-VARIABLE NEUTRINO SIGNAL

6.1 Motivation

A time-dependent archival search in the direction of the blazar TXS 0506+056 revealed [11] evidence of a neutrino flare. More recently, direct evidence of time-integrated neutrino emission from a nearby active galaxy NGC 1068 was found [2]. A natural follow-up question arises: Are neutrino sources time-variable? While it is difficult to answer that question directly and we expect there to be a mixture of steady and variable sources, IceCube has searched for a time-dependent signal as a way to reduce background. The reasoning is that a short burst of neutrinos from a particular point source would be statistically easier to identify as the steady[6] background observed by IceCube would be considerably reduced.

All prior studies of time-variability in IceCube assume a temporal profile for the neutrino signal [119, 11, 120, 104, 121, 105]. The temporal profile of an astrophysical neutrino signal is currently unknown. Time-variability of this neutrino emission from TXS 0506+056 has been studied extensively by assuming a temporal profile of the possible flare(s) or searching for temporal neutrino correlation with other electromagnetic counterparts. In the following sections, I will describe `TAUNTON` : a statistical test to determine if data is consistent with a steady neutrino source. The method can be quickly applied to candidate neutrino sources (hotspots) from time-integrated analyses. It should be noted that this is not a likelihood ratio test and the hypothesis being tested is a steady signal + background. It is a single hypothesis test and does not fit a parameter; only provides a p-value. This **steady hypothesis** is demonstrated in 6.1 for two simulated neutrino signals with identical strengths but

[6] Neutrino data collected by IceCube is known to have seasonal fluctuations but this discussion applies to much shorter time-windows ($\lesssim$ 1 day)

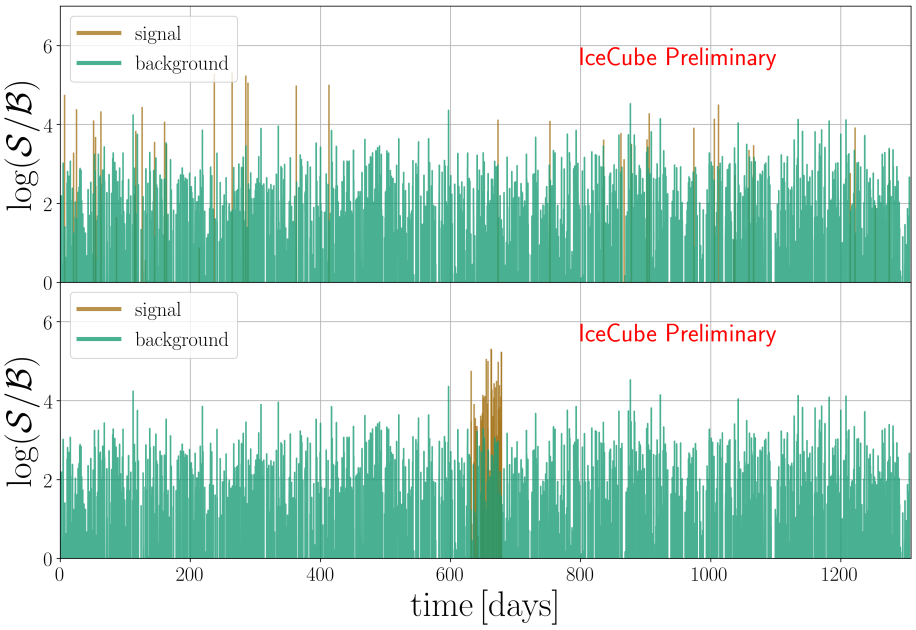

Figure 6.1: The log of spatial and energy signal probabilities over the background probabilities plotted for a selection of scrambled IceCube events. Simulated signal events are clustered (bottom) as opposed to injected uniformly (top) to demonstrate the difference in their time variability. I created this plot using the `matplotlib` package in `PYTHON`.

differing temporal profiles. The advantage of this method is that it can be quickly applied for future time-integrated searches while being sensitive to generic time variability.

Analyses in IceCube are performed by a variety of coding packages written and maintained by members of the collaboration. I developed, tested and then applied `TAUNTON` twice on different datasets with different packages in IceCube:

1. 7.5 year (2011-2018) Gamma-ray Follow Up (GFU) sample at the location of the top 4 hotspots from a previous time-integrated analysis [122], which are NGC 1068 , TXS 0506+056 , PKS 1420+240 and GB6 J1542+6129

2. 8.7 years (2011-2019) Northern Tracks (NT) sample with improved neutrino reconstruction and data calibration for a promising catalog of 51 potential neutrino sources

6.2 Method

TAUNTON uses high-level IceCube data which provides reconstructed information about events. Monte Carlo (MC) simulations provide identical information about injected events, as we saw in §5.8. For typical time-dependent point-source analyses in IceCube, this data is scrambled in right ascension (RA) and time to serve as "background" for trials. Additionally, MC simulations are time-independent and can be utilized to generate a variety of time-dependent and energy-dependent[7] signal events, by sampling appropriately. As we previously saw in §5.8, each event can be assigned a weight: $\log(\mathcal{S}/\mathcal{B})$. Additionally, each event has a time associated with it in units of Modified Julian Days (MJD), which can either be generated for signal and background events or utilized directly from the detector. These two quantities form the basis of the TAUNTON algorithm since $\log(\mathcal{S}/\mathcal{B})$ utilizes the spatial and energy probability of each event with respect to a point source. Note that, by construction, $\log(\mathcal{S}/\mathcal{B})$ is higher for events near the source position being searched due to the spatial term so TAUNTON uses spatial, energy, and temporal information from events to determine if data is consistent with steady signal and background.

The method relies on using a single sample Cramér–von Mises (CVM) test [123] to compute a test statistic[8], TS, in the following way:

$$TS = \sqrt{N_{\rm ev}(n_{\rm fit}) \int_0^1 \left[F_n(\Delta t) - F(\Delta t)\right]^2 \, dF(\Delta t)} \tag{6.1}$$

Here, Δt, is the time difference between consecutive events. $F(\Delta t)$ and $F_n(\Delta t)$ are the empirical distribution function (EDF) and the sample being tested. The EDF is calculated using the steady hypothesis. Additionally, $N_{\rm ev}(n_{\rm fit})$ are the largest $\log(\mathcal{S}/\mathcal{B})$ number of events as a function of the number of signal events from the time-integrated point-source fit at the source location.

[7] This method assumes a power-law flux but can be generalized to additional flux models

[8] This is a different test-statistic than the one derived for point-source analyses in §5.8

6.2.1 $N_{\rm ev}$ selection

$N_{\rm ev}$ is the number of events in the sample being tested and primarily depends on $n_{\rm fit}$, the number of fitted signal events from the time-integrated point-source fit at the source location. Additionally, we know that $n_{\rm fit}$ depends on the range of injected signal events, $n_{\rm inj}$, of identical spectral indices. That is, neutrino signal events drawn from MC for exactly $n_{\rm inj}$ number of signal events and index of $\gamma_{\rm inj}$, yield a distribution of $n_{\rm fit}$. This distribution is wider for weaker signal (low $n_{\rm inj}$) and narrower for stronger signal (high $n_{\rm inj}$) and is demonstrated for the two data samples and packages in Fig. 6.2 and 6.3.

If there is a bias in the fitting, on average many $n_{\rm inj}$ might match $n_{\rm fit}$. In order to test the choice of $N_{\rm ev}$, I consider the following choices:

(a) $N_{\rm ev}$ = $n_{\rm fit}$

(b) $N_{\rm ev}$ is pulled from the $n_{\rm inj}$ distribution for the target $n_{\rm fit}$

(c) $N_{\rm ev}$ = median $n_{\rm inj}$ for the target $n_{\rm fit}$

(d) $N_{\rm ev}$ = mean $n_{\rm inj}$ for the target $n_{\rm fit}$

The disadvantage of choice (b) is that it would potentially yield a different $N_{\rm ev}$ and therefore different TS from 6.1, but was tested nonetheless. Note that the Northern Tracks sample has a much lower bias compared to the GFU sample. This is primarily because of the improved reconstruction and calibration for the Northern Tracks sample, as well as the usage of kernel density estimation (KDE) from MC for the spatial PDFs as described in 5.7.3. For the GFU sample, the spatial pdf was approximated by a spectral index independent bivariate Gaussian, with the estimated angular event of each event providing the standard deviation. The KDE treatment is particularly helpful for lower energy events, $E_\mu \lesssim 10$ TeV, and therefore helps in reducing inj-vs-fit bias for softer index as can be seen in Fig. 6.2b. Due to lower inj-vs-fit bias for the Northern Tracks sample, the above-mentioned tests were only performed for the GFU sample. As demonstrated later in this

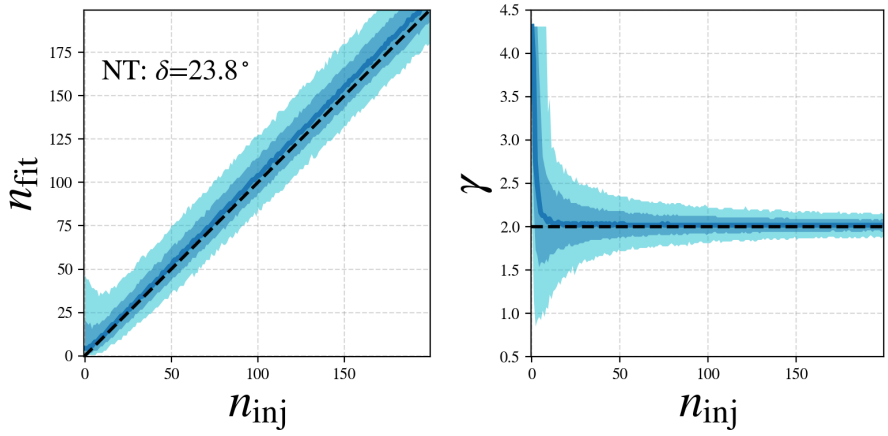

(a) Northern Tracks sample: $\gamma_{\mathrm{inj}} = 2$

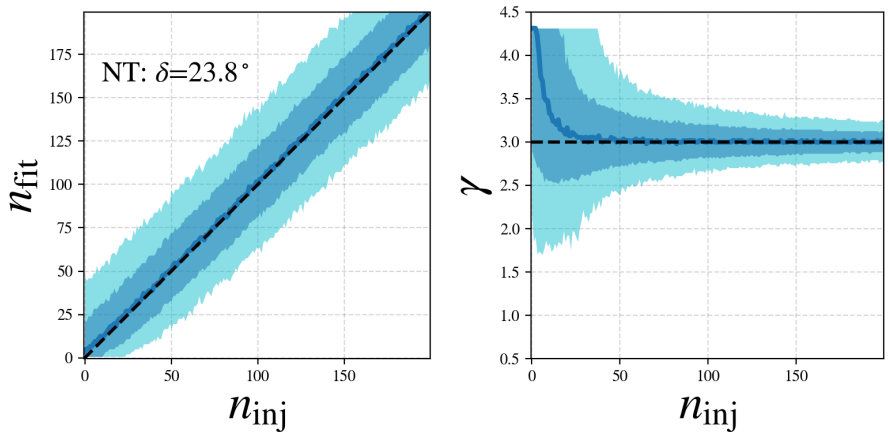

(b) Northern Tracks sample: $\gamma_{\mathrm{inj}} = 3$

Figure 6.2: n_{fit} distributions for time-integrated point-source fits at $\delta = 23.8°$ using the Northern Tracks data sample and IceCube point-source search package, `skyLLH`. The shaded regions represent the 1 σ and 2 σ central deviations from the median, which are plotted as the dark solid line. The dashed lines represent the expectation that one fully recovers the injected signal. I created this plot using the `matplotlib` package in `PYTHON`.

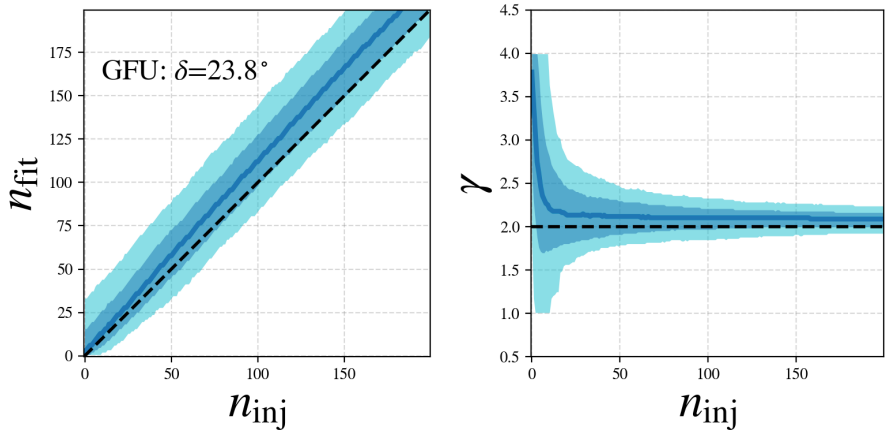

(a) GFU sample: $\gamma_{\mathrm{inj}} = 2$

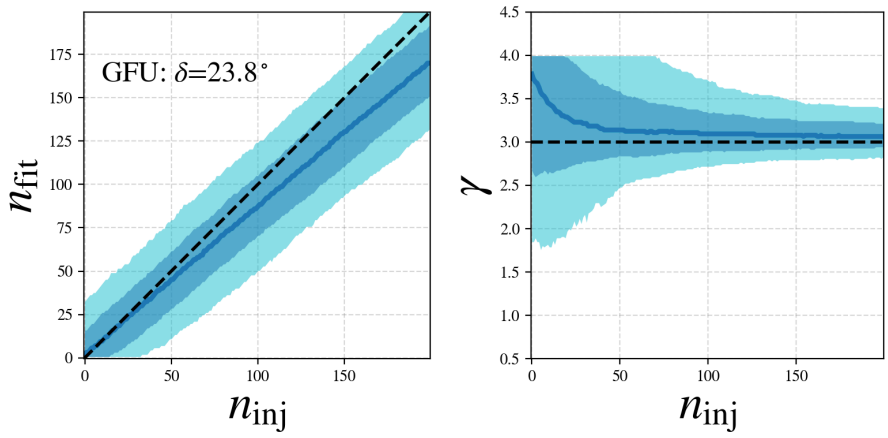

(b) GFU sample: $\gamma_{\mathrm{inj}} = 3$

Figure 6.3: n_{fit} distributions for time-integrated point-source fits at $\delta = 23.8°$ using the GFU data sample and IceCube point-source search package, `skylab`. The shaded regions represent the 1 σ and 2 σ central deviations from the median, which are plotted as the dark solid line. The dashed lines represent the expectation that one fully recovers the injected signal, similar to 6.2. I created this plot using the `matplotlib` package in `PYTHON`.

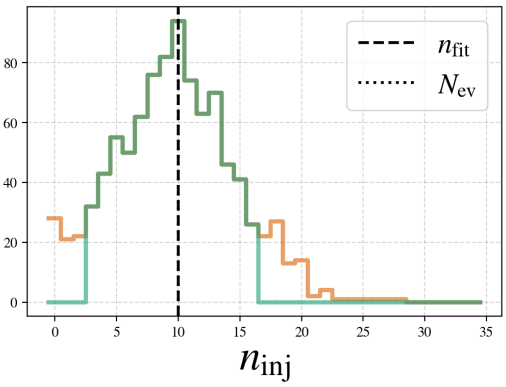

(a) Northern Tracks sample: $\gamma_{\text{inj}} = 2$

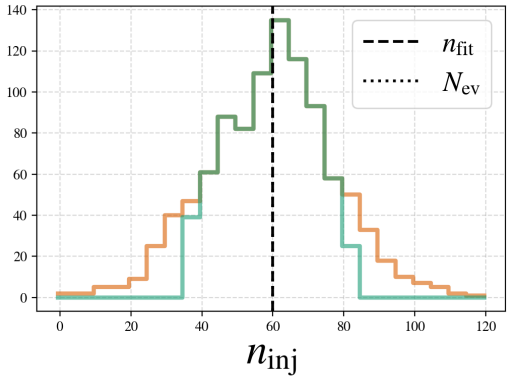

(b) Northern Tracks sample: $\gamma_{\text{inj}} = 3$

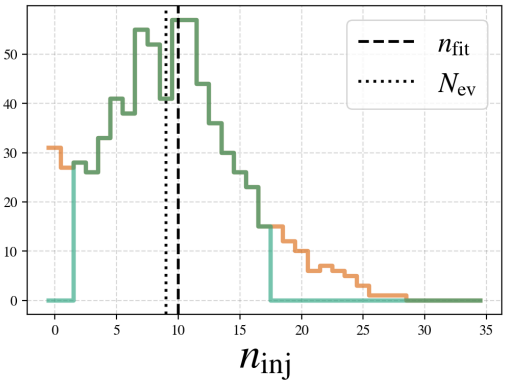

(c) GFU sample: $\gamma_{\text{inj}} = 2$

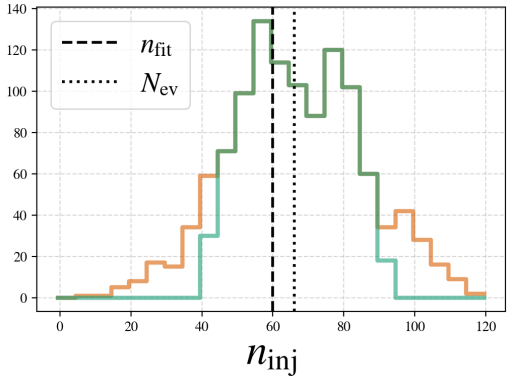

(d) GFU sample: $\gamma_{\text{inj}} = 3$

Figure 6.4: Extraction of N_{ev} from pre-computed inj-v-fit distributions such as the one shown in Fig. 6.2 and 6.3. This is a slice that satisfies $n_{\text{fit}} - 0.5 < n_{\text{inj}} < n_{\text{fit}} + 0.5$ at $\delta = -0.01°$ using different IceCube packages and data samples. n_{fit} is shown for reference as a dashed line, while the extracted N_{ev} according to choice (c) is shown as a dotted line. The central 80% is used for N_{ev} test choices (b) and (d) to cut the tails and is demonstrated by the green distribution. I created this plot using the `matplotlib` package in `PYTHON`.

chapter, choice (c) performs at least as well as the other choices, if not better, and has the advantage of providing a single, repeatable TS value from a fit.

After performing a fit at the source location and obtaining n_{fit}, `TAUNTON` uses the declination and index dependent distributions shown in Fig. 6.4. `TAUNTON` takes a slice of the aforementioned distribution that satisfies: $n_{\text{fit}} - 0.5 < n_{\text{inj}} < n_{\text{fit}} + 0.5$. For choice (c) of N_{ev} selection, the median n_{inj} is assigned to N_{ev} . This is demonstrated in Fig. 6.4. For test choices of (b) and (d), the central 80% is utilized to ensure the random pull or mean is not affected by the tails respectively. Additionally, as the Northern Tracks sample has a

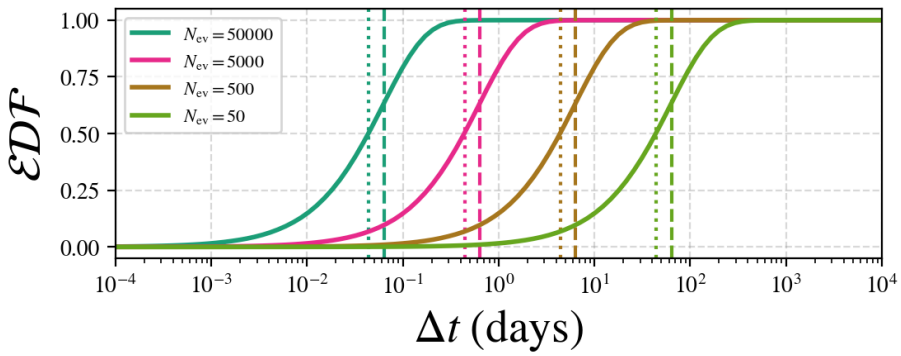

Figure 6.5: Empirical distribution functions for steady N_{ev} events in the 8.7 year Northern Tracks sample. This is calculated by a toy Monte Carlo described in the text and considers the seasonal variation of detector data. The vertical dashed lines are the mean separation between events, livetime / N_{ev} , while the dotted lines are the median, with the colors representing sample N_{ev} . I created this plot using the `matplotlib` package in `PYTHON`.

minimal bias in n_{fit}, N_{ev} is usually the same as the fitted signal events while it accounts for an under- or over-fit for the GFU sample. Finally, N_{ev} is rounded to a positive integer and used in conjunction with $\log(\mathcal{S}/\mathcal{B})$ weights of each event to extract the sample of events for `TAUNTON` . Overestimating N_{ev} can include more "true" background events in the sample while underestimating N_{ev} means missing out on "true" signal events and obtaining the right balance is important.

6.2.2 Empirical Distribution Functions

The steady hypothesis tested by `TAUNTON` is described by a steady signal and background. The empirical distribution function (EDF), prescribed as $F(\Delta t)$ in Eq. 6.1, is generated from toy Monte Carlo simulations of equal-weight event times. This EDF depends on N_{ev} and the livetime of the detector, assuming 100% uptime. For N_{ev} event times uniformly sampled in a duration, livetime, the cumulative distribution function of the consecutive event time differences provides the EDF. While IceCube has an impressive uptime above 99.8%, tiny gaps between runs do exist. Additionally, seasonal variation is a known effect so the generation of EDF must follow this variation as well since the EDF must take the detector performance and data properties into account.

Assuming a 100% uptime for the detector, we can gain insight into the properties of the EDF. Consider that n-events are detected uniformly, $t \in [0, 1]$ of arbitrary time units. It can be shown that the cumulative distribution function (CDF) of the consecutive time difference, $x = \Delta t$, can be written as: $Y_X(x) = P(X \leq x) = 1-(1-x)^{n-1}$. Consequently, the probability distribution function is $f(x) = (n-1)(1-x)^{n-2}$. The expectation value or mean of the consecutive time difference can then be shown to be $1/n$ as follows:

$$< x >= \int_0^1 x f(x)\, dx = \int_0^1 x(n-1)(1-x)^{n-2}\, dx \tag{6.2}$$

Using integration by parts for $u = x,\ v = -(1-x)^{n-1}$, we get:

$$< x > = -x(1-x)^{n-1}\Big|_0^1 + \int_0^1 (1-x)^{n-1} dx \tag{6.3}$$

$$< x > = 0 - \frac{(1-x)^n}{n}\Big|_0^1 = \frac{1}{n} \tag{6.4}$$

This argument can be generalized to a detector with livetime via a simple unit conversion and gives us the advertised $< \Delta t >= \text{livetime} \ / \ N_{\text{ev}}$ in Fig. 6.5. The median can be calculated directly from the aforementioned CDF by solving for x such that $Y_X(x) = 0.5$, which yields $\text{med}(x) \rightarrow 0.69 < x >$. Note that this calculation is strictly for an ideal (100%) detector with a perfectly steady event rate. The curves in Fig. 6.5 are generated by sampling event time from observation runs of detector data, appropriately weighted per run according to the seasons so that the resulting distribution includes seasonal variation and the non-100% detector uptime. This is why the curves in Fig. 6.5 only depend on N_{ev} as the livetime is already fixed for the particular data sample, and can be slid to the left or right depending on N_{ev} as the shape contains the important detector information. These curves provide the empirical distribution functions for the steady hypothesis

and specify, on average, how frequently event pairs should be at lower Δt's as opposed to higher Δt's if $N_{\rm ev}$ follows steady arrival time. Additionally, these curves are generated by sampling $\sim 10^7$ event times from observation runs of detector data, adjusted for the specific $N_{\rm ev}$, and then interpolated using `scipy.interpolate` routine [116]. Interpolation is required because the steady hypothesis, $F(\Delta t)$, has to be evaluated at the Δt's for the specific sample for test statistic calculation, as per Eq. 6.1. In the extremely unlikely event that the sample Δt lies outside the range of the toy Monte Carlo, the interpolation is set to fill a value of $[0, 1]$ for lower and higher Δt's respectively since we know the EDF should asymptote to those values.

6.2.3 Test Statistic Calculation

Once $N_{\rm ev}$ is extracted after performing a time-integrated search at the source location, `TAUNTON` calculates the EDF, $F(\Delta t)$, as described in the previous section. In order to construct the sample CDF, $F_n(\Delta t)$, for Eq. 6.1, `TAUNTON` assigns each consecutive event pair a weight as the geometric mean of each event's $\log(\mathcal{S}/\mathcal{B})$. For instance, if the event times in increasing order are $t_1,\ t_2, \ldots t_{Nev}$, then there exist $N_{\rm ev}$ - 1 consecutive event pairs: $\Delta t_{i,i+1}$ for $1 \leq i \leq N_{\rm ev} - 1$ with each pair assigned a weight, $w = \sqrt{\log \mathcal{S}/\mathcal{B}_i \times \log \mathcal{S}/\mathcal{B}_{i+1}}$. An example is demonstrated for $N_{\rm ev} = 6$ events in Fig. 6.6. The sample CDF, $F_n(\Delta t)$, and the empirical distribution function, $F(\Delta t)$, are then used to calculate the test statistic as per Eq. 6.1. Fig. 6.7 demonstrates this for a realization of the Northern Tracks sample. Note that Eq. 6.1 does not integrate in Δt, so the separation between the sample Δt's does not matter. Only the distance between the sample CDF and the corresponding EDF at the same Δt matters, as does $N_{\rm ev}$. The integration is performed in $F(\Delta t)$ space according to a composite trapezoidal rule using the `numpy.trapz` routine [124].

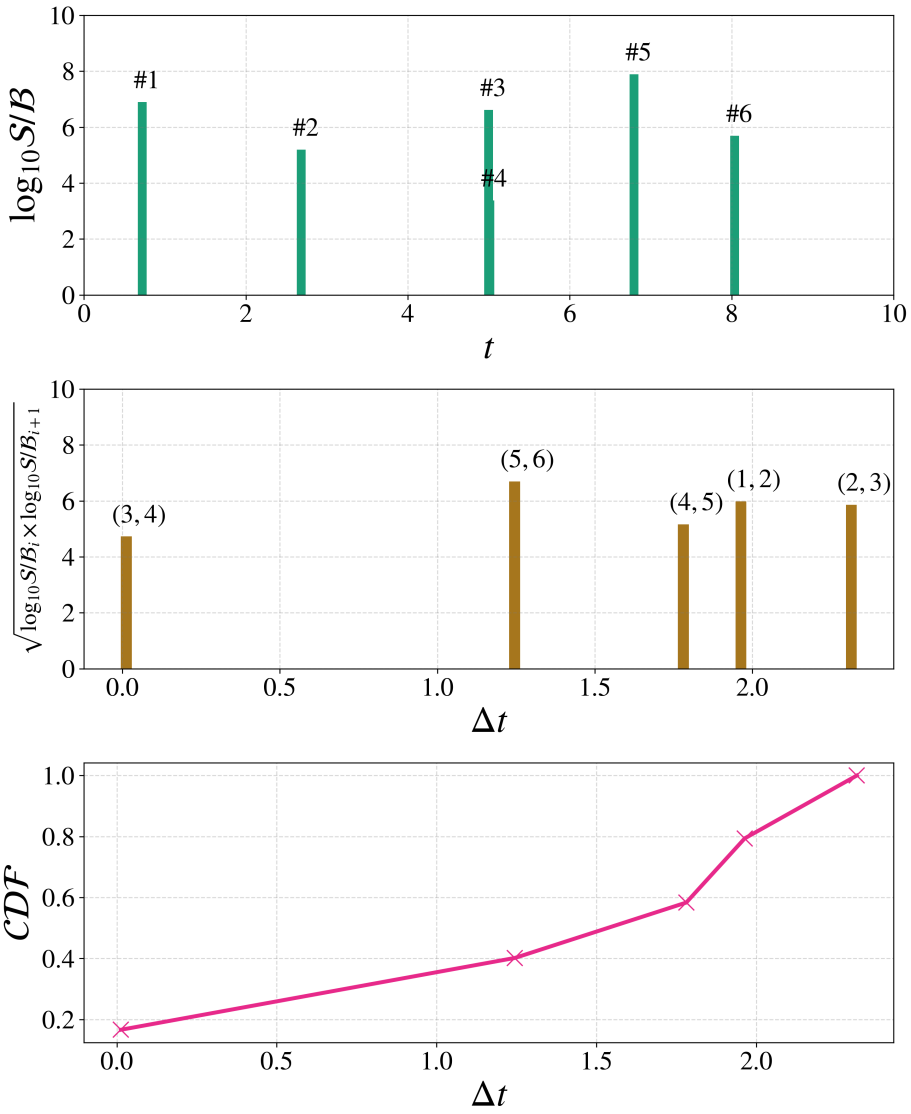

Figure 6.6: Example calculation of a sample CDF, $F(\Delta t)$, for $N_{\text{ev}} = 6$ events in arbitrary units of time. The topmost panel demonstrates a realization of 6 events sampled from a uniform distribution in $[0, 10]$ time units. The closest events $i = 3, 4$ form the lowest Δt pair in panel 2, with $i = 1, 2$ pair being the largest separated in middle and bottom panels. The bottom panel is calculated from the middle panel by normalizing the weights, as the largest weighted pair of events, $i = 1, 2$, provide the largest deviation to this cumulative sum. I created this plot using the `matplotlib` package in `PYTHON`.

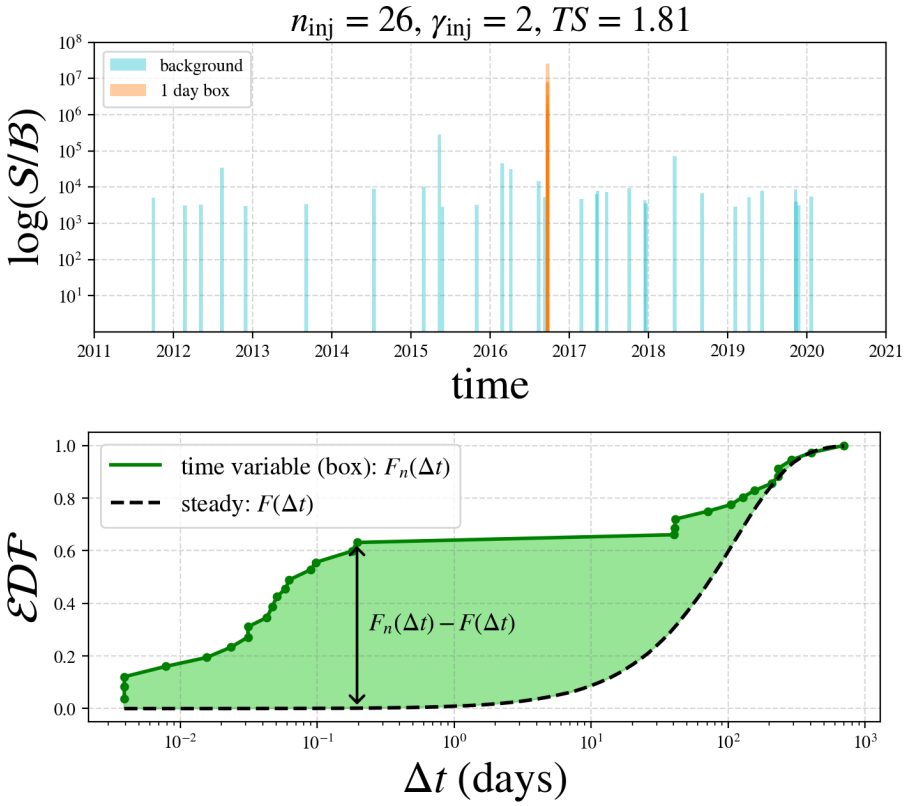

Figure 6.7: Example calculation of TAUNTON test statistic by injecting a box-flare to a realization of the 8.7-year Northern Tracks sample. The injected signal parameters are a 1-day box-flare of $n_{=}26$ events with a spectral index of $\gamma_{\rm inj} = 2$ at declination $\delta = 5.69°$, which yield time-integrated fit parameters of $n_{\rm fit} = 33.1$, $\gamma_{\rm fit} = 1.9$. The largest $N_{\rm ev} = 31$ events extracted by TAUNTON form the sample of events shown in the bottom panel and constitute the sample CDF, $F_n(\Delta t)$ and measured against the steady hypothesis, $F(\Delta t)$ as per Eq. 6.1 to yield a TAUNTON test statistic of 1.81. Additional largest $\log(\mathcal{S}/\mathcal{B})$ events are shown in the top panel for visualization purposes and TAUNTON 's sample of $N_{\rm ev}$ =31 events in the bottom panel only includes 5 background events. I created this plot using the `matplotlib` package in PYTHON.

6.2.4 Steady TS distributions

TAUNTON calculates the time-variability test statistic (TS) for each realization or trial, which includes performing a time-integrated point-source fit at the source location of interest for that specific realization. As per §5.8, we continue using the "signal" and "background" terminology here, where signal events are injected from MC and background events are scrambled detector data. The time-integrated fit is performed at the source location on the combined (signal and background) sample of events. In order to evaluate this TS for any realization or detector data, TAUNTON computes the steady TS distribution for identical signal parameters, at the declination δ of the injection, the Poisson mean number of signal events $n_{\rm inj}$, and spectral index γ of the signal power-law flux.

TAUNTON uses a large number of trials to attain a steady TS distribution, typically in the range $5 \times 10^4 - 10^5$, as shown in Fig. 6.8. The only restriction to performing additional trials is computational time, and the aforementioned range is adequate to reject the steady hypothesis with at most $\sim 4.2\sigma$ significance. Additionally, since $N_{\rm ev}$ is an important factor in calculating TS (Eq. 6.1), the distributions get slightly narrower for higher $N_{\rm ev}$ or $n_{\rm inj}$. This is because the mean of the consecutive time difference for n events in time $t \in [0, 1]$ is $< x >$: $1/n$, while the variance is $\mathrm{var}(x) : 2/(n^2 + n) - 1/n^2$. This variance in $x = \Delta t$ is higher for lower n, and therefore changes the TS distributions slightly. Additionally, the distributions shift slightly depending on the spectral index of the injected signal because a harder index means injecting more high-energy events as compared to a softer index. This directly affects $\log(\mathcal{S}/\mathcal{B})$ and makes the TS values a bit larger. For instance, see in Fig. 6.8 that a larger fraction of trials yields a high TS of 1 for the harder index of $\gamma = 2$ as compared to $\gamma = 3$, even though a fewer number of signal events are injected.

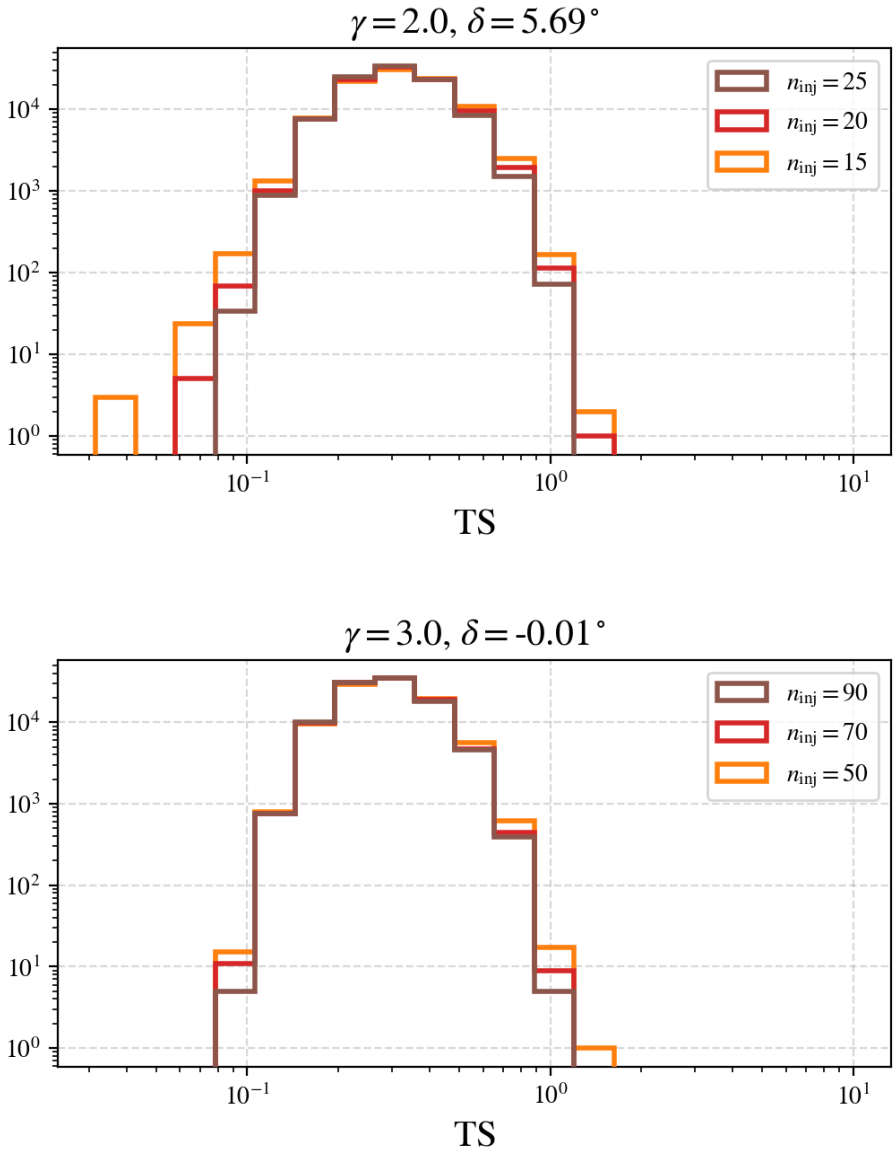

Figure 6.8: Steady TAUNTON TS distributions for the 8.7-year Northern Tracks sample using 100,000 steady signal injection trials. The top panel displays this distribution for 3 sample injections with a common spectral index of $\gamma = 2$ at declination $\delta = 5.69°$, and the bottom panel for a softer spectral index of $\gamma = 3$ at declination $\delta = -0.01°$. Note that the histograms utilize a log-log scaling. I created this plot using the `matplotlib` package in PYTHON.

6.3 Performance Benchmarking

Since TAUNTON is a single-hypothesis time-variability test, all TAUNTON performance benchmarking tests are performed for fixed signal parameters $(n_{\rm inj},\ \gamma_{\rm inj},\ \delta)$. For each test, trials are categorized as "steady" and "time-variable" depending on the temporal profile of the injected signal. Note that the time-variable injections serve to benchmark the performance of the method, and are not part of the method. The time-variable injections are then compared to the steady injections. TAUNTON calculates and utilizes the relevant steady TS distribution described in the previous section §6.2.3.

A box or top-hat time PDF for time-variable signal events is perhaps the simplest form of time-variability; wherein signal events only arrive within a time window and do not arrive outside the bounds set by the box. For such a box, there are two temporal parameters, T_0 and Δt, such that the former specifies the central time of the box and the latter is the width of the box. This simple case is extensively tested by TAUNTON to establish and optimize performance. This single flare test case is then modified to include additional features such as double flares, multiple flares, and semi-flares. For instance, the performance of two 10-day flares of 5 signal events each can be compared to a 20-day 10 signal event flare to evaluate how TAUNTON 's performance changes when a flare *splits*. In this section, I shall first describe the test to optimize TAUNTON and select a choice for calculating $N_{\rm ev}$ (see §6.2.1 for $N_{\rm ev}$ selection choices). Next, I shall describe tests designed to establish TAUNTON 's performance for a variety of time-dependent signal.

6.3.1 $N_{\rm ev}$ selection

This test is designed to evaluate TAUNTON 's ability to reject the steady hypothesis for a box-shaped or top-hat signal time PDF (flaring signal), for the $N_{\rm ev}$ selection choices as described in §6.2.1. As described previously, this test is important when the $n_{\rm fit}$ bias for the injected signal is high and directly impacts $N_{\rm ev}$, as is the case for the GFU dataset

(see Fig. 6.3). This involves calculating the steady TS distributions for each of the four $N_{\rm ev}$ selection choices and a sample signal with a hard ($\gamma = 2$) and soft ($\gamma = 3$) index at test declinations. For a fixed test declination, injection strength ($n_{\rm inj}$), injected spectral index ($n_{\rm inj}$), TAUNTON 's sensitivity to a box-shaped signal time PDF decreases as the time window of the box, Δt, increases. Note that this Δt is the size of the injected signal flare and is not related to the consecutive time difference of events utilized by TAUNTON 's algorithm.

For a specific time window Δt of the box-flare, TAUNTON computes a distribution of time-variable TS from different trials of identical signal parameters. The median of this distribution, $\mathrm{med}(TS_{\rm var})$, is then converted to a p-value or significance using the corresponding steady TS distribution as explained in Fig. 6.10. For shorter flares, TAUNTON is able to reject the steady hypothesis with a higher significance since events are clustered together in time due to a narrow, box time PDF as opposed to uniformly distributed throughout the detector livetime. Consequently, TAUNTON 's performance suffers as the time window of the injected box-flare increases as shown in Fig. 6.9. See that all four choices of $N_{\rm ev}$ selection perform similarly, but choice (c) of calculating $N_{\rm ev} = \mathrm{med}(n_{\rm inj})$ for the given fit parameters performs better. After evaluating this test at other declinations and injected signal parameters, I decided to use this choice for selecting $N_{\rm ev}$ in TAUNTON . All tests hereafter and results of applying TAUNTON on data use this choice of $N_{\rm ev}$ selection.

6.3.2 Double box-flares

Splitting a box flare into two could lower the performance of this method since it relies on how the consecutive event pair Δt's are distributed. In order to see this effect, I compare a single v/s double box-flare, such that the total flare size and flare strength remain the same. The double box-flares are injected such that they are separated maximally to be conservative i.e. near the beginning and end of the livetime. For instance, 50 signal events in a 10-day flare are compared directly to 25 signal events in two 5-day flares each. The

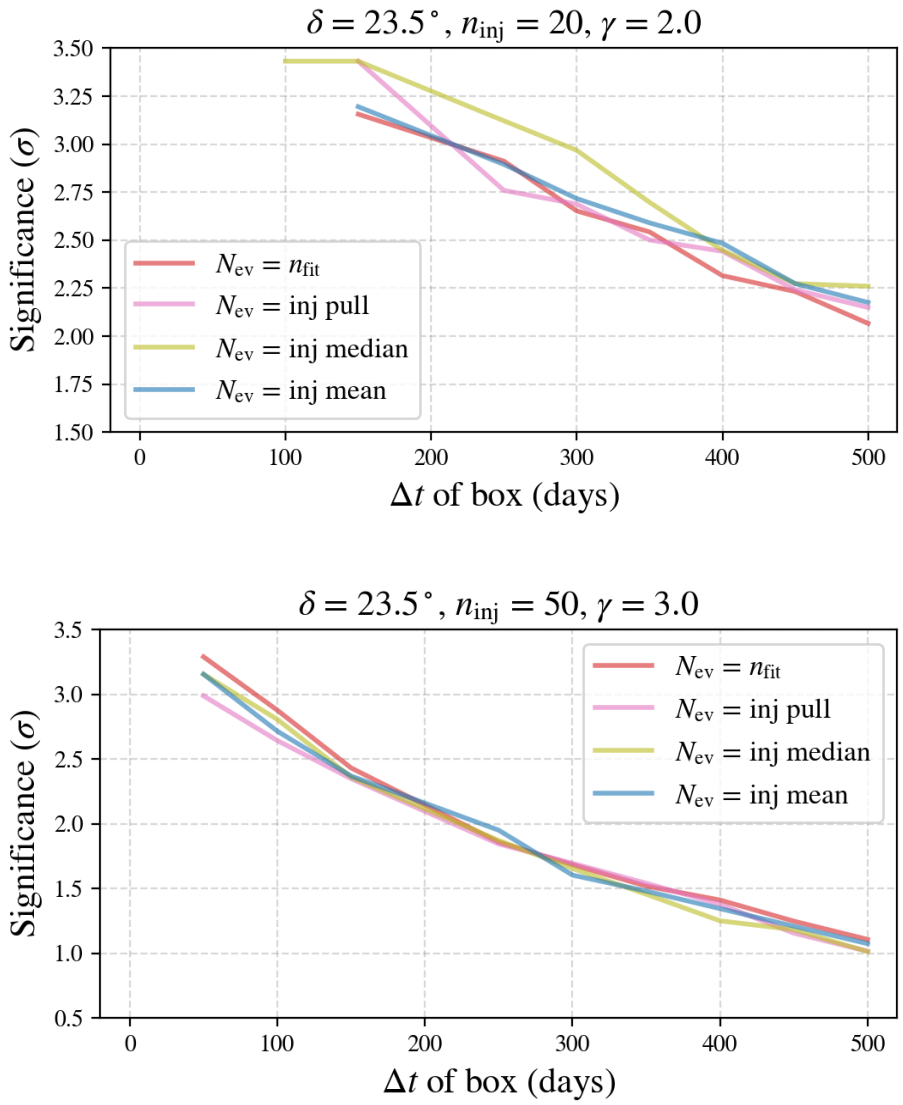

Figure 6.9: TAUNTON 's performance of increasingly long box-flare shaped signal time PDFs, evaluated for four N_{ev} selection choices at a test declination of $\delta = 23.5^\circ$ on trials drawn from the 7.2-year GFU sample. TAUNTON 's ability to reject the steady hypothesis, or statistical power, diminishes for longer injected box flares naturally since the largest possible box is the steady hypothesis. The top panel demonstrates the impact of N_{ev} on the statistical power of TAUNTON for injection parameters of $n_{\text{inj}} = 20$ events with a hard index ($\gamma = 2$) and the bottom panel for $n_{\text{inj}} = 50$ events with a soft index ($\gamma = 3$). The four choices for N_{ev} extraction are explained in the text. I created this plot using the `matplotlib` package in PYTHON.

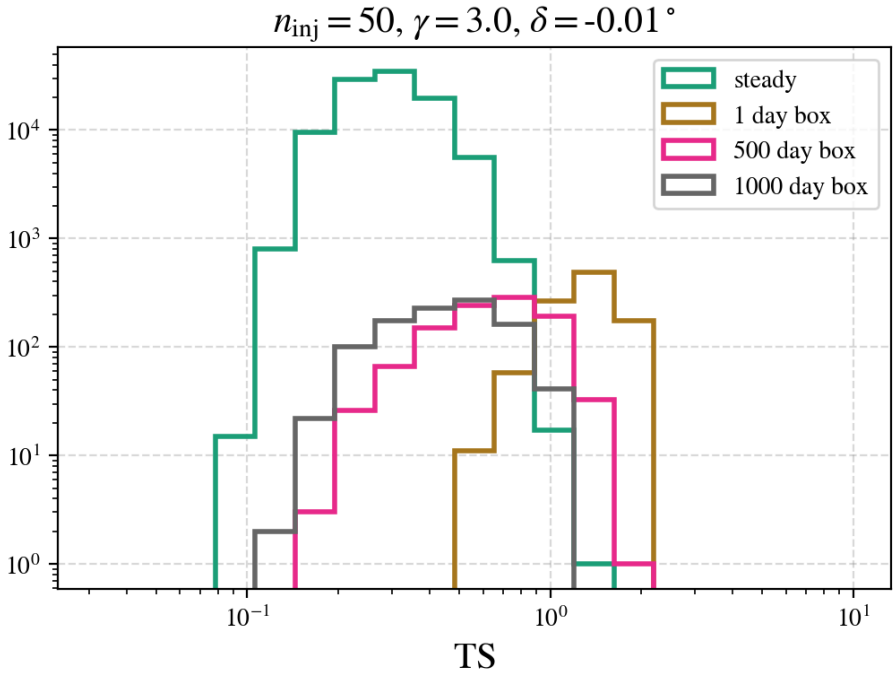

Figure 6.10: Example TAUNTON TS distributions for the steady hypothesis and box-flares for identical injected signal parameters: $n_{\mathrm{inj}} = 60,\ \gamma_{\mathrm{inj}} = 3$. These distributions use trials drawn from the 8.7-year Northern Tracks sample at declination $\delta = -0.01$. The median of the box-flare TS is converted to a p-value to reject the steady hypothesis. As can be seen, TAUNTON is more sensitive to shorter box flares. I created this plot using the `matplotlib` package in PYTHON.

proximity of the two flares within the detector livetime has important consequences to the TAUNTON test statistic as it relies on consecutive event time differences. This type of signal events distribution should perform the worst when the two flares are separated by the maximum amount possible in the detector livetime, hence this type of flare-splitting is tested here. The solid and dashed curves in Fig. 6.11 represent the single and double box significance for the 7.2-year GFU sample.

The important signal parameters relevant for TAUNTON 's performance are as follows. Firstly, the amount of injected signal events $n_{\rm inj}$ increases TAUNTON 's ability to reject the steady hypothesis as a stronger time-integrated point source helps TAUNTON determine statistically if the fluctuation in consecutive event time difference is important. Secondly, the signal time PDF for longer box flares asymptotes toward the steady hypothesis, and TAUNTON has increased sensitivity to shorter flares. Finally, for identical total injected signal strength $n_{\rm inj}$ and total flare duration, splitting a signal flare into two worsens TAUNTON 's sensitivity as expected. These trends are also seen for the 8.7-year Northern Tracks sample with improved reconstruction and calibration as seen in Figures 6.12, 6.13.

6.3.3 Multi box-flares

As we learned from the double box-flare test, there are two directions via which a single box-shaped flare of signal events asymptotes toward the steady hypothesis: (i) increasing the time-window of a single flare and (ii) splitting the single flare into multiple flares. For a total $N_{\rm ev}$ events in a signal flare, splitting this flare into multiple flares decreases TAUNTON 's performance because those signal events can be separated further apart depending on the proximity of those multiple flares. Therefore, we can naturally extend the previous test to multiple box-flares, such that they are injected randomly and evenly throughout the livetime. This multi-box-flares test is a limiting check to see if the significance drops as the number of flares approaches $N_{\rm ev}$ or $n_{\rm inj}$. For this test, the centers of all box flares are randomized throughout the livetime such that there are no overlapping flares.

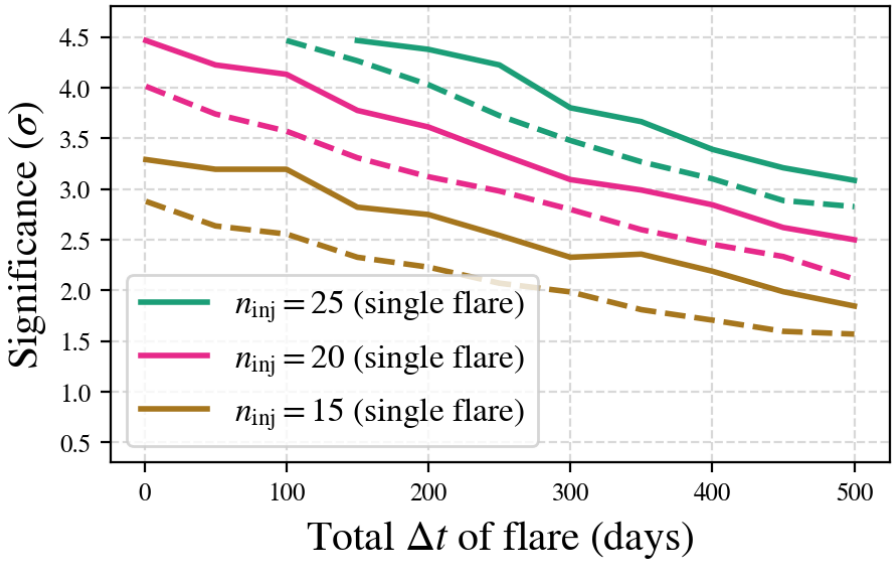

(a) $\delta = 5.69°, \gamma = 2$

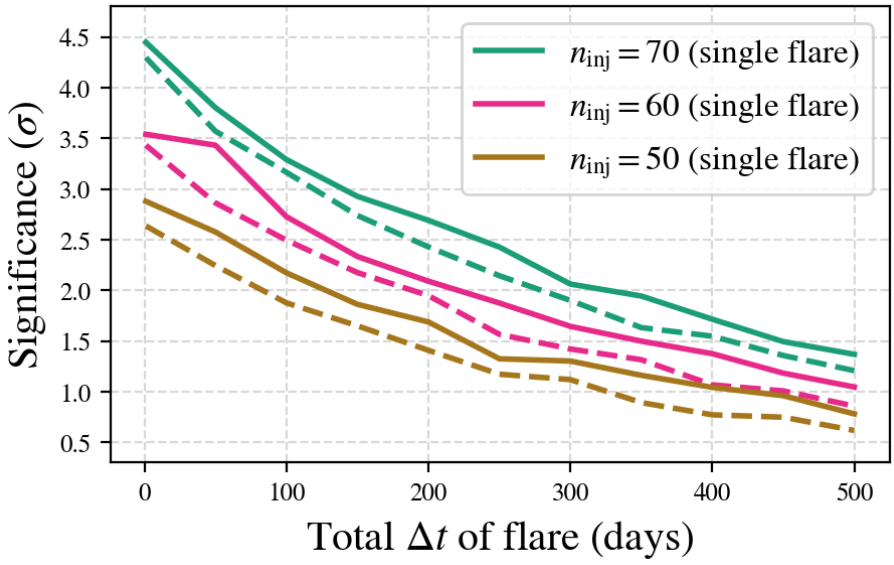

(b) $\delta = -0.01°, \gamma = 3.25$

Figure 6.11: TAUNTON 's performance for increasingly long single and double box-flare shaped signal time PDFs, evaluated for 3 injection strengths (n_{inj}) at test declinations of $\delta = -0.01°$ (top) and $\delta = 5.69°$ (bottom) on trials drawn from the 7.2-year GFU sample. The solid and dashed lines correspond to a single and double box flare respectively. I created this plot using the `matplotlib` package in PYTHON.

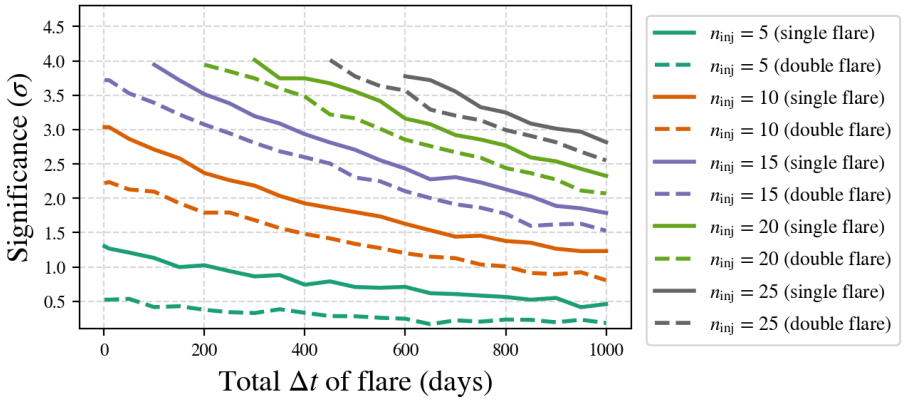

(a) $\delta = 5.69°$, $\gamma_{\text{inj}} = 2$

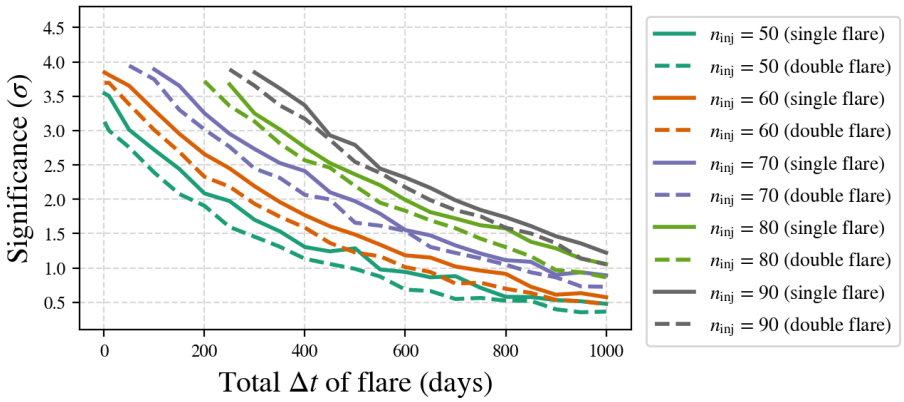

(b) $\delta = 23.8$, $\gamma_{\text{inj}} = 3$

Figure 6.12: `TAUNTON` 's performance for increasingly long single and double box-flare shaped signal time PDFs, evaluated for various injection strengths (n_{inj}) and spectral indices at test declinations of $\delta = 5.69°$ (top) and $\delta = 23.8°$ (bottom) on trials drawn from the 8.7-year Northern Tracks sample. The solid and dashed lines correspond to a single and double box flare respectively, similar to Fig. 6.11. I created this plot using the `matplotlib` package in `PYTHON`.

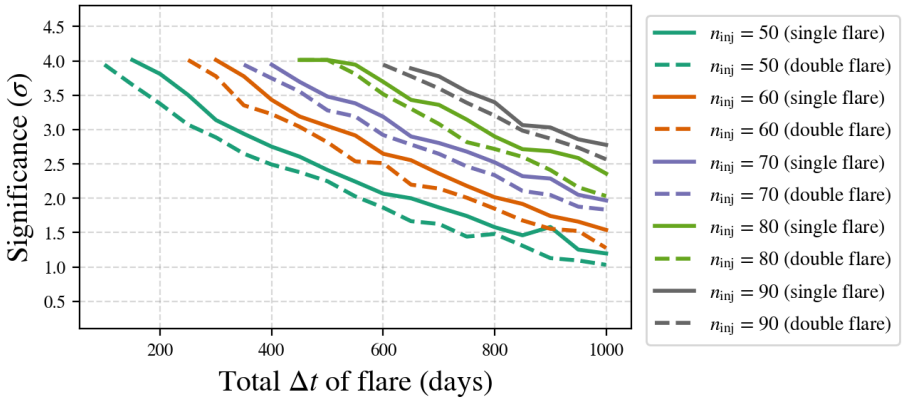

(a) $\delta = -0.01,\ \gamma_{\text{inj}} = 3$

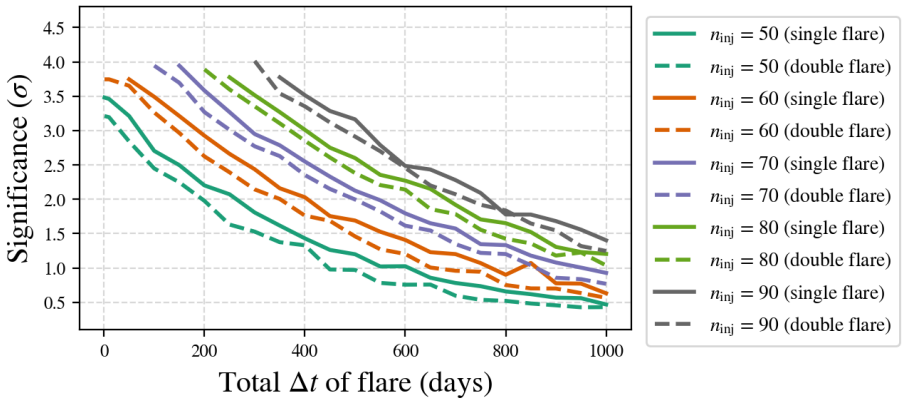

(b) $\delta = -0.01, \gamma_{\text{inj}} = 3.5$

Figure 6.13: Companion plot to 6.12: TAUNTON 's performance for increasingly long single and double box-flare shaped signal time PDFs, evaluated for various injection strengths (n_{inj}) and spectral indices at test declination of $\delta = -0.01°$ that coincides with the declination of NGC 1068 . The injected spectral index is $\gamma = 3$ (top) and $\gamma = 3.5°$ (bottom) on trials drawn from the 8.7-year Northern Tracks sample. The solid and dashed lines correspond to a single and double box flare respectively. I created this plot using the `matplotlib` package in PYTHON.

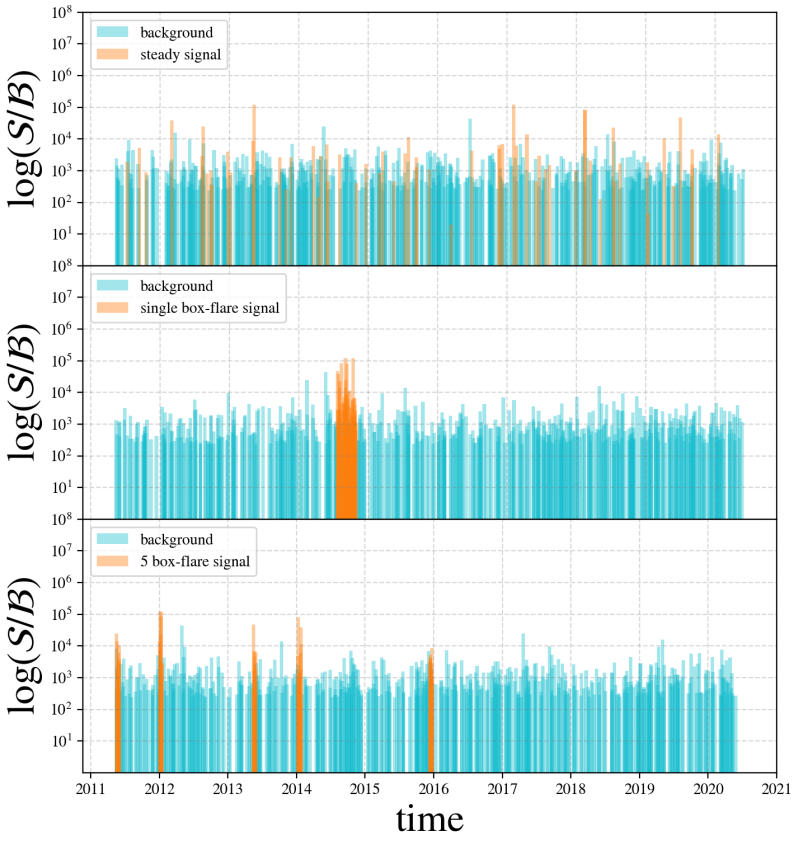

Figure 6.14: Example injections of varying signal time PDFs for a trial drawn from the 8.7-year Northern Tracks sample for declination $\delta = -0.01°$. The topmost panel demonstrates the steady hypothesis for injected signal and scrambled background data, while the middle panel for a single flare, and the bottom panel for multi flares with $N_{\text{flare}} = 5$. Each realization retains the total amount of injected signal of $n_{\text{inj}} = 60$ events at a softer spectral index of $\gamma = 3$. The middle and bottom panels have a total flare active time of 100 days. I created this plot using the `matplotlib` package in `PYTHON`.

The number of signal events per flare is distributed as evenly as possible. Another way to think about it is that as $N_{\text{flare}} \rightarrow N_{\text{ev}}$, the significance should drop to 0 since the time PDF mimics a steady signal. This is demonstrated in Fig. 6.14. See that while N_{flare} ¡¡ N_{ev} or n_{inj}, the multiple flares are distinct and recognizable, whereas the steady hypothesis can be thought of as the scenario where $N_{\text{flare}} = N_{\text{ev}}$.

In order to evaluate the performance of `TAUNTON` for multi-box-flares on trials drawn from the 8.7-year Northern Tracks sample, I test `TAUNTON` at the declination of NGC 1068 since there is evidence of time-integrated neutrino emission from that particular AGN [2]. This

test was performed for a soft[9] spectral index of $\gamma = 3$ and total mean injected strength of $n_{\rm inj} \in [50, 90] \times N_{\rm flare} \in [1, 30]$. For each combination in this grid, TAUNTON is evaluated for distributions of multi-box-flares with mean flare-sizes of $1,\ 5,\ 10,\ 50$ days and its performance is shown in Figures 6.15 and 6.16. Since IceCube needs 62.7 signal events for a power-law flux with a spectral index of $\gamma = 3$ at the declination of NGC 1068 to claim a neutrino source and reject the background-only hypothesis with a power of 5σ (pre-trial), the region in Figures 6.15, 6.16 to the left of the dashed vertical lines represent the added sensitivity of TAUNTON . See that as the size of the individual flares increases, TAUNTON 's sensitivity to time-variability decreases. Additionally, for very high $N_{\rm flare}$ of $20 - 30$, TAUNTON needs a strong time-integrated signal (high $n_{\rm inj}$) to reject the steady hypothesis and claim evidence for time-variability.

6.3.4 Semi-variable box-flare

While the simplest possible model of time-variability could be argued to be a box flare, here I test injections of box flares such that a fraction of the total injected signal mimics a steady distribution. In this test, the signal parameter of interest is the semi-variable fraction. This fraction of injected events follows a steady signal, whereas the rest retain a box-flare shape. For instance, say a specific realization or trial has $n_{\rm inj} = 60$ injected number of events for a flare-size of $\Delta t_{\rm flare} = 100$ days then for a semi-variable fraction of 0.3, only 42 of the 60 injected events will be in the 100-day box-flare. The remaining 18 events will be injected uniformly throughout the detector livetime. This semi-variable fraction provides another testing parameter for time variability, as a semi-variable fraction of 0 corresponds to a pure box and 1 corresponds to the steady hypothesis. This is demonstrated in Fig. 6.17, similar to Fig. 6.14.

This test is performed by evaluating TAUNTON across a grid of the semi-variable fraction and size of the box flare as shown in Figures 6.18, 6.19. At each grid point in this space,

[9]The fitted index for NGC 1068 is 3.2 [2]

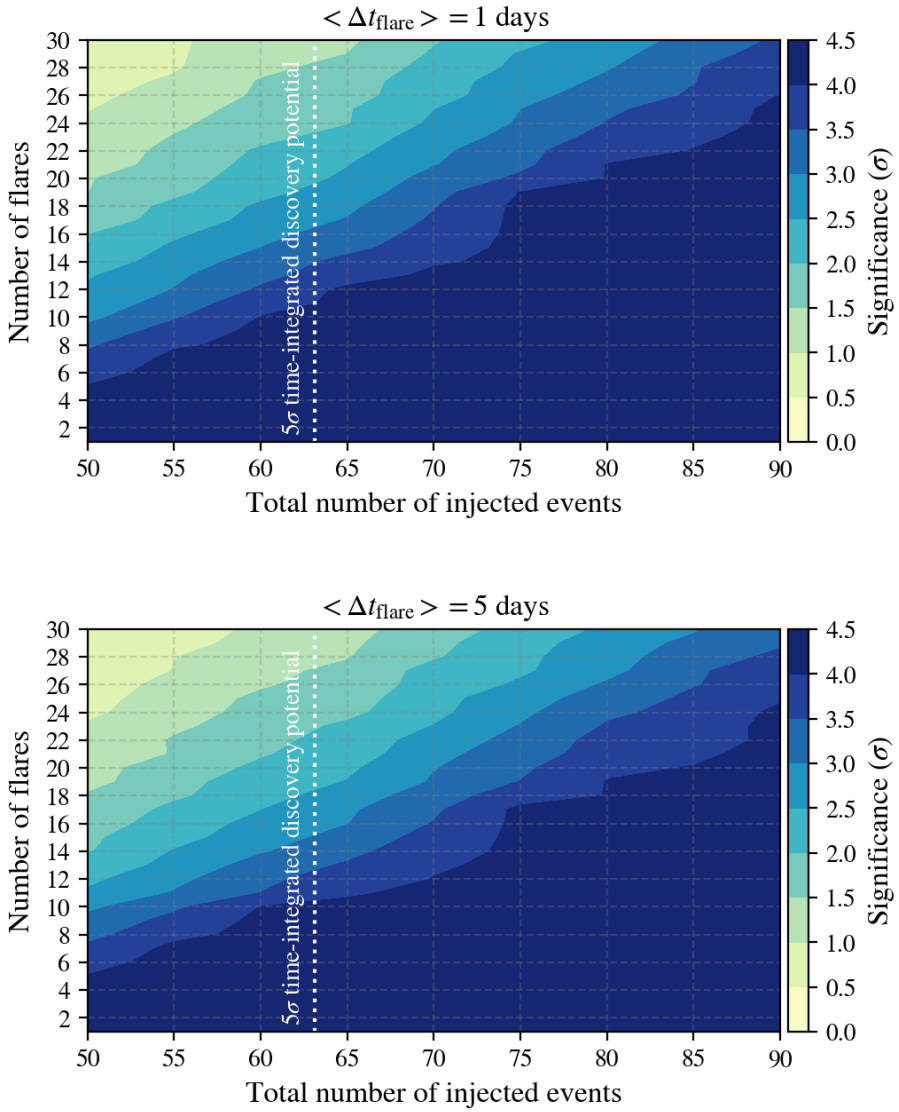

Figure 6.15: TAUNTON 's performance for distributions of the multi-box-flare signal at test declination of NGC 1068 ($\delta = -0.01°$) and soft spectral index of $\gamma = 3$. All trials in this figure are drawn from the 8.7-year Northern Tracks sample with improved reconstructions and calibration data used in [2]. Each panel is evaluated across an identical $n_{\text{inj}} \times N_{\text{flare}}$ grid. The mean box-flare size of the multiple flares used in each panel are: 1 day (top) and 5 days (bottom). The vertical dashed line demonstrates the 5σ time integrated discovery potential, so signal parameters to the right of that line would be identified as point-source in IceCube. I created this plot using the `matplotlib` package in PYTHON.

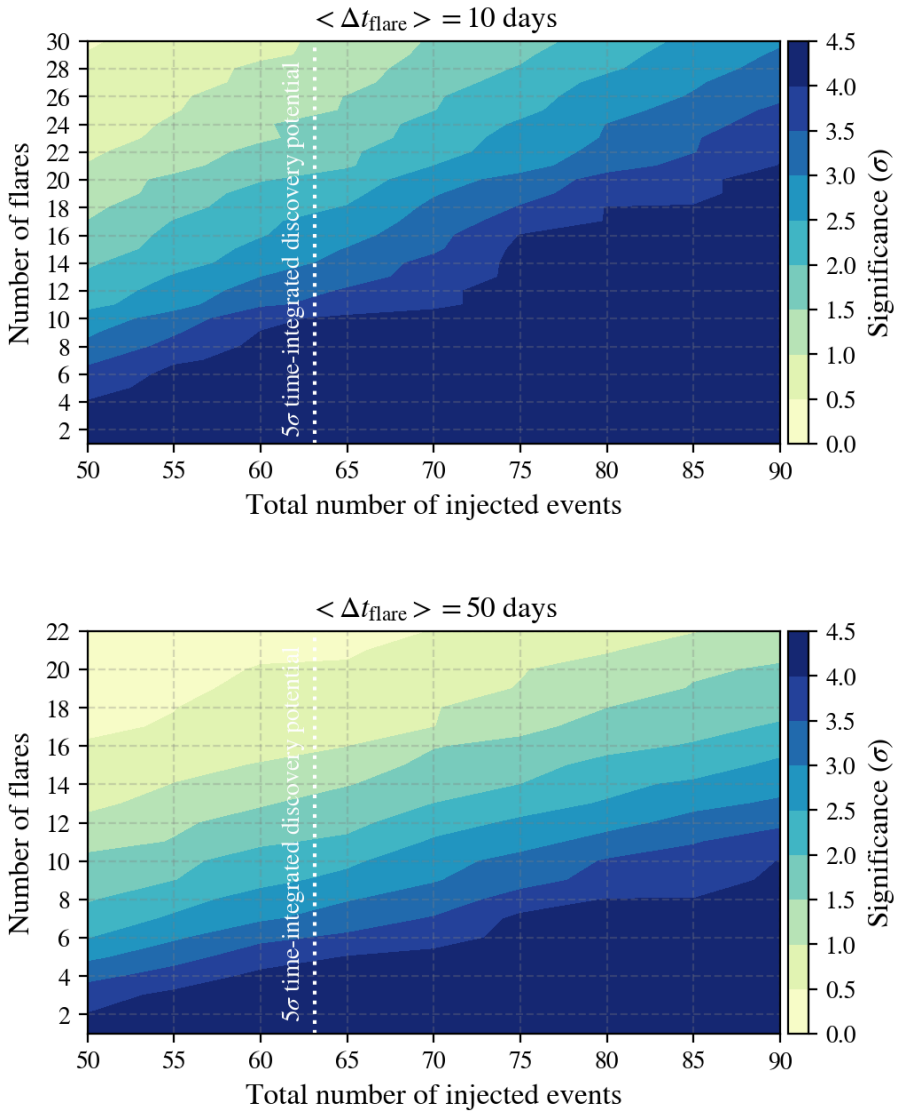

Figure 6.16: Companion plot to Fig. 6.15: TAUNTON 's performance for distributions of the multi-box-flare signal at test declination of NGC 1068 ($\delta = -0.01°$) and soft spectral index of $\gamma = 3$. All trials in this figure are drawn from the 8.7-year Northern Tracks sample with improved reconstructions and calibration data used in [2]. Each panel is evaluated across an identical $n_{\text{inj}} \times N_{\text{flare}}$ grid. The mean box-flare size of the multiple flares used in each panel are: 10 days (top) and 50 days (bottom). The vertical dashed line demonstrates the 5σ time integrated discovery potential, so signal parameters to the right of that line would be identified as point-source in IceCube. I created this plot using the `matplotlib` package in PYTHON.

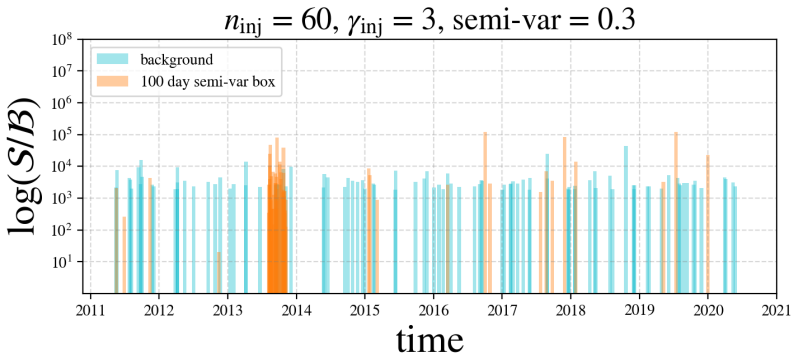

Figure 6.17: Example injection of semi-variable signal time PDFs for a trial drawn from the 8.7-year Northern Tracks sample for declination $\delta = -0.01°$. $n_{\text{inj}} = 60$ events are injected with a spectral index of $\gamma = 3$ for a flare with semi-variable fraction of 0.3. The size of the flare is 100 days, similar to Fig. 6.14, but instead of splitting a single flare, this test spreads a fraction of signal events over the livetime of the detector. I created this plot using the `matplotlib` package in `PYTHON`.

a combination of signal parameters is obtained and evaluated for test injection strengths. As we saw previously, increasing the size of the box flare, Δt_{flare}, decreases `TAUNTON` 's ability to reject the steady hypothesis. Similarly, increasing the semi-variable fraction decreases the number of signal events in the flare, if the total number of signal events is fixed. Therefore, `TAUNTON` 's sensitivity region is shorter flares, with a low semi-variable fraction, and Figures 6.18, 6.19 show how this sensitivity region expands for stronger signal strength.

This is a particularly interesting test because we do not know the temporal profile of the recently reported neutrino emission from NGC 1068 , and gives us a better understanding of the results of applying `TAUNTON` on NGC 1068 using the same data sample. This test concludes the testing of `TAUNTON` for the family of box flares and is important because astrophysical neutrino sources could very well be steady neutrino emitters with infrequent flares.

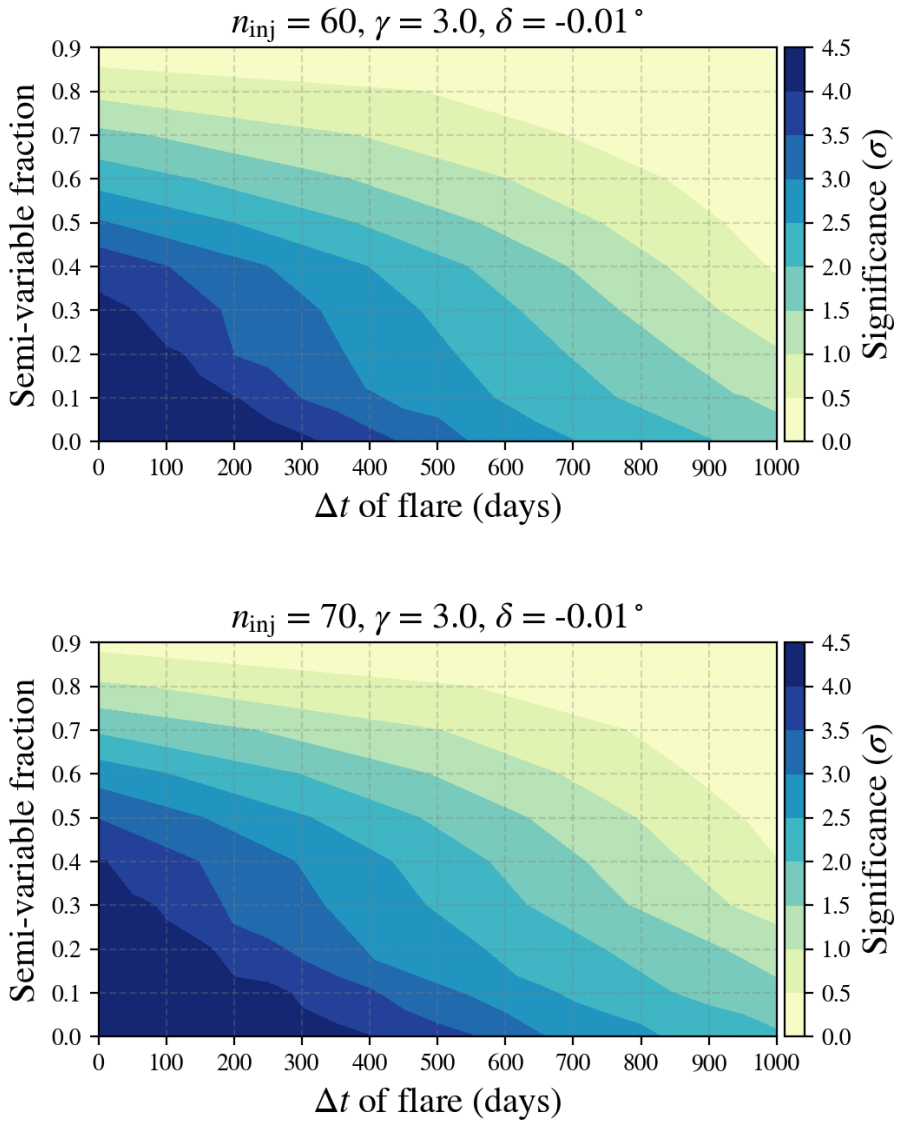

Figure 6.18: `TAUNTON` 's performance for semi-variable signal at test declination of NGC 1068 ($\delta = -0.01$) and soft spectral index of $\gamma = 3$. All trials in this figure are drawn from the 8.7-year Northern Tracks sample with improved reconstructions and calibration data used in [2]. Each panel is evaluated across an identical $\Delta t_{\text{flare}} \times \text{semi} - \text{var}$ grid. The mean number of injected events in each panel are: 60 (top) and 70 (bottom). I created this plot using the `matplotlib` package in `PYTHON`.

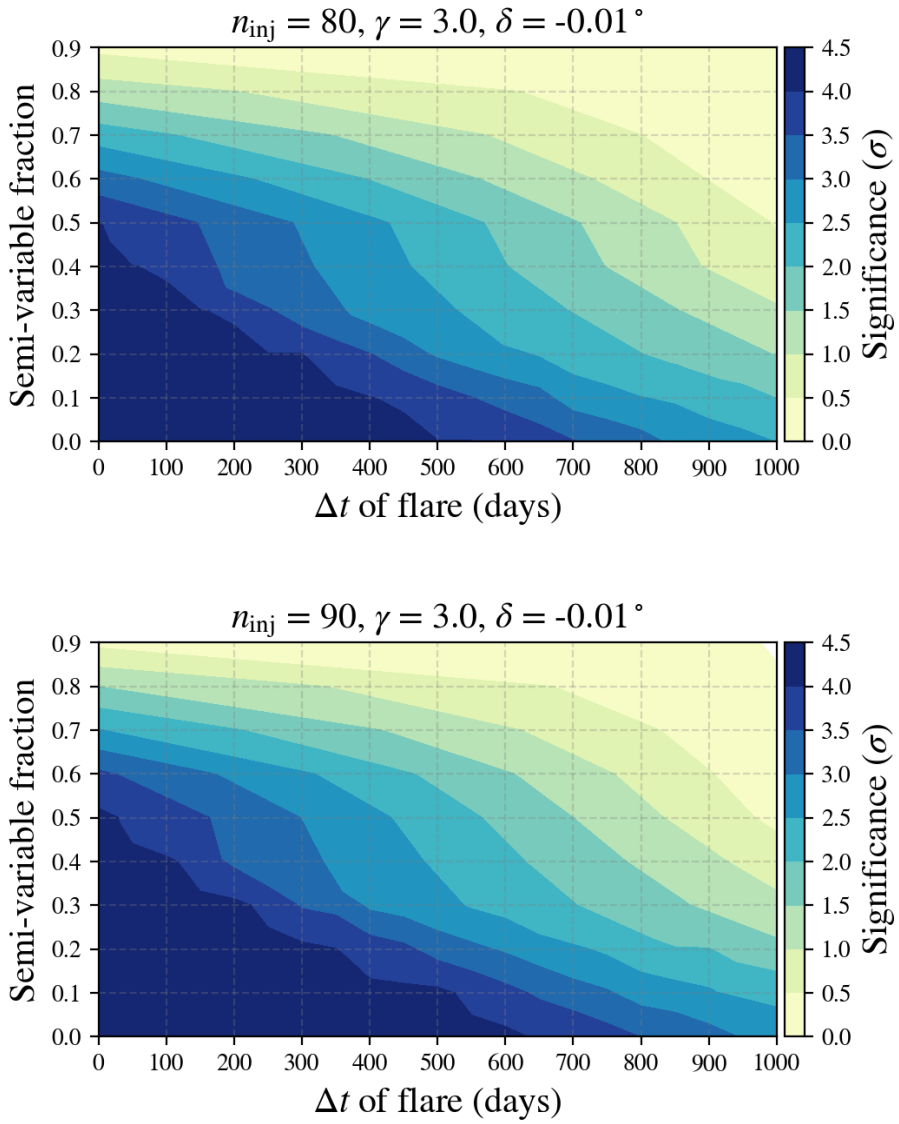

Figure 6.19: Companion plot to Fig. 6.18: `TAUNTON` 's performance for semi-variable signal at test declination of NGC 1068 ($\delta = -0.01$) and soft spectral index of $\gamma = 3$. All trials in this figure are drawn from the 8.7-year Northern Tracks sample with improved reconstructions and calibration data used in [2]. Each panel is evaluated across an identical $\Delta t_{\text{flare}} \times \text{semi} - \text{var}$ grid. The mean number of injected events in each panel are: 80 (top) and 90 (bottom). I created this plot using the `matplotlib` package in `PYTHON`.

6.3.5 Generic time-variable signal

TAUNTON 's sensitivity to box flares tells us that it needs a particularly strong time-integrated signal to reject the steady hypothesis. While an astrophysical neutrino flare could be modeled by a box, it might inherently have a different structure. This test makes use of a 47-week flux measured by Fermi for one of their bright blazars as per [125]. Assuming an astrophysical source emits neutrinos only in this 47-week window, with the same time PDF as the gamma-ray flux, I apply TAUNTON to test its validity. Note that it is known that astrophysical neutrino flare(s) might not correlate temporally with gamma-ray flare(s), as in the case of TXS 0506+56, and this time PDF is treated as a non-uniform toy model. This comparison is shown in Fig. 6.20 and we can see that the non-uniform flare performs better. This is because the time PDF extracted from the FERMI lightcurve, as shown in Fig. 6.20a is very low initially but rises rapidly past the 30-week mark for the remainder of the observation duration. Effectively, this ensures that consecutive event time differences of signal events are clustered towards smaller Δt, not unlike the case for a shorter box-flare. As we saw earlier, TAUNTON performs better for shorter flares compared to longer flares and therefore performs better for this non-uniform case demonstrated here.

6.4 Results

IceCube analyses are tested using a blinded technique as a method is developed so as to not introduce bias in the analysis. All tests performed in §6.3 utilize scrambled data for background and the relevant Monte Carlo simulation for signal events. TAUNTON underwent this approval process twice, for each data sample and coding package, before being applied to IceCube data. All results shown here utilize choice (c) of N_{ev} selection, as described in 6.2.1 and tested in 6.3.1, for the 7.5-year GFU sample. While no changes were made to the TAUNTON algorithm, more extensive testing of a time-variable signal was performed for the 8.7-year Northern Tracks sample. As TAUNTON is not meant to be a "search" tool for

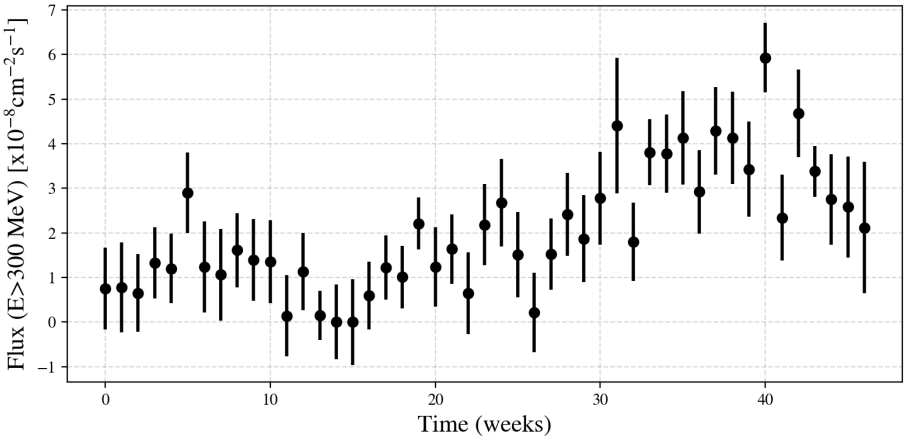

(a) Weekly FERMI lightcurve from GB6 J1542+6129 measured over a 47-week period taken from the supplementary material of [125]

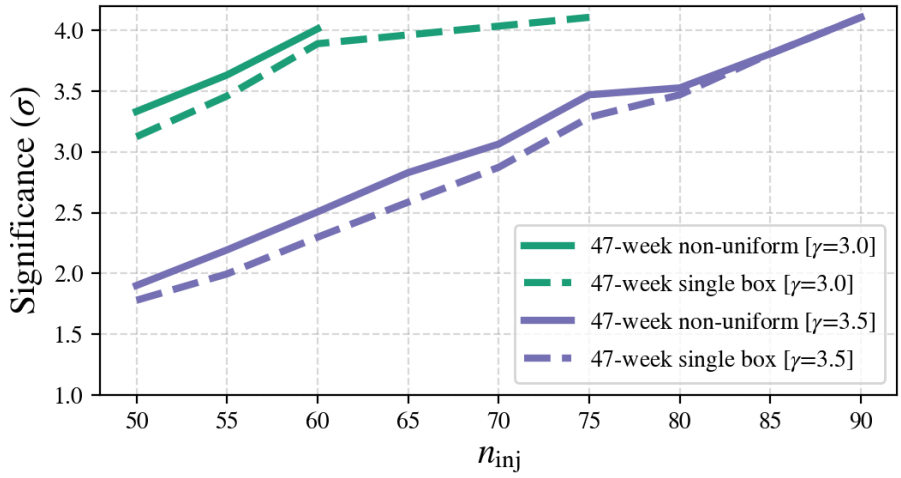

(b) TAUNTON 's ability to reject the steady hypothesis

Figure 6.20: A TAUNTON test of generic time-variability using weekly FERMI lightcurve [125] from GB6 J1542+6129 to model a non-uniform toy neutrino curve. The top panel displays the aforementioned lightcurve and the bottom panel evaluates TAUNTON 's performance by injecting this non-uniform time profile and comparing with a 47-week box-flare for increasing signal strength n_{inj} and two softer spectral indices $\gamma = 3,\ 3.5$ at a test declination of $\delta = -0.01°$ for trials drawn from the Northern Tracks sample. I created this plot using the `matplotlib` package in PYTHON.

Source	**R.A.** (°)	**Dec** (°)	n_{fit}	γ_{fit}	**TS**	reject steady?
TXS 0506+056	$77.35°$	$5.70°$	19.03	2.23	0.28	no
NGC 1068	$40.67°$	$-0.01°$	65.58	3.08	0.31	no
PKS 1420+240	$216.76°$	$23.8°$	28.83	3.14	0.29	no
GB6 J1542+6129	$235.75°$	$61.50°$	45.68	3.4	0.33	no

Table 6.1: TAUNTON results of applying time-variability test at 4 pre-selected source locations on the 7.5-year GFU data sample. Source names and locations in celestial coordinates are provided, along with the time-integrated fit parameters and the TAUNTON test statistic (TS) for each source. The TAUNTON TS reported here are consistent with the respective steady TS distributions and do not reject the steady hypothesis. Sources were selected based on a prior 10-year time-integrated study by IceCube on a different data sample [122]. I created this plot using the `matplotlib` package in PYTHON.

new candidate neutrino sources, but rather a "characterization" tool for existing candidate sources, I applied it only at the most promising hotspot locations from previous IceCube time-integrated analyses [122][2]. The post-trials correction is discussed in 6.5. Prior to applying TAUNTON on both data samples and unblinding both analyses, a 3σ local p-value threshold was set to reject the steady hypothesis. TAUNTON found no evidence of time-variability for either analysis.

6.4.1 7.5-year GFU sample

The unblinding plan for this sample was to apply TAUNTON on the 4 hottest spots found in a previous 10-year time-integrated study [122]. For each source tested by TAUNTON , no evidence of time-variability was found. The time-integrated fit parameters, as part of the TAUNTON algorithm, are also reported along with the TAUNTON test-statistic in Table 6.1.

6.4.2 8.7-year Northern Tracks sample

The unblinding plan for this sample was to apply TAUNTON on the set of objects used in the recent time-integrated search on a 110-source catalog [2], which demonstrated evidence of neutrino emission from NGC 1068 . For each of the 51 objects, which are Fermi 4FGL-DR2 sources [126], no evidence of time-variability was found. Weighting the Fermi γ-ray

flux above 1 GeV by IceCube's sensitivity at each source's declination, the 5% highest weighted sources consist of 110 sources. However, only 51 objects out of 110 yields an $n_{\rm fit}$ of at least 4 events, the predetermined minimum for `TAUNTON` . This list of objects and the `TAUNTON` results are reported in Table 6.2, sorted by the pre-trial (per-source) p-value.

Neutrino data for NGC 1068 , with a per-source (pre-trial) variability p-value of 0.9, is consistent with it being a steady neutrino source. However, TXS 0506+056 is inconsistent with the steady neutrino hypothesis at 2σ (pre-trial). This latter result is consistent with prior studies of TXS 0506+056 that found a very high energy event in September 2017 [10] and a neutrino flare in 2014-2015 [11]. While 2σ is not a strong inconsistency with the steady hypothesis, the best-fit number of events is small at $n_{\rm fit} = 5.36$. Additionally, BLL RX J1931.1+0937 is found to have an over-fluctuation in the `TAUNTON` TS, there is no evidence of time-integrated emission from this source. Figures 6.21 and 6.22 demonstrate the `TAUNTON` TS calculation for these three sources, along with a $\log(\mathcal{S}/\mathcal{B})$ time-series for TXS 0506+056 . The latter is shown explicitly because of prior time-dependent studies by IceCube in the blazar's direction [11].

Table 6.2: `TAUNTON` results of applying time-variability test on 51 Fermi 4FGL-DR2 sources, sorted by the p-value consistent with the steady hypothesis, on the 8.7-year Northern Tracks data sample. Source names and locations in celestial coordinates are provided in degrees, along with the variability test statistic ($TS_{\rm var}$) as per Eq. 6.1 and pre-trial (per-source) p-values. The 51 objects were selected from the 110-source catalog used in [2] for which the time-integrated fit yielded at least 4 events.

Source	**R.A.** (°)	**Dec** (°)	$\mathrm{TS}_{\rm var}$	$p_{\rm pre}$
RX J1931.1+0937	292.78	9.63	0.7	0.01
NGC 5380	209.33	37.5	0.65	0.03
TXS 0506+056	77.36	5.7	0.62	0.04
B2 2234+28A	339.1	28.48	0.53	0.09
S2 0109+22	18.03	22.75	0.49	0.12
Continued on next page				

Table 6.2 continued from previous page

Source	R.A. (°)	Dec (°)	TS	p_{pre}
B2 1215+30	184.48	30.12	0.48	0.11
Mkn 421	166.12	38.21	0.48	0.13
OJ 287	133.71	20.12	0.46	0.13
4C +55.17	149.42	55.38	0.42	0.22
IC 678	168.56	6.63	0.4	0.22
PMN J0948+0022	147.24	0.37	0.39	0.27
LQAC 284+003	284.48	3.22	0.39	0.27
TXS 0518+211	80.44	21.21	0.39	0.29
NVSS J141826-023336	214.61	-2.56	0.38	0.33
B2 0619+33	95.73	33.43	0.37	0.28
PKS 0235+164	39.67	16.62	0.36	0.34
PKS 0735+17	114.54	17.71	0.35	0.35
Mkn 501	253.47	39.76	0.34	0.39
B2 1520+31	230.55	31.74	0.34	0.34
4C +38.41	248.82	38.14	0.34	0.34
M 31	10.82	41.24	0.33	0.42
NGC 1275	49.96	41.51	0.33	0.43
S5 1044+71	162.11	71.73	0.33	0.34
S3 0458-02	75.3	-1.97	0.32	0.47
B2 2308+34	347.77	34.42	0.32	0.45
PKS 0736+01	114.82	1.62	0.32	0.46
7C 2010+4619	303.02	46.49	0.31	0.41
PKS 0336-01	54.88	-1.78	0.3	0.55
OG 050	83.17	7.55	0.29	0.55

Continued on next page

Table 6.2 continued from previous page

Source	R.A. (°)	Dec (°)	TS	$p_{\rm pre}$
RGB J2243+203	340.99	20.36	0.29	0.56
B2 0218+357	35.28	35.94	0.29	0.55
4C +14.23	111.32	14.42	0.27	0.66
B2 2114+33	319.06	33.66	0.27	0.65
B3 1343+451	206.39	44.88	0.27	0.64
Arp 299	172.07	58.52	0.26	0.69
OX 169	325.89	17.73	0.26	0.69
BL Lac	330.69	42.28	0.25	0.72
MG2 J201534+3710	303.89	37.18	0.25	0.72
TXS 1055+567	164.67	56.46	0.25	0.72
B3 0609+413	93.22	41.37	0.24	0.67
GB6 J1542+6129	235.76	61.5	0.24	0.74
NVSS J184425+154646	281.12	15.79	0.24	0.76
PKS B1130+008	173.2	0.57	0.23	0.8
3C 273	187.27	2.05	0.23	0.79
SBS 0846+513	132.51	51.14	0.23	0.79
PKS 1717+177	259.81	17.75	0.22	0.8
NGC 1068	40.67	-0.01	0.19	0.9
OJ 014	122.86	1.78	0.18	0.95
TXS 0603+476	91.86	47.66	0.17	0.97
PKS 1424+240	216.76	23.8	0.16	0.97
1ES 1959+650	300.01	65.15	0.16	0.97

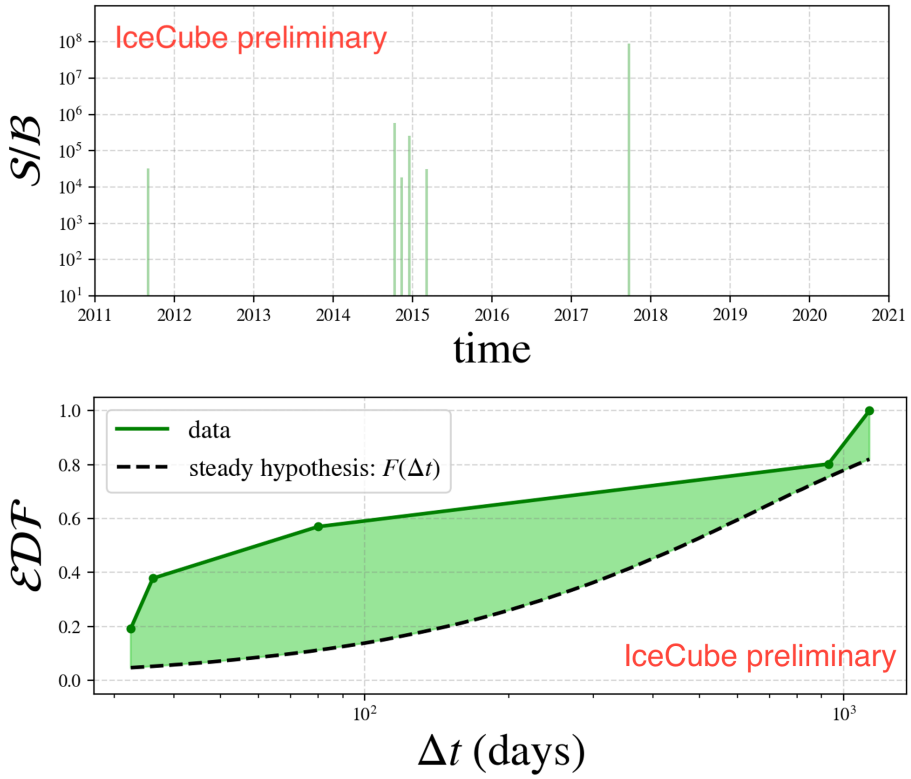

Figure 6.21: `TAUNTON` 's evaluation of the $N_{\text{ev}} = 6$ largest $\log(\mathcal{S}/\mathcal{B})$ events in the direction of blazar TXS 0506+056 using the 8.7-year Northern Tracks sample. This result is inconsistent with the steady hypothesis at 2σ per-source (pre-trial) significance. The top panel shows the time series of the 6 events, including IC170922A that passes the criteria set by the N_{ev} selection. The bottom panel shows the TS calculation performed by `TAUNTON` for these 6 events, as compared to the steady hypothesis, as per Fig. 6.2.3. I created this plot using the `matplotlib` package in `PYTHON`.

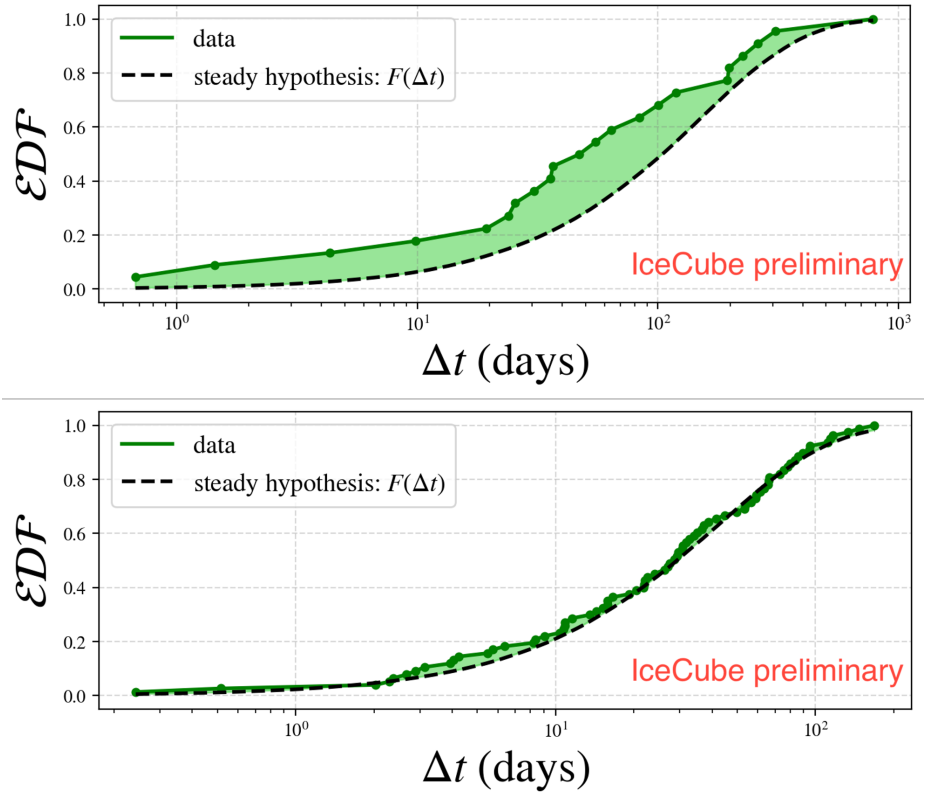

Figure 6.22: TAUNTON 's evaluation of the largest N_{ev} $\log(\mathcal{S}/\mathcal{B})$ events in the direction of select Fermi 4FGL-DR2 sources, RX J1931.1+0937 and NGC 1068 . The latter is found to be consistent with the steady hypothesis tested by TAUNTON with a per-source (pre-trial) p-value of 0.9. TAUNTON calculates the test statistic based on the consecutive time-difference of N_{ev} events and compares it to the steady expectation, as per Fig. 6.2.3. I created this plot using the matplotlib package in PYTHON.

6.5 Discussion

I explored and presented a new non-parametric method, TAUNTON , to test time-variability for candidate neutrino sources. This test is analogous to Fermi's variability index that is used to characterize existing γ-ray sources observed by Fermi-LAT [125]. The key difference between the Fermi test and TAUNTON is that temporal binning is not required. This is important for neutrino data observed by IceCube as we expect a handful of signal events among a large number of background events. For γ-ray data observed by Fermi-LAT, the sources are extremely bright, $> 50\sigma$, and the source retains its significance when data is binned monthly or weekly. For neutrino data, each event can be assigned a weight, $\log(\mathcal{S}/\mathcal{B})$, that is expected to be large for signal events as opposed to background events. However translating event weights to say, a weekly-binned flux is not meaningful. Finally, TAUNTON also takes into account detector effects such as seasonal variability of atmospheric neutrinos intrinsically by incorporating it into the steady hypothesis distribution functions.

TAUNTON requires at least $N_{\rm ev} \leq 4$ number of neutrino events in the source direction and performs best for bright, time-integrated sources. I applied this method to 4 objects in the GFU data sample, and 51 objects in the Northern Tracks sample, which are all Fermi-4FGL-DR2 sources [126]. All 51 unique objects are in the northern sky, where IceCube's sensitivity is optimal. Setting a per-source (pre-trial) threshold of 3σ, we do not find any evidence for time variability. Post-trials correction, that is correcting for the look-elsewhere effect, is performed on the per-source (pre-trial) p-values on the Northern Tracks sample using an $n = 110$ Sidak correction [127].

The most interesting are the results of this time-variability test applied to the Seyfert II and starburst galaxy NGC 1068 , IceCube's strongest time-integrated neutrino source candidate with a fit of $n_{\rm fit} = 79$ signal events. The $N_{\rm ev} = 78$ largest $\log(\mathcal{S}/\mathcal{B})$ events are consistent with the steady hypothesis at a per-source (pre-trial) p-value of 0.9. If NGC 1068 is

a neutrino source with a single power-law index $\gamma = 3$, all ~ 80 events in a flare of size 1-600 days would be identified as time-variable emission by TAUNTON . Additionally, a shorter neutrino flare of size 1-300 days with $\lesssim 50\%$ of the ~ 80 events would reject the steady signal hypothesis with 3σ 50% of the time. We can conclude, that if NGC 1068 is a real neutrino source, IceCube data best describes it as a steady source. Additionally, if NGC 1068 is a steady neutrino source, we would need ~ 150 events to identify it as a point source with a power of 10σ over the background. This level of background rejection is achievable with the IceCube-Gen 2 [128] and with such a strong neutrino signal, TAUNTON 's ability to reject the steady hypothesis automatically increases. This is shown in Fig. 6.23 for the semi-variable test. As IceCube continues to operate and maintain its impressive up-time, as well as the planned IceCube-Gen2 upgrade, ensures that a truly steady neutrino source will gradually get brighter in IceCube. The TAUNTON algorithm including my analysis code has been internally checked for reproducibility and added to IceCube's internal repository for future use with two point-source search packages. In this way, the TAUNTON algorithm adds to IceCube's existing tools for point-source studies and provides additional room for testing and interpretations in the event of a successful point-source neutrino search in the future.

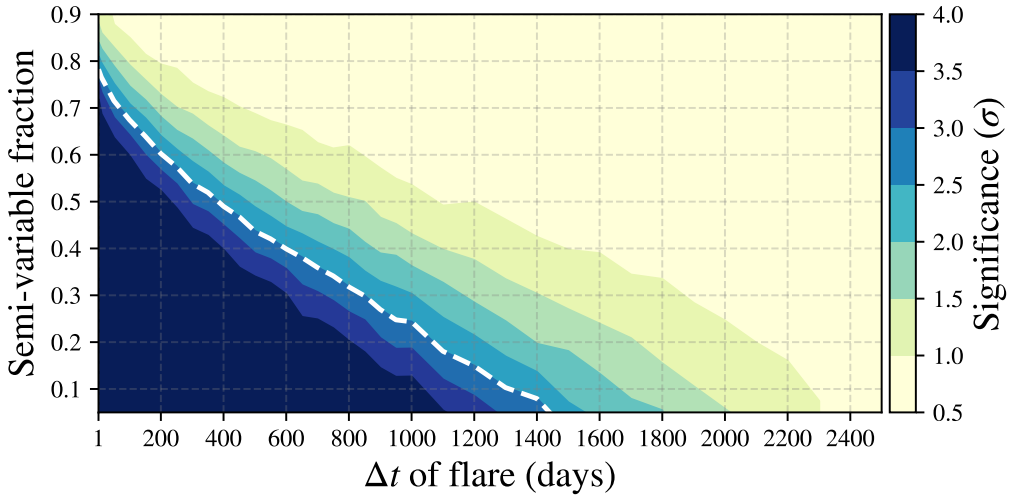

Figure 6.23: Semi-variable TAUNTON test of a simulated source, that would have been identified with a significance of 10σ excess over the background, with $n_{\text{inj}} = 152$ events, spectral index of $\gamma = 3$ at a declination of $\delta = -0.01°$. With IceCube-Gen2, such a strong neutrino signal can be identified in the future and boosts TAUNTON 's ability to differentiate between signal variability and a steady source. The dashed white line is the 3σ TAUNTON contour and is added for reference. I created this plot using the matplotlib package in PYTHON.

CHAPTER 7
SEARCH FOR NEUTRINOS FROM EVAPORATING PRIMORDIAL BLACK HOLES

7.1 Motivation

Despite the fact that there is no evidence for the existence of primordial black holes (PBHs), they have been a source of interest for nearly 50 years [17]. PBHs can be light enough for Hawking radiation to be observable, as we saw in Ch. 3. Hawking radiation elegantly unifies general relativity, quantum field theory, and thermodynamics and experimental confirmation of Hawking radiation itself is yet another puzzle associated with the process. PBHs originally lighter than $\sim 10^{15}$ g would have evaporated by now due to Hawking radiation, so our current understanding of their existence[10] can be broadly categorized by this dividing mass limit. On the one hand, there are searches for evaporating PBHs (also referred to as PBH bursts), on the other, there are constraints on the fraction of dark matter that can be accounted for by PBHs (a higher mass that would not have evaporated over the age of the universe). In this chapter, I present a search for neutrino emissions from nearby PBHs that are evaporating using IceCube data, assuming Hawking radiation. In §7.2, I describe the method and in §7.3, I present the sensitivity of this search. This sensitivity is calculated by injecting the time and energy-dependent muon neutrino flux at Earth from PBH evaporation as discussed in Ch 3 and demonstrated in Fig. 3.4. In §7.5, I give an overview of the current constraints, prior searches for evaporating holes performed by γ-ray experiments, and present the constraints imposed by this study.

[10] Or lack thereof

7.2 Analysis Method

The PBH search method presented in this dissertation uses high-level IceCube data that uses timing, directional, and energy information. Specifically, this analysis is applied to the 8.7-year Point Source Tracks (PS Tracks) sample by performing an all-sky time-dependent point-source search in the northern celestial sky ($\delta > -5^{\circ}$). These techniques have been applied to other IceCube event selections, however, this is the first time high-energy neutrinos are used to search for PBHs. The time-dependent search techniques used by IceCube are well described in literature [119]. For this analysis, I modified an internal coding library, `csky`, originally developed by Dr. Mike Richman, to inject the signal expected from an evaporating PBH. Prior point-source searches using and updating `csky` have been performed for time-integrated and time-dependent point-source searches with IceCube [129] [120]. In this section, I will describe how the standard time-dependent search is modified for PBHs and build on the techniques described in §5.8, by using the expected neutrino flux from an evaporating PBH at Earth as described in 3.3.

7.2.1 Likelihood

Given a search location in the celestial sky, the standard time-dependent unbinned likelihood method used by IceCube fits a box flare with four free parameters: $n_s,\ \gamma,\ T_0,\ \Delta t$ [119], where $n_s,\ \gamma$ are consistent with the definitions provided in §5.8 and $T_0,\ \Delta t$ is the central time and width of the box-flare [119] [11]. The PBH search presented in this dissertation fixes the width parameter, Δt, while fitting T_0. For this analysis, T_0 represents the ending edge of the box flare as shown in Fig. 7.1 which is the time of complete evaporation of the PBH, after which no emission is expected. This time-dependent modification now includes using the event times, t_i, to evaluate the signal and background PDFs, along with the likelihood as shown below:

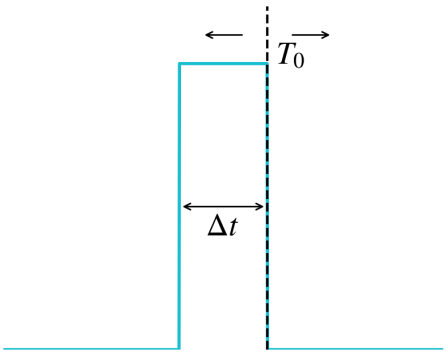

Figure 7.1: Example time PDF used by the point-source time-dependent search for PBHs. Here T_0 is a fitted parameter, while Δt is the fixed duration of the search.

$$\mathcal{L}(n_s,\ \gamma,\ T_0) = \prod_i^N \left[\frac{n_s}{N} \mathcal{S}_i + \frac{N - n_s}{N} \mathcal{B}_i \right] \tag{7.1}$$

$$\mathcal{S}_i(E_i, \vec{x}_i, t_i) = \Theta_i^s(\vec{x}_i | \vec{x}_s, E_i) \cdot \mathcal{E}_i^s(E_i, \sin\delta_i; \gamma) \cdot \mathcal{T}_i^s(t_i; T_0) \tag{7.2}$$

$$\mathcal{B}_i(E_i, \vec{x}_i, t_i) = \Theta_i^s(\vec{x}_i | \text{bkg}, E_i) \cdot \mathcal{E}_i^b(E_i, \sin\delta_i) \cdot \mathcal{T}_i^b \tag{7.3}$$

This is very similar to the time-integrated likelihood. The signal and background PDFs are composed of the spatial, energy and time components, wherein the spatial (§5.8.2) and energy terms §5.8.3 remain the same as before. As the background expectation in time is uniform across the livetime of the detector, the background time PDF is simply a constant factor $\mathcal{T}_i^b = 1/\text{livetime}$. Similarly, given a fixed box-width (Δt), the signal time PDF is given by:

$$\mathcal{T}_i^s(t_i) = \begin{cases} 1/\Delta t, & \text{if } T_0 \geq t_i \geq T_0 - \Delta t \\ 0, & \text{otherwise} \end{cases}$$

The test statistic is evaluated by fitting 3 parameters similar to the time-integrated search with 2 free parameters (see §5.8.4):

$$\mathrm{TS} = 2\log\left[\frac{\mathcal{L}(\hat{n}_s, \hat{\gamma}, \hat{T}_0)}{\mathcal{L}(n_s = 0)}\right] \tag{7.4}$$

For a given search location ($\vec{x}_s$) and search duration (Δt), in order to perform the maximization procedure, events are selected in a $10^\circ \times 10^\circ$ box around the search location. While the minimization procedure is similar to the time-integrated method, there is an additional step to incorporate the temporal component. This is because time-dependent analyses with fitted flare profiles are notoriously challenging for the minimizer. In order to tackle this, $\log(\mathcal{S}/\mathcal{B})$ for all events to be considered are evaluated at multiple spectral indices with the parameter bounds, $\gamma \in \{1, 2, 3, 4\}$. Then, events that pass a pre-defined $\log(\mathcal{S}/\mathcal{B})$ threshold value are considered as seeds. That is, the event times t_i's in this list of events form the list of seed T_0's to ensure that each seeded flare starts or ends at an event. For this particular analysis, this means that the seeded flares are ensured to end at an event time. Note that this list of seeded flare end times is computed for 4 spectral indices. Minimizations are then performed for each seeded flare to fit $n_s,\ \gamma$ similar to a time-integrated search, and the minimization with the largest TS (or smallest negative TS) is chosen as the best-fit flare. Essentially, the minimizer is not directly utilized to fit T_0, as methods such as gradient descent are not directly applicable when the parameter space is discontinuous. That is, in this case, the flare has to begin and end at an event time, and event times are themselves discontinuous.

Naturally, it is important to consider the ramifications of choosing the pre-defined $\log(\mathcal{S}/\mathcal{B})$ threshold value. Ideally, we would want a threshold value that is as low as possible to allow all events to be considered as the event at which the fitted flare can start/end. The cost of choosing a lower $\log(\mathcal{S}/\mathcal{B})$ threshold value is the higher computational time for the final minimization, as the number of seeded flares increases the number of minimizations required per search. For this analysis, the $\log(\mathcal{S}/\mathcal{B})$ threshold value was chosen to

be 1 which is lower than other time-dependent IceCube searches. Computationally, this is not as expensive as an identical choice for the typical time-dependent search, because this analysis does not fit Δt and has one less parameter than the typical time-dependent search. The ability to choose a lower $\log(\mathcal{S}/\mathcal{B})$ threshold was an important factor in deciding to fix Δt for this analysis.

7.2.2 TS distributions

In order to test the performance of this time-dependent point-source search, simulated events are injected along with scrambled data near the search location, that correspond to the signal and background hypothesis $\mathcal{H}_1$. Since all IceCube point-source searches are first tested on blinded or scrambled data, the likelihood method and the aforementioned prescription remains the same for blind background trials, blind background trials with injected signal, and unblinded data. Similar to the time-integrated search (§5.8.4), larger TS values correspond to cases where the signal hypothesis $\mathcal{H}_1$ is much more likely than the background hypothesis $\mathcal{H}_0$. The distribution of TS for identical realizations or signal parameters allows us to evaluate the performance of this search.

The TS distributions for a collection of blind background trials at a test declination of $\delta = 0^\circ$ are shown in Fig. 7.2. A demonstrative χ^2-fit is performed for these background-only trials, similar to the example TS distributions for a time-integrated search in Fig. 5.10. Each trial corresponds to a minimization performed by the time-dependent likelihood prescribed in §7.2.1. See that the tails of the distributions get marginally larger for longer search windows. This is because there is a higher chance to fit a larger n_s when there are more events in the larger search windows, and a larger n_s directly affects the TS as per Eq. 7.3. This is also reflected in the number of degrees of freedom, $n_{\rm dof}$, for the fitted χ^2 distribution. Since 3 parameters are fitted, the expected $n_{\rm dof}$ is between 2 and 3 identical to how the expected $n_{\rm dof}$ for a 2-parameter time-integrated search is between 1 and 2.

In addition to the TS distributions for blind background trials, it is also informative to

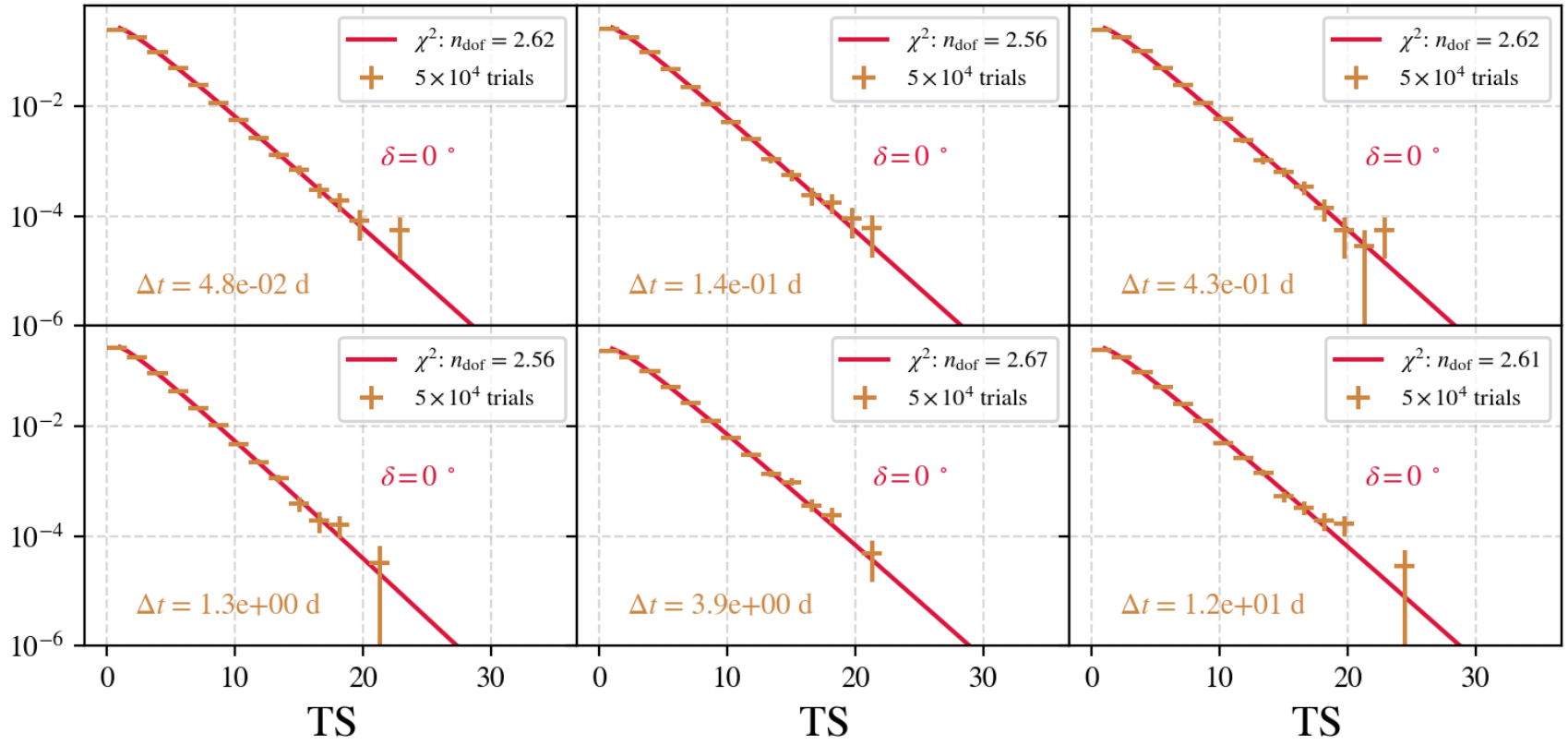

Figure 7.2: Example background-only TS distributions at a test declination of $\delta = 0°$ for the time-dependent point-source PBH search using the 8.7 year PS Tracks sample. Each panel corresponds to the six search windows that correspond to fixed Δt's for the minimization described in the text. A χ^2-fit to the distribution is provided in red for reference, along with the fitted number of degrees of freedom in the legend. I created this plot using the `matplotlib` package in `PYTHON`.

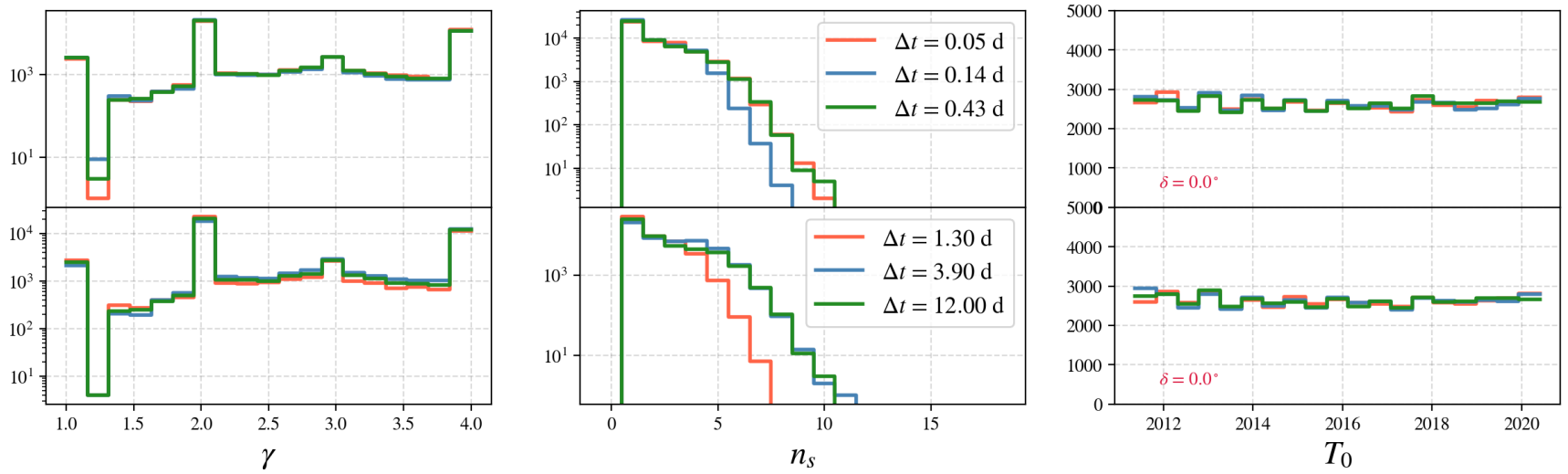

Figure 7.3: Example distributions of the fitted parameters, n_s, γ, T_0, at a test declination of $\delta = 0°$ for the time-dependent point-source PBH search using the 8.7 year PS Tracks sample. The top panel corresponds to the three shortest search windows, while the bottom panel corresponds to the three longest search windows. I created this plot using the `matplotlib` package in `PYTHON`.

inspect the distributions of the best-fit parameters to ensure that the minimization procedure is working as expected. These are shown in Fig. 7.3 for the same trials as the aforementioned TS distributions. Firstly, we expect the fitted T_0 to have no preference across the livetime of the detector so the uniform $\hat{T}_0$ distribution is expected. Next, the fitted n_s distributions roughly follow the corresponding TS distributions as larger TS values or over fluctuations correspond to a larger $\hat{n}_s$. Finally, the fitted γ distributions are expected to be flat, except for a peak at $\gamma = 4$ because these are background-only trials. We see the effects of seeding in the minimization procedure, which corresponds to the smaller peaks with bin-centers at $\gamma = 1, 2, 3, 4$. This is not a problem because the fitted n_s peaks at 0 where the index does not contribute to the TS. As previously mentioned, this seeding effect is unique to time-dependent likelihoods where minimization is non-trivial.

7.3 Sensitivity

In order to evaluate the sensitivity of this analysis to PBH evaporation, I inject simulated events from Monte Carlo that follow the time and energy-dependent neutrino flux at Earth expected in the final[11] 11.57 days. All prior point-source studies by IceCube have utilized a separable time and energy component for injected signal so this is the first time signal has been injected that does not assume a time-independent index for the flux [119, 11, 120, 121]. The cumulative time-integrated flux, for select times to evaporation, is shown in Fig. 3.4 which demonstrates how this flux changes with time. The choice of distance to PBH, $d_{\rm ref}$ in Eq. 3.9, simply serves as a scaling factor, as will see later. The sensitivity to PBH evaporation is more meaningful when translated into a `sensitivity distance`, and consequently an estimate of the detectable volume. This volume represents the region around the detector, in our local universe, such that if a PBH evaporated in this region, IceCube would be able to detect a significant[12] amount of signal events over the background. Consequently, the livetime of this search along with the detectable volume is converted

[11] See Ch. 3 for the justification of this duration

[12] The relevant thresholds are defined and explained in §7.3.1

into a burst-rate upper limit upon null-detection. This section prescribes the aforementioned steps in this analysis from injection to the calculation of the detectable volume. This volume is converted into an upper limit in section 7.5 after considering results from the unblinded data in 7.4.

7.3.1 Injection sensitivity

The 11.57-day (10^6 s) injection is performed in 29 log-spaced time-bins from $0 - 10^6$ s to capture the increasing neutrino flux as the hole evaporates. For instance, for a $0.35 - 1.16$ day time-bin prior to evaporation, this emission peaks at $\sim 10^3$ GeV and for a $1-3$ seconds time-bin prior to evaporation, this emission peaks at 2×10^4 GeV. These bins are then appropriately weighted by the energy-dependent flux and the effective area of the PS Tracks data sample, or the expected number of neutrinos given that flux over that particular time-bin. Note that the effective area is declination-dependent, so this injection scheme depends on the declination at which simulated events are injected. Once the injection scheme is established, blind background trials with injected signal events are evaluated by the test statistic and are referred to as the signal TS distributions. This signal TS distribution is then compared with blind background-only trials to establish the sensitivity to the injected signal.

Two errors are typically assessed in hypothesis testing: type I error, known as "false positive", and type II error known as "false negative". The type I error refers to the rejection of the null hypothesis ($\mathcal{H}_0$) when it is correct. Alternatively, type II error is when the null hypothesis is not rejected when it is incorrect. Sensitivity can then be defined by setting the confidence level, $\alpha = 0.5$, and power at $\beta = 0.95$. For the likelihood ratio test used in this analysis, this means finding the mean signal strength, n_s, such that 95% of signal trials TS are larger than 50% of the background-only trials TS. For reference, IceCube's definition of *sensitivity* is 90% of signal trials TS are larger than 50% of the background-only trials TS. A stronger constraint on the type 1 error: $\alpha = 5\sigma$ and $\beta = 0.5$ is used to

define *discovery potential* by IceCube. These thresholds are a matter of convention for the specific field of study, and ideally, we would want high $\alpha,\ \beta$ values. In order to match the variety of definitions used by the community, I will be presenting three choices of statistical thresholds in this dissertation:

- $\alpha = 0.5,\ \beta = 0.95$: This threshold will be used for comparison purposes
- $\alpha = 0.5,\ \beta = 0.99$: This threshold will be used to define the final upper limit of this study
- $\alpha = 5\sigma,\ \beta = 0.5$: This threshold will be used for comparison purposes

Note that, for typical flare-search methods employed by IceCube [119], the sensitivity ($\alpha = 0.5,\ \beta = 0.9$) and discovery potential ($\alpha = 5\sigma,\ \beta = 0.5$) behave differently at smaller timescales of $< 0.5days$. That is, for very short flares, it is easier to satisfy the discovery potential threshold than the sensitivity threshold because the TS distributions become wider; consequently we require fewer events to reach the discovery potential than sensitivity. Additionally, none of these thresholds match the HAWC threshold of $\alpha = 5\sigma,\ \beta = 0.99$ for their PBH search [19]. This will be addressed in the future with additional statistics to match thresholds and properly compare with the HAWC PBH burst-density limits.

While the specific definitions of sensitivity or discovery potential can change depending on $\alpha,\ \beta$, the relevant signal parameter ($n_{\rm sens}$ or $n_{\rm disc}$) is computed in this analysis by iteratively injecting a stronger signal until the desired statistical power is exceeded. It is denoted as $n_{\rm sens,90\%}$ for $\beta = 0.9$ or $n_{\rm sens,95\%}$ for $\beta = 0.95$. A threshold TS that corresponds to the desired statistical power is computed from blind background-only trials at a given declination. This allows for signal efficiency curves, as shown in Fig. 7.4, where the Poisson mean number of injected events is iteratively increased in a pre-defined range. Each set of signal trials corresponds to a mean number of injected events and search window, and the corresponding β values asymptote to 1. That is, increasing the injected mean number of signal events increases TS, and we see a larger passing frac-

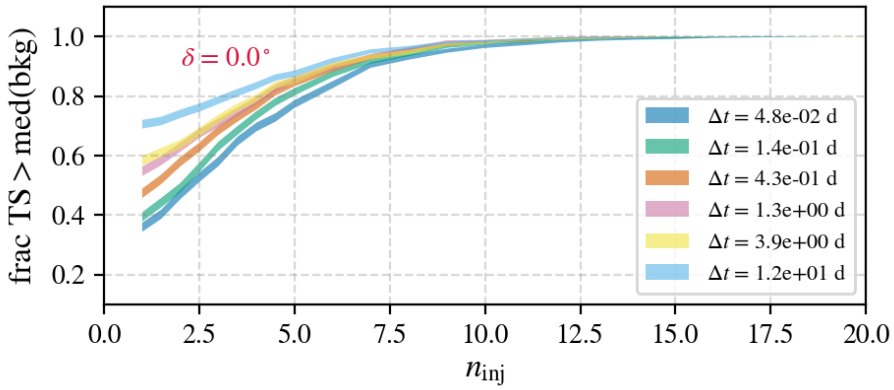

Figure 7.4: Example signal efficiency curves for injected signal events at a test declination of $\delta = 0°$. Each colored solid line corresponds to the unbinned likelihood method's fixed search windows from 0.05 to 11.5 days as explained in the text. I created this plot using the `matplotlib` package in `PYTHON`.

tion above the threshold TS. A smaller sample of 10^3 signal trials is used for each search window, per declination and injected mean number of signal events. This sampling uncertainty is included while calculating the efficiency curves, and these are interpolated using the `scipy.interpolate.PchipInterpolator` routine. The relevant mean signal strength, n_{sens} or n_{disc}, is then solved by using Brent's root-finding algorithm provided by the `scipy.optimize.brentq` routine [116].

Fig. 7.5 shows the sensitivity of this analysis to PBH evaporation using the statistical thresholds of $\alpha = 0.5,\ \beta = 0.95$. The declinations in the northern sky are sampled linearly in $\sin\delta$ to sample near-equal areas in a unit sphere. The chosen declinations are $\delta \in \{-4.98°,\ 0.0°,\ 4.98°,\ 10°,\ 20.6°,\ 32°,\ 45.59°,\ 64°,\ 80.27°\}$, with additional declinations chosen near the horizon to resolve fluctuations. For each declination and search window, 5×10^4 blind background-only trials are evaluated to determine the threshold TS, which in this case is the median. See that there exists a sweet spot for the search window, that is longer search windows suffer from more background events requiring a larger n_{sens}. Conversely, for shorter search windows, the search misses out on a potential signal from the final 11.57 days of PBH evaporation. For this specific choice of statistical threshold, the shortest search ($\Delta t = 4.8 \times 10^{-2}$ days) performs the worst across the northern sky due

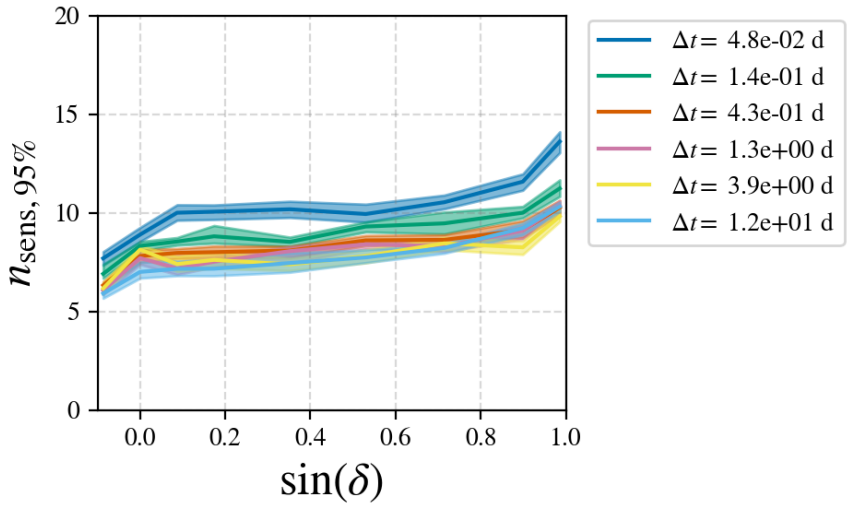

Figure 7.5: Northern-sky injection sensitivity of PS Tracks sample to the final 11.57 days of PBH evaporation. The required mean number of signal events over background for $\alpha = 0.5,\ \beta = 0.9$ is plotted against $\sin\delta$ for chosen declinations in the northern celestial sky. Each color represents the size of the 6 search windows used in this analysis, while the relevant shaded bands estimate the 1σ statistical uncertainties as described in the text. I created this plot using the `matplotlib` package in `PYTHON`.

to missing out on potential signal events from PBH evaporation beyond the search. In the next section, I will detail the calculations required to convert this n_{sens} into a sensitivity distance, d_{sens}.

7.3.2 Sensitivity distance

For the sampled declinations in the northern celestial sky, I calculate n_{ref} using the flux prescribed in Eq. 3.9 and the effective area of the PS Tracks sample outlined in 5.7.2. The choice of $d_{\mathrm{ref}} = 0.01$ pc in this calculation is now used to compare n_{ref} and n_{sens} by using the relation $n \propto 1/d^2$:

$$d_{\mathrm{sens}} = d_{\mathrm{ref}} \sqrt{\frac{n_{\mathrm{ref}}}{n_{\mathrm{sens}}}} \tag{7.5}$$

See that the choice of statistical threshold translates directly to d_{sens}. A stronger thresh-

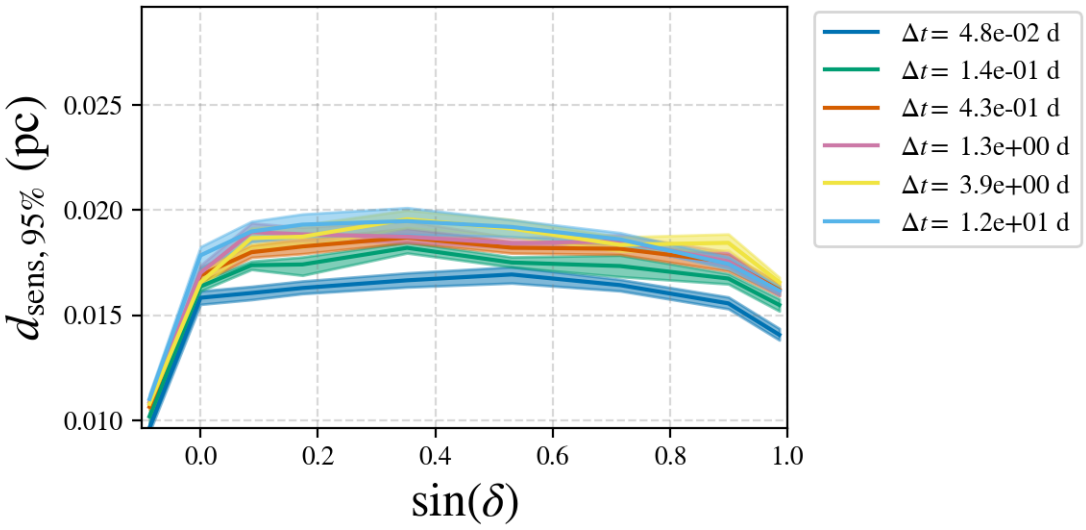

Figure 7.6: Northern-sky sensitivity distance of the PS Tracks sample to the final 11.57 days of PBH evaporation. Each color represents the size of the search window, while the relevant shaded bands translate the 1σ statistical uncertainties from calculating n_{sens} as described in the text. I created this plot using the `matplotlib` package in `PYTHON`.

old will require a larger n_{sens}, and consequently, be sensitive at a smaller distance. Additionally, since n_{ref} is the estimated signal events during the final 11.57 days of a PBH evaporation, it only depends on the declination of the source or PBH in this case. d_{sens} is shown for the sampled declinations in the northern celestial sky in Fig. 7.6 for the 6 search windows, using the statistical thresholds of $\alpha = 0.5,\ \beta = 0.95$.

As a way to include systematic uncertainties in this analysis, I explored variations in n_{ref} based on choices that determine the calculation of the PBH flux at Earth. The first is, x_{min}, which is an `HDMSpectra` parameter. This parameter, described in §3.3, is used to allow the calculation of lower energy decay products from the PBH. That is, for particles emitted directly from the PBH, $x \in [x_{\mathrm{min}}, 1]$ is the range of allowable final (decay/hadronization) particle energies. This analysis uses $x_{\mathrm{min}} = 10^{-4}$, but values of 10^{-6} and 10^{-2} were also explored for test declinations of $\delta = \{-4.98^{\circ},\ 0.0^{\circ},\ 4.98^{\circ}\}$. While no difference was found in calculating n_{min} for $x_{\mathrm{min}} = 10^{-4}, 10^{-6}$, n_{ref} was found to be $\sim 0.007\%$ smaller for $x_{\mathrm{min}} = 10^{-2}$. This indicates that the calculation of n_{ref} was fairly robust to the choice

of $x_{\min}$ for this analysis. I explored another cause of fluctuations in n_{ref} by increasing the sampling rate of the PBH flux as it evaporates. That is, the flux reported in Fig. 3.9 was recalculated with finer time bins, $(\tau_i,\ \tau_f)$, as the PBH evaporated. For reference, τ is the time to evaporation as detailed in §3.3.

7.4 Results

I tested this analysis using a blinded technique, as per internal IceCube guidelines. The prescribed method of searching for time-dependent point sources has been previously applied to different datasets, notably, to reveal a flare from the blazar TXS 0506+056 [11]. The unblinding plan of this analysis was to search the northern celestial sky ($\delta > -5^\circ$) for time-dependent sources using the 8.7-year PS Tracks sample 5.3. Note that while this is a pre-curated, high-level sample, it is background-dominated with mostly atmospheric neutrinos, and is optimized for point-source searches (see §5.7.2 for more details about the sample). For each of the six search windows, $\Delta t \in \{11.57,\ 3.86,\ 1.29,\ 0.43,\ 0.14,\ 0.05\}$ days, I searched for an excess signal over the background using the method prescribed in the earlier sections. A pre-determined threshold for this search was set at 3σ (post-trial correction) after accounting for the look-elsewhere effect to define *null-detection*. Based on this pre-determined threshold, no signal excess was detected and this search is consistent with background expectations. In this section, I detail the procedure of unblinding the northern celestial sky using the time-dependent flare search algorithm described previously. The significance of null-detection will be discussed in the next section §7.5.

7.4.1 Skymaps

To apply the point-source search method, the northern celestial sky ($\delta > -5^\circ$) for the PS Tracks data sample was divided into equal area quadrilaterals using the `HEALPIX` algorithm, provided by `healpy` [130] [131]. The resolution of this division is expressed by a parameter called N_{side}, with the total number of pixels being: $n_{\text{pix}} = 12 \times N_{\text{side}}^2$. For

reference, the approximate resolution at $N_{\rm side} = 128$ is 0.46° (low-res) and at $N_{\rm side} = 512$ is 0.11° (high-res). For each pixel in the map created by this division and search window duration ($\Delta t \in \{11.57,\ 3.86,\ 1.29,\ 0.43,\ 0.14,\ 0.05\}$ days), the unbinned likelihood method was applied to yield 4 quantities of interest: TS, $\hat{n}$, $\hat{\gamma}$, $\hat{T}_0$ that corresponds to the test statistic, best-fit number of signal events, best-fit spectral index, and the best-fit time of PBH evaporation as described in §7.2.1.

For each pixel that was scanned by this method, the test statistic is converted to a *local* p-value. This conversion involves pre-computing $50,000$ background-only trials across various declinations in the northern celestial sky. The set of background-only trials extends the previous set used for sensitivity calculations. 50 declinations, including the 9 sampled for sensitivity, are used to generate a background map and are shown in Fig. 7.2. This map is then interpolated to convert the unblinded TS of each pixel into a local p-value. As this p-value does not account for the look-elsewhere effect (number of pixels scanned), smaller values are to be expected while performing this search over a large number of pixels. These skymaps, for each time window and $N_{\rm side} = 128$, are shown in Figures 7.7 - 7.12. For reference, the number of pixels scanned is $106,388$. Note that p-values shown in the figures are the pre-trial or local p-values, and are reported as $-\log_{10}(p)$ in the maps. A higher resolution scan of $n_{\rm side} = 512$ is also performed to verify that the observed fluctuations are consistent with background expectations.

7.4.2 Hotspots & trial correction

The most significant locations in each unblinded map are called *hotspots*. These are listed in Table 7.1, along with the best-fit parameters, TS, and local (pre-trial) p-values for $N_{\rm side} = 128,\ N_{\rm pix} \sim 10^5$. Firstly, we expect these local p-values to be uniformly distributed, between 0 and 1. That is the distribution of $\log_{10}(p)$ is expected to follow an exponential distribution, and this is shown in Fig. 7.13 using log-log scaling. Next, we can convert these local p-values to global p-values by accounting for the look-elsewhere effect. This is

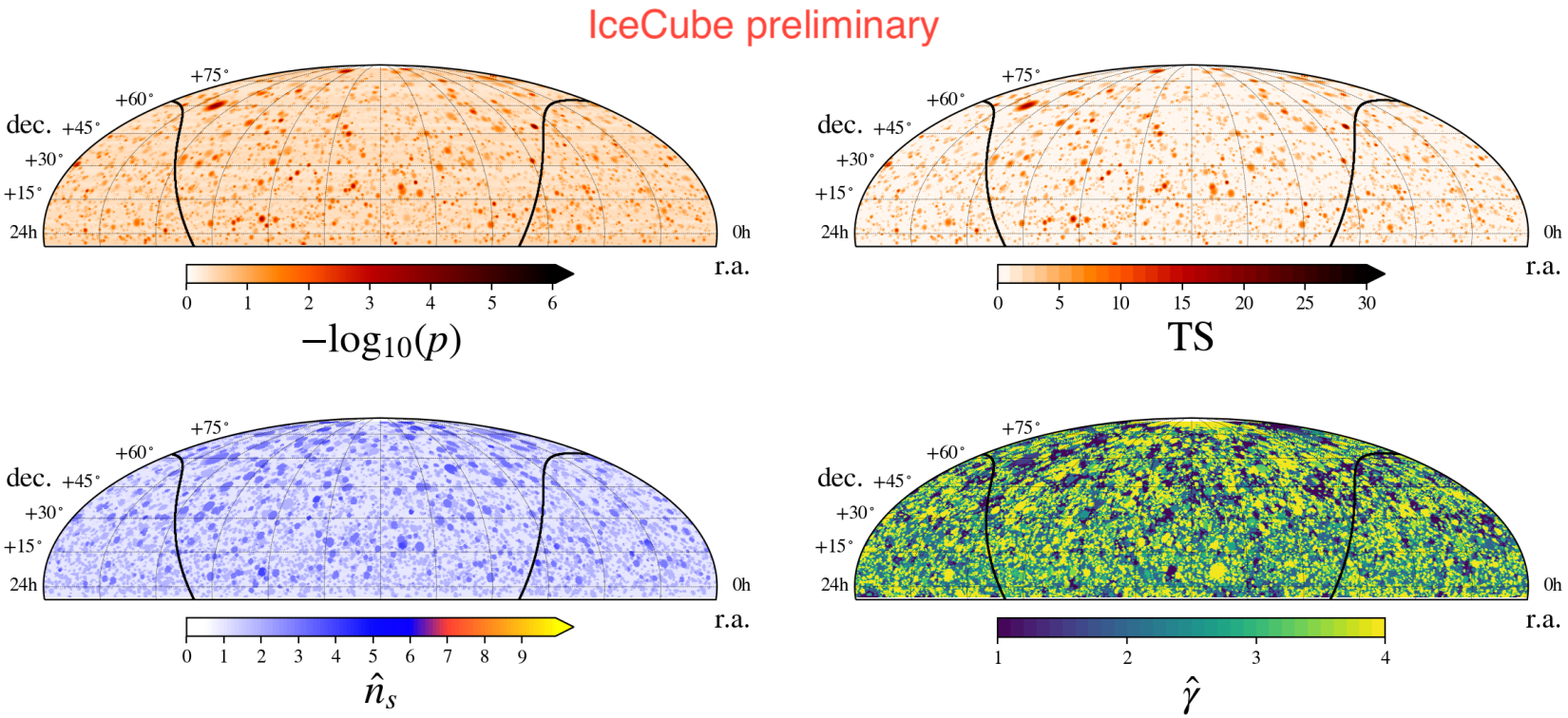

Figure 7.7: Skymap of the point-source search for a 0.05-day neutrino flare in the northern 8.7-year PS Tracks sample. No significant excess was found, see text for more details. I created this plot using `cartopy` and `matplotlib` in `PYTHON`.

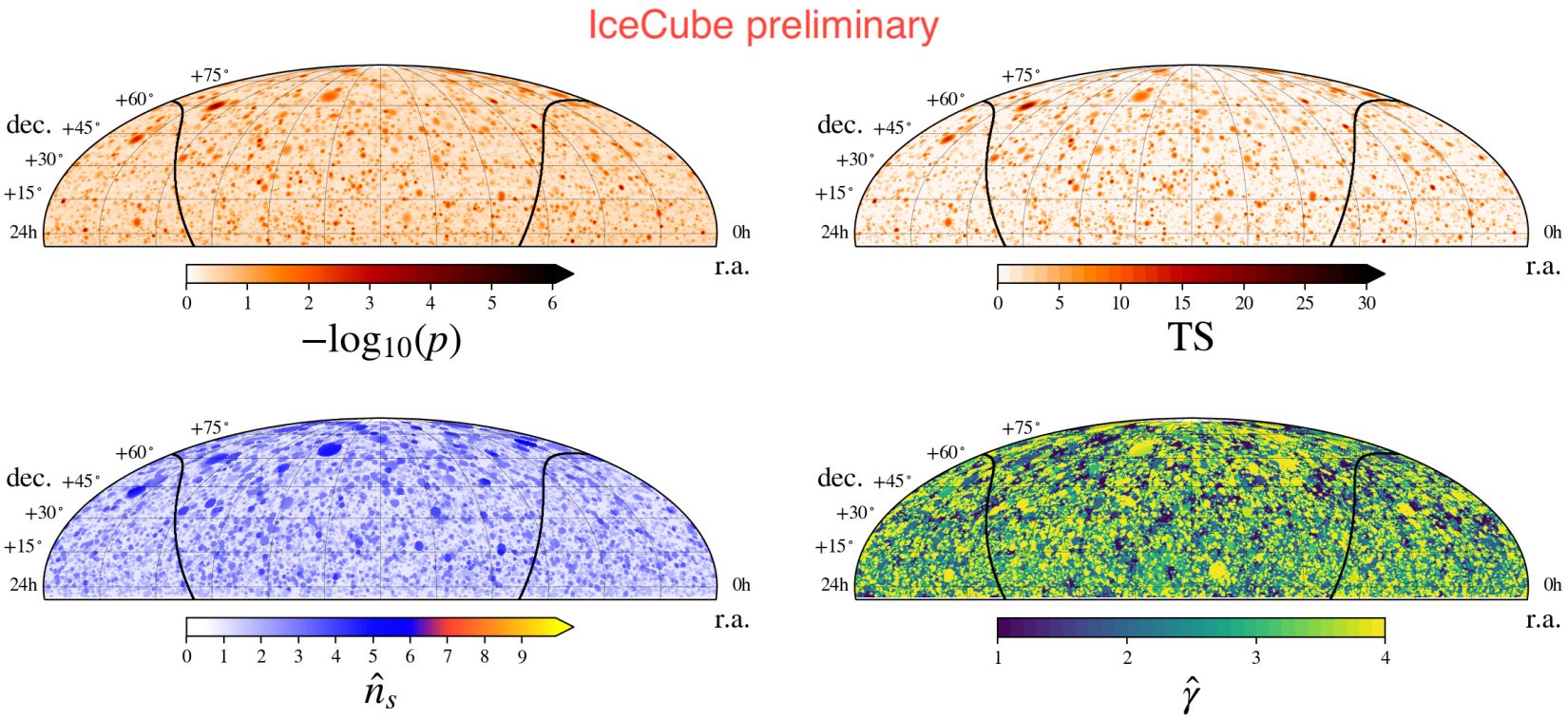

Figure 7.8: Skymap of the point-source search for a 0.14-day neutrino flare in the northern 8.7-year PS Tracks sample. No significant excess was found, see text for more details. I created this plot using `cartopy` and `matplotlib` in PYTHON.

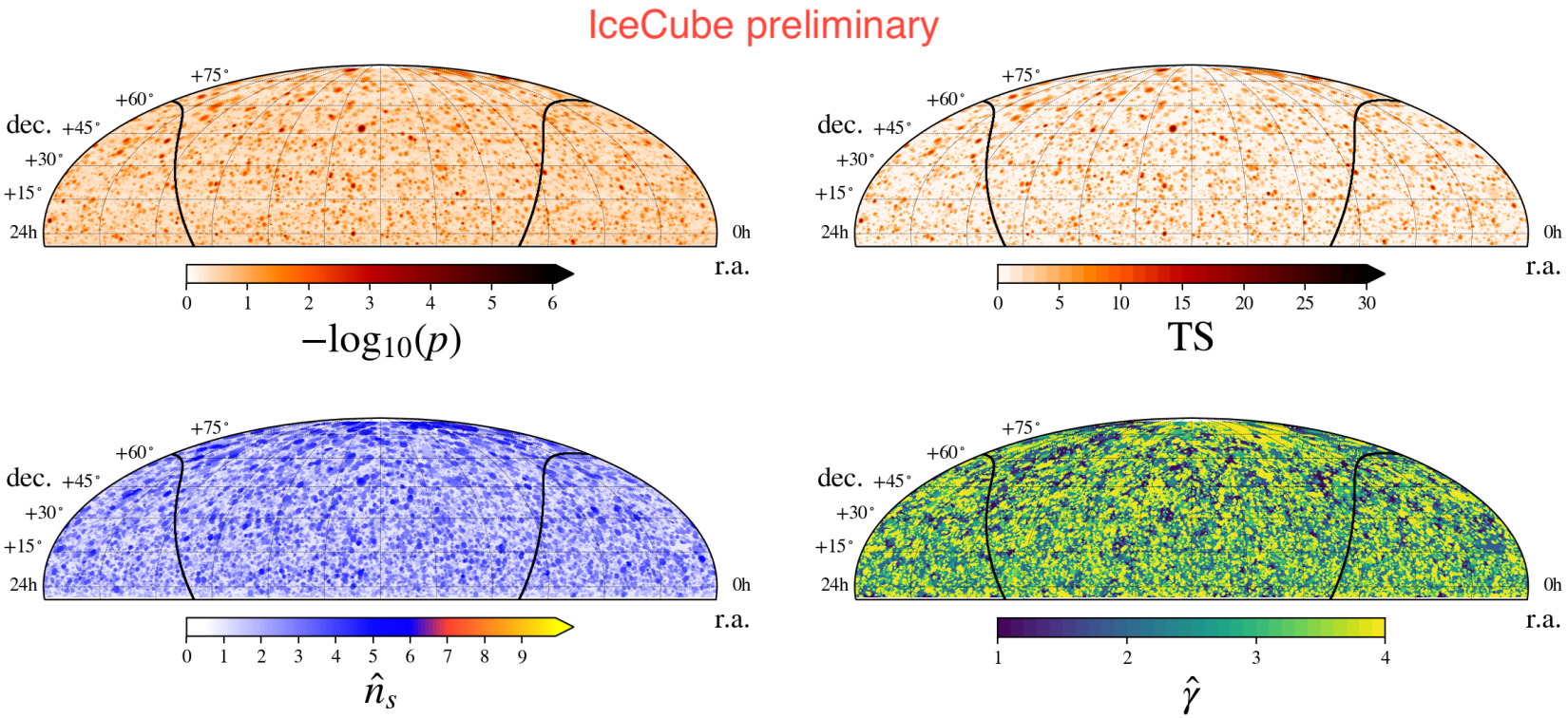

Figure 7.9: Skymap of the point-source search for a 0.43-day neutrino flare in the northern 8.7-year PS Tracks sample. No significant excess was found, see text for more details. I created this plot using `cartopy` and `matplotlib` in PYTHON.

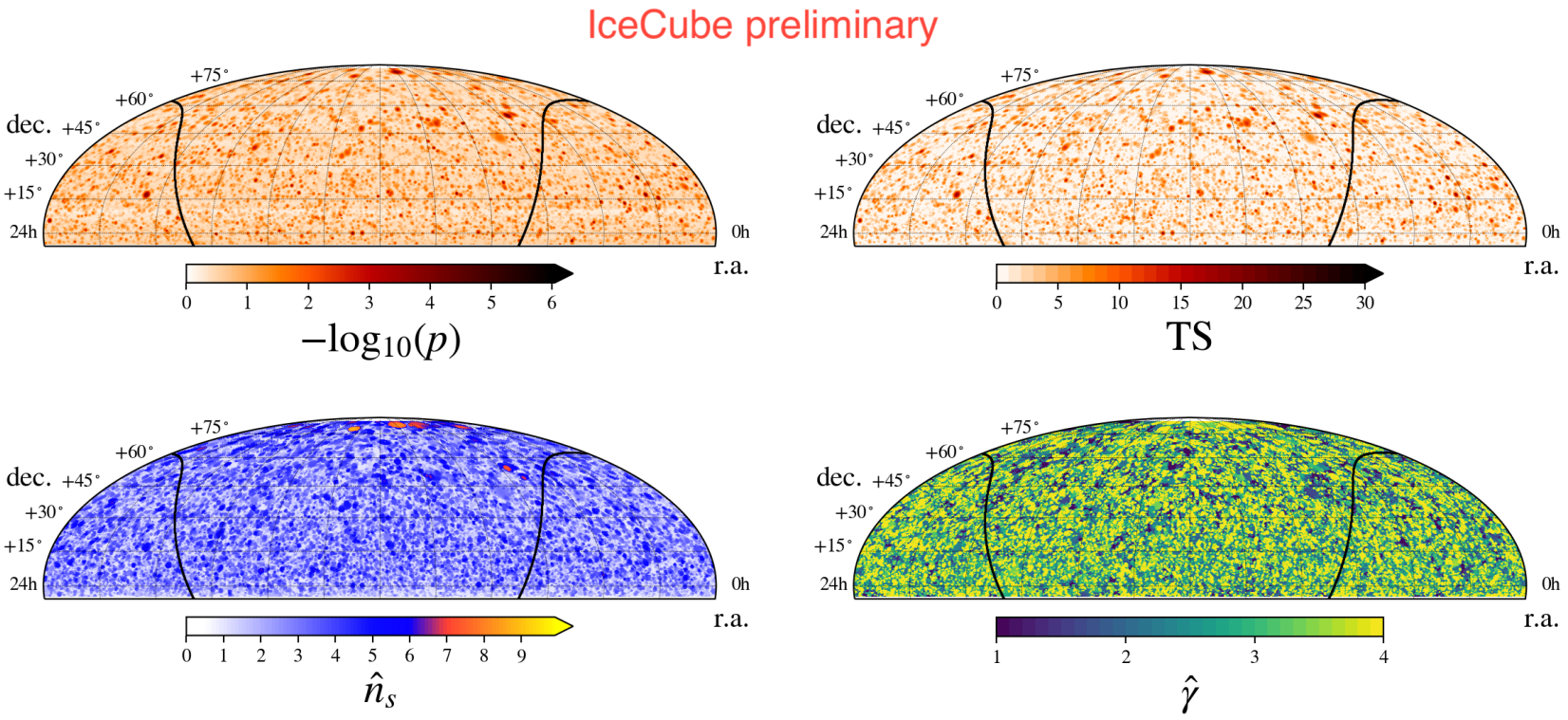

Figure 7.10: Skymap of the point-source search for a 1.29-day neutrino flare in the northern 8.7-year PS Tracks sample. No significant excess was found, see text for more details. I created this plot using `cartopy` and `matplotlib` in PYTHON.

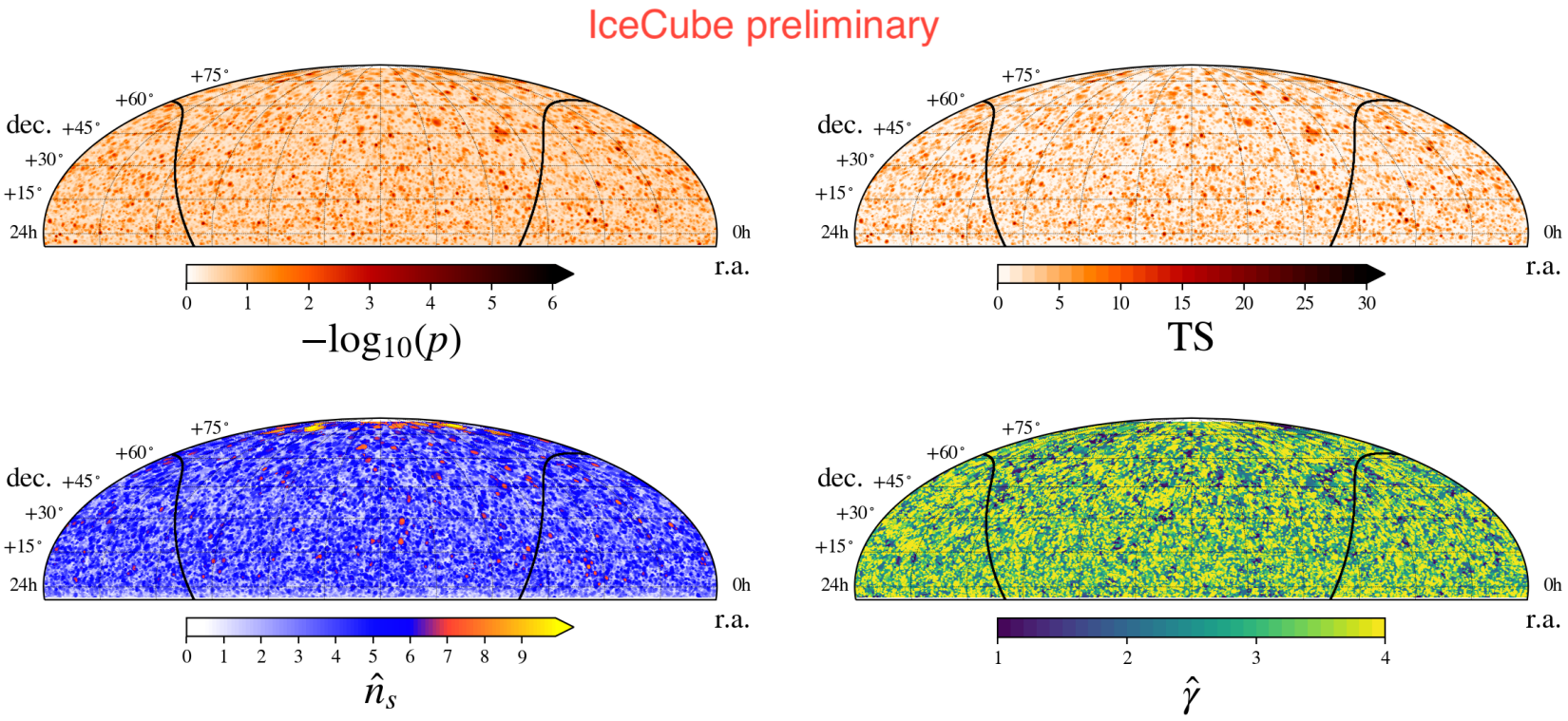

Figure 7.11: Skymap of the point-source search for a 3.86-day neutrino flare in the northern 8.7-year PS Tracks sample. No significant excess was found, see text for more details. I created this plot using `cartopy` and `matplotlib` in PYTHON.

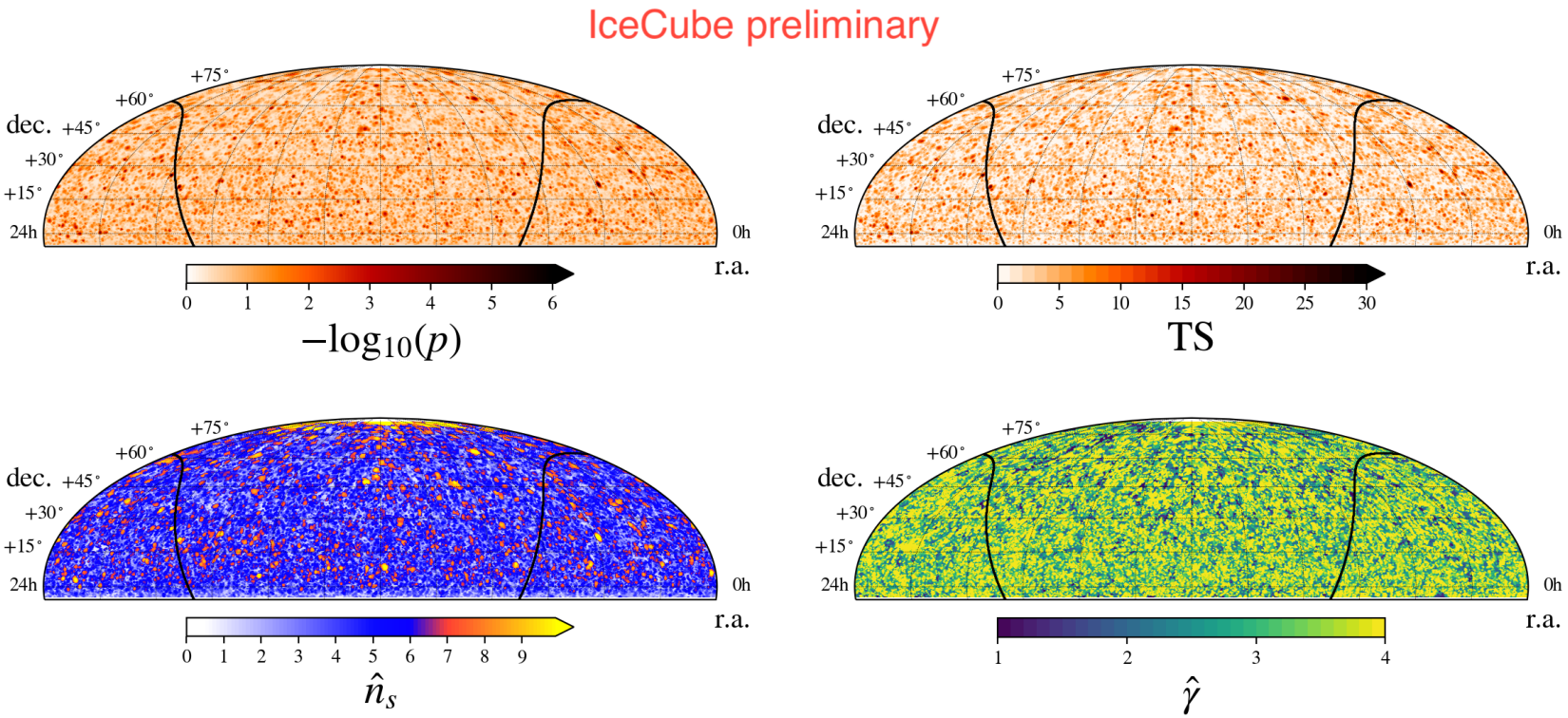

Figure 7.12: Skymap of the point-source search for an 11.57-day neutrino flare in the northern 8.7-year PS Tracks sample. No significant excess was found, see text for more details. I created this plot using `cartopy` and `matplotlib` in PYTHON.

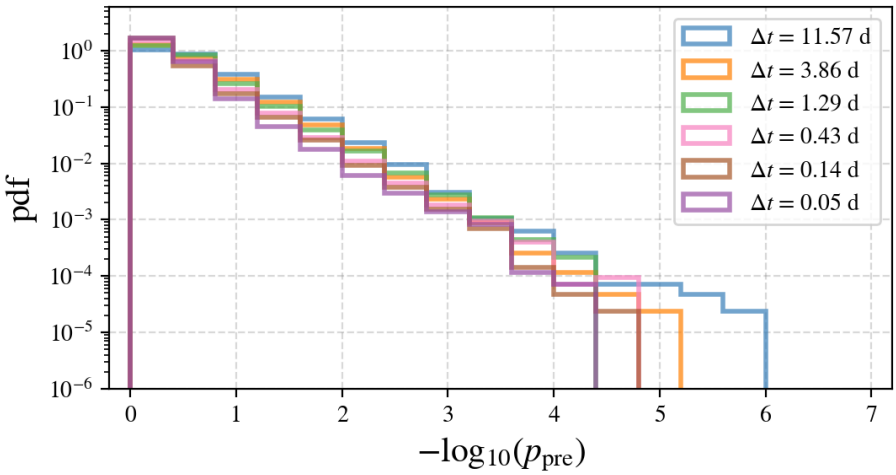

Figure 7.13: Distribution of local p-values from the time-dependent search for six search windows in the northern celestial sky for the 8.7-year PS Tracks sample. I created this plot using the `matplotlib` package in `PYTHON`.

done by using the blinded background-only TS map and generating multiple realizations such that only the most-significant p-values are picked for each search window. In this way, we can establish the distribution of local p-values expected from the background and use it to convert the observed local p-value into an estimate of the post-trial or global p-value. This is shown in Fig. 7.14. See that this correction does not take into account the number of search windows (Bonferroni correction), and the global p-values reported in Table 5.3 include this additional correction. As per the pre-determined threshold for this analysis, I conclude that these p-values are consistent with the background and that this search yields a null detection.

7.5 Limits & Discussion

As we previously saw, the results of this time-dependent point-source search yielded a null detection for each search window ($\Delta t \in \{11.57,\ 3.86,\ 1.29,\ 0.43,\ 0.14,\ 0.05\}$ days). This allows for the conversion of the sensitivity distance, calculated in §7.3.2, into an upper limit on PBH evaporation in our local universe. Before we move on to interpreting the results of the study presented in this dissertation, it is important to review existing bounds by various

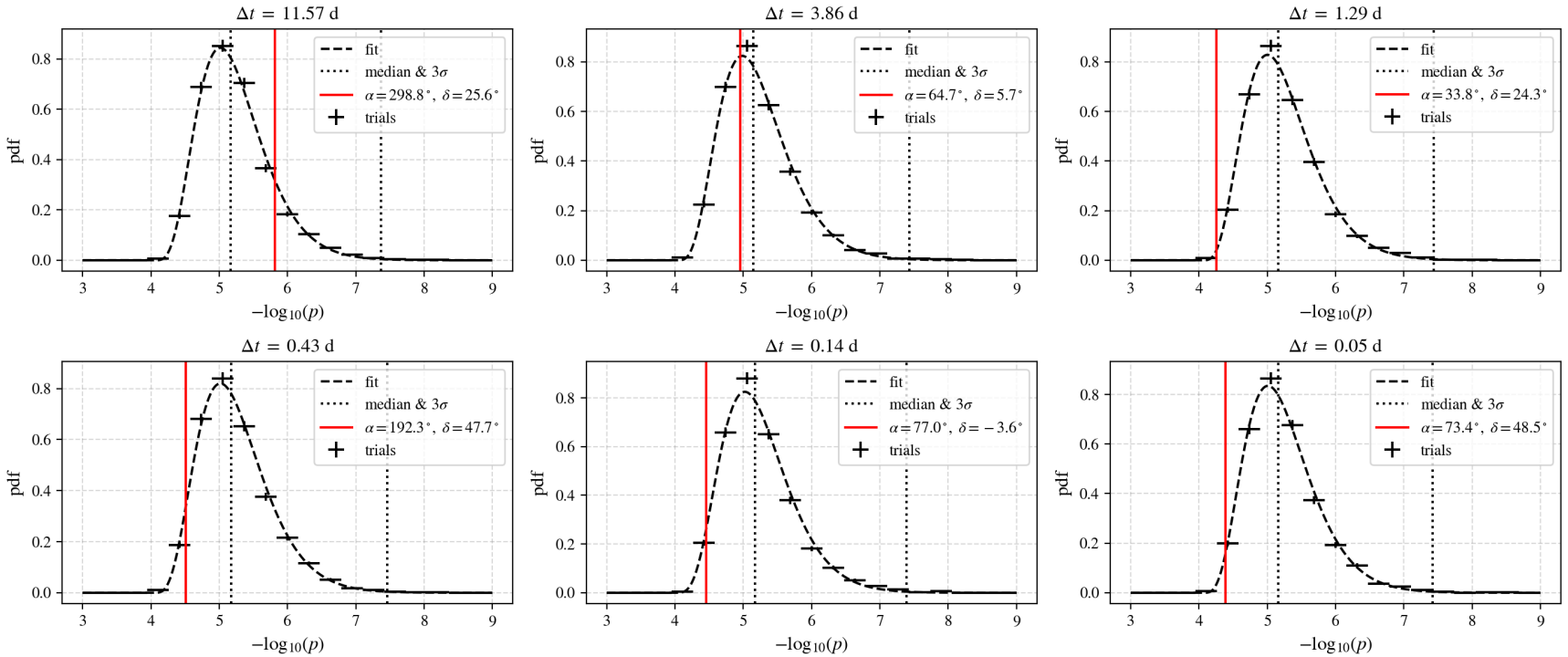

Figure 7.14: Trial correction applied to each search window for $N_{\text{pix}} \sim 10^5$, that results in the hottest spot for the 11.57-day search to be 1.1 σ before the Bonferroni correction for the six searches. The hottest spot from each search is shown by the vertical red line, while the dashed black lines correspond to the median and 3σ. As per the pre-determined threshold for this search, this significance is consistent with background expectations. I created this plot using the `matplotlib` package in `PYTHON`.

Table 7.1: Most significant locations in the northern celestial sky for each search window (Δt) in the 8.7-year PS Tracks sample, using `healpy`'s $N_{\text{side}} = 128$ division, taken from figures 7.7 - 7.12. For each location, the celestial coordinates (in degrees), best-fit parameters of the unbinned likelihood method, and the corresponding local (pre) and global (post) p-values are provided. These results are consistent with background expectations, see text for more details.

Δt **(days)**	**R.A.** (°)	**Dec** (°)	$\hat{T}_0$ **(UTC)**	$\hat{n}_s$	$\hat{\gamma}$	**TS**	$-\log_{10}(p_{\text{pre}})$	p_{post}
11.57	298.83	25.61	2015-12-27	10.10	4.00	28.14	5.82	0.78
3.86	64.69	5.68	2012-12-25	7.59	2.62	24.24	4.96	1.0
1.29	33.75	24.30	2015-12-07	5.41	4.00	19.96	4.26	1.0
0.43	192.35	47.75	2014-02-24	4.86	2.40	21.14	4.51	1.0
0.14	76.99	-3.58	2015-01-14	3.00	4.00	19.97	4.46	1.0
0.05	73.38	48.53	2012-04-03	3.00	4.00	21.15	4.39	1.0

experiments on PBHs. Firstly, PBHs that have not fully evaporated yet due to Hawking radiation, have been considered to be dark matter (DM) candidates [18]. This is because BHs that arise from the early universe are not limited by the mass or population constraints that distinguish BHs of stellar origin. Therefore, these holes of primordial origin satisfy the fundamental requirements for being DM, without the requirement of postulating additional particle types. Moreover, while their precise mass is uncertain, on a cosmological level, primordial black holes (PBHs) would act similarly to conventional cold DM particles. Over the years, several formation mechanisms have been proposed for PBHs and are reviewed recently here [132]. Due to the size of the possible ranges of PBHs over orders of magnitude in mass, our current understanding comes from limits that can be broadly categorized by mass as shown in Fig. 7.15:

- Evaporation: PBHs with initial masses of $\sim 5 \times 10^{14}$ g should be fully evaporating in the present universe with bursts of high-energy particles due to Hawking radiation
- Microlensing: For a given PBH mass, and the known galactic DM mass distribution, gravitational lensing of light around a PBH should be observable
- Gravitational Waves: LIGO, the current standard on GW detection, would observe a higher merger rate if PBHs are DM

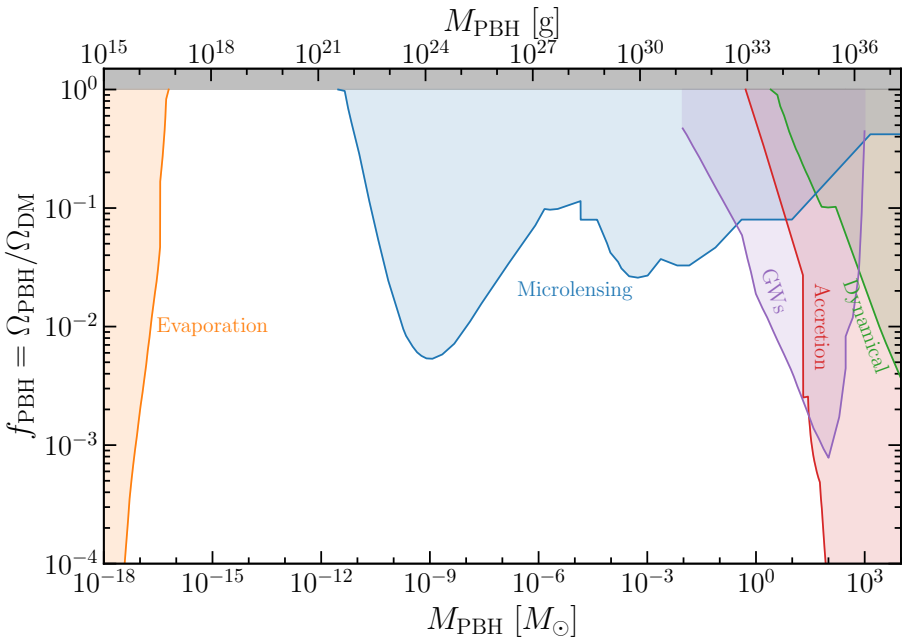

Figure 7.15: Existing bounds on the allowable mass range for monochromatic PBHs (identical mass distribution), as a fraction of dark matter. Figure reproduced from [133] that uses an online repository of existing bounds [134].

- Accretion: Radio and X-ray measurements would observe the accretion of gas from the interstellar medium onto PBHs

- Dynamical: Upper bounds from searches for massive compact halo objects (MACHOs)

The age of the universe sets the strongest constraint on the PBH mass, as they cannot be DM if they do not exist. If PBHs managed to endure until the present day, they would emit a considerable amount of Hawking radiation. The current limits in the $10^{15} - 10^{17}$ g mass range come from the absence of bumps in the extragalactic background (EGB) light observations, if all of PBHs are DM. These constraints are powerful but do not test the local DM density but rather its average extragalactic distribution. In this range $\lesssim 10^{15}$ g there are also limits derived from the galactic γ-ray background (GGB). My work, presented in this dissertation is a contribution to the constraining PBHs below 10^{15} g. Additionally, PBHs in this mass range would emit sub-GeV $e^{\pm}$ pairs in our galaxy that would be observable

by Voyager I. So there are strong constraints on evaporating PBHs that can contribute to DM shown by the orange region in Fig. 7.15. These constitute the constraints on *diffuse* emission from evaporating PBHs in our local universe, that can contribute to dark matter. Searches for *individual* PBH bursts[13] are a different matter. The verification of a PBH burst goes beyond merely confirming their existence and enables the calculation of their relic density and burst rate density. Such a confirmation would offer crucial insights into various fields of physics, such as the fundamental processes that occurred in the early Universe and particle physics at energies that are currently unattainable by terrestrial accelerators. Conversely, the absence of PBH burst occurrences in focused searches would provide significant limitations on the early Universe.

7.5.1 Burst rate upper limits

The current best limits on the local PBH evaporation rate (burst-rate) density at the 99% confidence level are by the HAWC collaboration at $3400\ \mathrm{pc}^{-3}\ \mathrm{yr}^{-1}$, using 959 days of HAWC data and a search duration of 10 seconds. See Table 7.2 for existing limits by various γ-ray experiments. The study presented in this dissertation is the first time high-energy neutrinos are used to search for an individual PBH burst. We can easily translate d_{sens} calculated in 7.3.2 into an effective sensitivity volume by integrating over the northern celestial sky using:

$$V_{\mathrm{sens}} = \sum_{\delta_i} \frac{2\pi}{3} \cdot d^3_{\mathrm{sens}}(\delta_i) \cdot \Delta(\sin\delta) \tag{7.6}$$

This in turn allows us to calculate the burst rate upper limit by considering Poisson fluctuations and the livetime of this search which is 8.7 years:

[13] Or explosions as Hawking initially proposed

Experiment	Burst Rate Upper Limit	Search Duration	Reference
Whipple	1080000 $\mathrm{pc}^{-3}\mathrm{yr}^{-1}$	5 s	[136]
CYGNUS	850000 $\mathrm{pc}^{-3}\mathrm{yr}^{-1}$	1 s	[137]
Tibet	460000 $\mathrm{pc}^{-3}\mathrm{yr}^{-1}$	1 s	[138]
IceCube	170342 $\mathrm{pc}^{-3}\mathrm{yr}^{-1}$	3.7×10^4 s	this work
Milagro	36000 $\mathrm{pc}^{-3}\mathrm{yr}^{-1}$	1 s	[50]
VERITAS	22200 $\mathrm{pc}^{-3}\mathrm{yr}^{-1}$	30 s	[139]
H.E.S.S.	14000 $\mathrm{pc}^{-3}\mathrm{yr}^{-1}$	30 s	[52]
Fermi-LAT	7200 $\mathrm{pc}^{-3}\mathrm{yr}^{-1}$	1.26×10^8 s	[49]
HAWC 3 yr.	3400 $\mathrm{pc}^{-3}\mathrm{yr}^{-1}$	10 s	[19]

Table 7.2: The strongest limits on the burst rate density of individual PBHs in our local universe by various γ-ray detectors and IceCube Neutrino Observatory at the 99% confidence level, including the best limit by HAWC [19].

$$UL^{\nu}_{99} \leq \frac{4.6}{V_{\mathrm{sens,\ 99\%}} \cdot \mathrm{livetime}} = 17.0342^{+1.0003}_{-0.6408} \times 10^4\ \mathrm{pc}^{-3}\ \mathrm{yr}^{-1}, \tag{7.7}$$

where $4.6 = -\log(1 - 0.99)$ is the 99% Neyman upper limit for observing zero PBH bursts in neutrinos. This burst-rate upper limit of $170,342\ \mathrm{pc}^{-3}\ \mathrm{yr}^{-1}$ uses $\alpha = 5\sigma,\ \beta = 0.99$ for calculating n_{sens}, and a search duration of 0.43 days. By changing the required statistical threshold on n_{sens}, we can see the behavior of this sensitivity across the six search windows selected in this analysis in Fig. 7.16. The bands provided represent the statistical uncertainty in estimating n_{sens}, and the number reported in Table 7.2 is the best time window for the top of the band as a pessimistic choice. Future telescopes such as the Southern Wide field of view Gamma-ray Observatory (SWGO) would further push the detectable volume and therefore the best limits, with an estimated $\lesssim 10^3\ \mathrm{pc}^{-3}\ \mathrm{yr}^{-1}$ within one year of operation for the $1 - 10$ second search window [135].

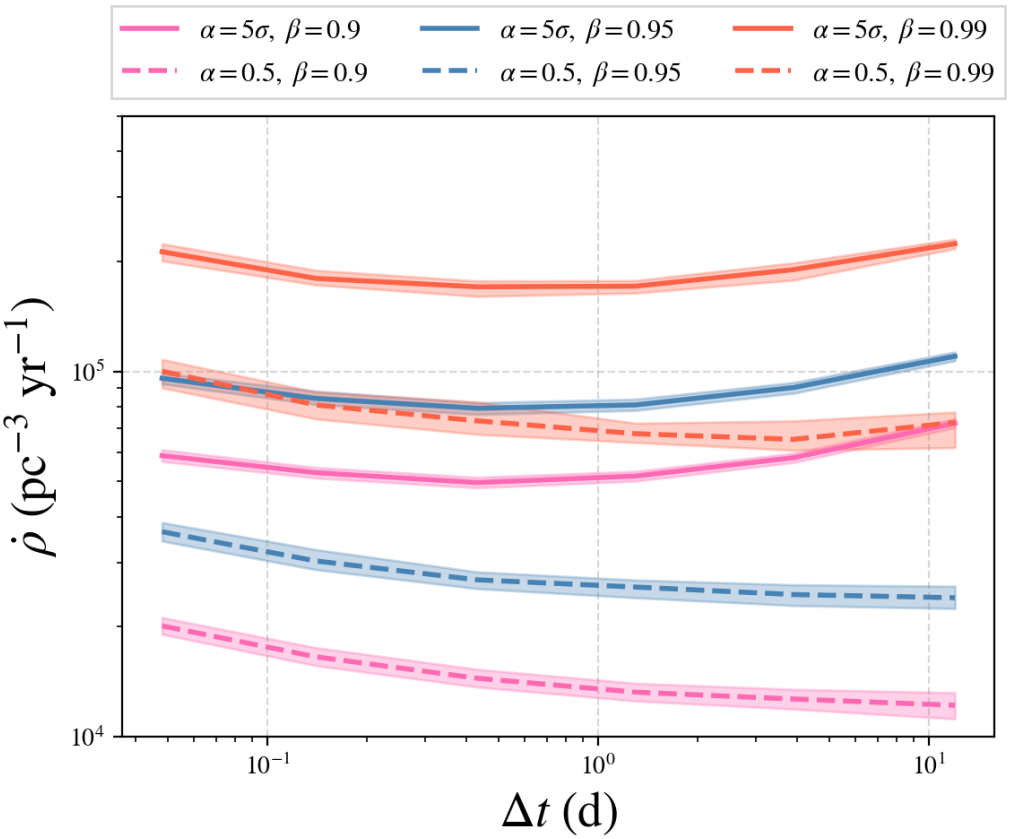

Figure 7.16: IceCube's sensitivity to PBH burst-rate in our local universe, using the six search windows evaluated by the 8.7-year PS Tracks sample. Various statistical thresholds are provided for reference, along with the one used by the community of $\alpha = 5\sigma,\ \beta = 0.99$ that corresponds to a 5σ detection with 99% background rejection. I created this plot using the `matplotlib` package in `PYTHON`.

CHAPTER 8
CONCLUSION & OUTLOOK

Neutrinos offer a distinct perspective into the high-energy, non-thermal universe by enabling the identification of their source, unlike cosmic rays. Furthermore, they offer valuable insights into the optically thick surroundings of cosmic accelerators. For instance, the observation of 19 neutrinos from the galactic supernova, SN 1987A, demonstrated the existence of a proto-neutron star [9]. The recent evidence of TeV neutrino emission [2] from the nearby Seyfert II galaxy and Active Galactic Nuclei (AGN) NGC 1068 points to γ-ray suppression in the disk-corona model of an AGN [13] [14] [15] [46]. AGNs are known to be variable across all wavelengths, but what about neutrinos? In order to answer this question, I developed the time-variability test, `TAUNTON` , as described in this dissertation. This test is a single hypothesis test that confirms or rejects the steady source hypothesis for current and future neutrino source candidates, based on a pre-defined threshold. The purpose of this test is to characterize current and future neutrino sources into steady and time-variable neutrino sources. This allows for additional constraints to be placed on models describing these cosmic accelerators. For instance, neutrino production in NGC 1068 should consistently occur over the 8.7 years of observation time, and consequently so should cosmic-ray acceleration.

Hawking radiation is perhaps the most interesting and untested prediction regarding black holes, as it elegantly unifies general relativity and quantum field theory for a single physical process. A consequence of this prediction, made in 1974 by Stephen Hawking [17], is that holes formed in the early universe with a mass $\lesssim 10^{15}\ \mathrm{g}$ would evaporate today after losing mass over the age of the universe. These holes, commonly referred to as primordial black holes (PBHs), offer a direct test of Hawking radiation as they inch closer to evaporation due to the energetics of the radiation as well as the accelerating mass loss.

While PBHs have been considered to be dark matter (DM) candidates and have been of interest over the past 45 years, it has proven difficult to explain the abundance of DM solely with PBHs. Additionally, modern detectors have made it possible to search for an *individual* PBH evaporation event in our local ($\lesssim 0.01$ pc) universe to further constrain their existence. High-energy neutrinos, along with γ-rays are expected from Hawking radiation of an evaporating PBH, and I present a search for these evaporation events using IceCube data in this dissertation. The results of this search are interpreted as null-detection of PBHs in the detectable volume around the Earth. Consequently, an upper limit on the rate density of PBH evaporation events using high-energy neutrinos is placed at 170,342 $\mathrm{pc}^{-3}\ \mathrm{yr}^{-1}$ for a search duration of 0.43 days. This adds to limits placed by the γ-ray detectors over the years, as we continue to search for PBHs.

In terms of neutrino astronomy, with the identification of NGC 1068 and TXS 0506+056 as candidate neutrino sources, we take a step closer to understanding the specific sites of cosmic-ray acceleration and contributions to the high-energy diffuse flux observed by IceCube since 2013 [1]. This indicates that there are at least two populations of neutrino sources that differ in both density and luminosity by orders of magnitude and that we do not know much about neutrino emission from these sources. Upcoming cubic kilometer-sized detectors such as Baikal-GVD, KM3NeT, and P-ONE, will be able to add to our knowledge about the high-energy neutrino sky [140, 77, 80]. In particular, as these detectors are located in the northern hemisphere, they would be more sensitive to the southern celestial sky that is dominated by down-going atmospheric muon background for IceCube. That is, galactic neutrino sources, such as Sagittarius A*, could be visible in the high-energy neutrino sky in the near future. Additional detectors also offer increased opportunities for detecting neutrino sources due to coincident searches, similar to searches from an alert event observed by IceCube [10]. In the future, the methods presented in this dissertation can be readily applied to muon neutrino data collected by IceCube as well as by these upcoming detectors. Perhaps we will confirm Hawking radiation, or confirm that the region

near the BH at the center of our own galaxy is also a steady neutrino source!

REFERENCES

[1] IceCube Collaboration, "Evidence for High-Energy Extraterrestrial Neutrinos at the IceCube Detector," *Science*, vol. 342, no. 6161, 2013.

[2] IceCube Collaboration *et al.*, "Evidence for neutrino emission from the nearby active galaxy NGC 1068," *Science*, vol. 378, no. 6619, 2022.

[3] Pierre Auger Collaboration *et al.*, "Observation of a large-scale anisotropy in the arrival directions of cosmic rays above 8×10^{18} eV," *Science*, vol. 357, no. 6357, 2017.

[4] B. P. Abbott *et al.*, "Observation of gravitational waves from a binary black hole merger," *Phys. Rev. Lett.*, vol. 116, 6 2016.

[5] B. P. Abbott *et al.*, "Multi-messenger Observations of a Binary Neutron Star Merger," *The Astrophysical Journal Letters*, vol. 848, no. 2, 2017.

[6] K. Hirata *et al.*, "Observation of a neutrino burst from the supernova SN1987A," *PRL*, vol. 58, no. 14, 1987.

[7] R. M. Bionta *et al.*, "Observation of a neutrino burst in coincidence with supernova 1987A in the Large Magellanic Cloud," *PRL*, vol. 58, no. 14, 1987.

[8] K. Scholberg, "Supernova neutrino detection," *Annual Review of Nuclear and Particle Science*, vol. 62, no. 1, 2012.

[9] J. M. Lattimer and A. Yahil, "Analysis of the Neutrino Events from Supernova 1987A," *The Astrophysical Journal*, vol. 340, 1989.

[10] IceCube Collaboration *et al.*, "Multimessenger observations of a flaring blazar coincident with high-energy neutrino IceCube-170922A," *Science*, vol. 361, no. 6398, 2018.

[11] IceCube Collaboration *et al.*, "Neutrino emission from the direction of the blazar TXS 0506+056 prior to the IceCube-170922A alert," *Science*, vol. 361, no. 6398, 2018.

[12] F. Halzen, A. Kheirandish, T. Weisgarber, and S. P. Wakely, "On the neutrino flares from the direction of TXS 0506+056," *The Astrophysical Journal*, vol. 874, no. 1, 2019.

[13] E. P. T. Liang, "On the hard X-ray emission mechanism of active galactic nuclei sources.," *The Astrophysical Journal*, vol. 231, 1979.

[14] F. Haardt and L. Maraschi, "A Two-Phase Model for the X-Ray Emission from Seyfert Galaxies," *The Astrophysical Journal Letters*, vol. 380, 1991.

[15] F. Haardt and L. Maraschi, "X-Ray Spectra from Two-Phase Accretion Disks," *The Astrophysical Journal*, vol. 413, 1993.

[16] D. R. Wilkins and L. C. Gallo, "The Comptonization of accretion disc X-ray emission: consequences for X-ray reflection and the geometry of AGN coronae," *Monthly Notices of the Royal Astronomical Society*, vol. 448, no. 1, 2015.

[17] S. W. Hawking, "Black hole explosions?" *Nature*, vol. 248, no. 5443, 1974.

[18] B. Carr and J. Silk, "Primordial black holes as generators of cosmic structures," *Monthly Notices of the Royal Astronomical Society*, vol. 478, no. 3, 2018.

[19] A. Albert *et al.*, "Constraining the local burst rate density of primordial black holes with hawc," *Journal of Cosmology and Astroparticle Physics*, vol. 2020, no. 04, 2020.

[20] V. Hess, "On the Observations of the Penetrating Radiation during Seven Balloon Flights," *arXiv e-prints*, 2018.

[21] C. Evoli, *The cosmic-ray energy spectrum*, Accessed: 2023-03-14. [Online]. Available: `https://doi.org/10.5281/zenodo.4309926`.

[22] B. Peters, "Primary cosmic radiation and extensive air showers," *Il Nuovo Cimento*, vol. 22, no. 4, 1961.

[23] A. De Angelis and M. Pimenta, *Introduction to Particle and Astroparticle Physics*. 2018.

[24] E. Fermi, "On the origin of the cosmic radiation," *Phys. Rev.*, vol. 75, 8 1949.

[25] M. S. Longair, *High energy astrophysics: Stars, the galaxy and the interstellar medium*. 1994, vol. 2.

[26] M Bustamante *et al.*, "High-energy cosmic-ray acceleration," 2010.

[27] T. K. Gaisser, R. Engel, and E. Resconi, *Cosmic Rays and Particle Physics*. 2016.

[28] A. R. Bell, "The acceleration of cosmic rays in shock fronts - I.," *Monthly Notices of the Royal Astronomical Society*, vol. 182, 1978.

[29] ——, "The acceleration of cosmic rays in shock fronts - II.," *Monthly Notices of the Royal Astronomical Society*, vol. 182, 1978.

[30] C. Adler *et al.*, "Kaon production and kaon to pion ratio in Au + Au collisions at s_{NN}=130 GeV," *Physics Letters B*, vol. 595, no. 1-4, 2004.

[31] T. Kashti and E. Waxman, "Astrophysical Neutrinos: Flavor Ratios Depend on Energy," *PRL*, vol. 95, no. 18, 2005.

[32] P. Lipari, "Lepton spectra in the earth's atmosphere," *Astroparticle Physics*, vol. 1, no. 2, 1993.

[33] E. Zas, F. Halzen, and R. Vázquez, "High energy neutrino astronomy: Horizontal air shower arrays versus underground detectors," *Astroparticle Physics*, vol. 1, no. 3, 1993.

[34] A. Schukraft, "A view of prompt atmospheric neutrinos with IceCube," *Nuclear Physics B Proceedings Supplements*, vol. 237, 2013.

[35] E. Richard *et al.*, "Measurements of the atmospheric neutrino flux by super-kamiokande: Energy spectra, geomagnetic effects, and solar modulation," *Physical Review D*, vol. 94, no. 5, 2016.

[36] G. Bellini *et al.*, "First Evidence of pep Solar Neutrinos by Direct Detection in Borexino," *PRL*, vol. 108, no. 5, 2012.

[37] E. F. Brown, A. Cumming, F. J. Fattoyev, C. J. Horowitz, D. Page, and S. Reddy, "Rapid Neutrino Cooling in the Neutron Star MXB 1659-29," *PRL*, vol. 120, no. 18, 2018.

[38] A. V. Sweigart and P. G. Gross, "Evolutionary sequences for red giant stars.," *The Astrophysical Journal Supplement Series*, vol. 36, 1978.

[39] Planck Collaboration *et al.*, "Planck 2018 results. VI. Cosmological parameters," *AAP*, vol. 641, 2020.

[40] S. E. Woosley and T. A. Weaver, "The Evolution and Explosion of Massive Stars. II. Explosive Hydrodynamics and Nucleosynthesis," *The Astrophysical Journal Supplement Series*, vol. 101, 1995.

[41] E. Waxman and J. Bahcall, "High energy neutrinos from astrophysical sources: An upper bound," *PRD*, vol. 59, no. 2, 1998.

[42] M. G. Aartsen *et al.*, "Observation of High-Energy Astrophysical Neutrinos in Three Years of IceCube Data," *PRL*, vol. 113, no. 10, 2014.

[43] G. Jungman, M. Kamionkowski, and K. Griest, "Supersymmetric dark matter," *Phys. Rep.*, vol. 267, 1996.

[44] P. Padovani *et al.*, "Active galactic nuclei: what's in a name?" *Astronomy & Astrophysics Review*, vol. 25, no. 1, 2017.

[45] Y. Inoue, D. Khangulyan, S. Inoue, and A. Doi, "On high-energy particles in accretion disk coronae of supermassive black holes: Implications for MeV gamma-rays and high-energy neutrinos from AGN cores," *The Astrophysical Journal*, vol. 880, no. 1, 2019.

[46] K. Murase, S. S. Kimura, and P. Mé száros, "Hidden cores of active galactic nuclei as the origin of medium-energy neutrinos: Critical tests with the MeV gamma-ray connection," *Physical Review Letters*, vol. 125, no. 1, 2020.

[47] C. W. Misner, K. S. Thorne, and J. A. Wheeler, *Gravitation*. 1973.

[48] Event Horizon Telescope Collaboration *et al.*, "First M87 Event Horizon Telescope Results. I. The Shadow of the Supermassive Black Hole," *The Astrophysical Journal Letters*, vol. 875, no. 1, 2019.

[49] M. Ackermann *et al.*, "Search for Gamma-Ray Emission from Local Primordial Black Holes with the Fermi Large Area Telescope," *Astrophys. J.*, vol. 857, no. 1, 2018.

[50] A. A. Abdo *et al.*, "Milagro Limits and HAWC Sensitivity for the Rate-Density of Evaporating Primordial Black Holes," *Astropart. Phys.*, vol. 64, 2015.

[51] G. T. and, "Searching for primordial black holes with the VERITAS gamma-ray experiment," *Journal of Physics: Conference Series*, vol. 375, no. 5, 2012.

[52] J.-F. Glicenstein, A. Barnacka, M. Vivier, T. Herr, and for the H. E. S. S. Collaboration, "Limits on Primordial Black Hole evaporation with the H.E.S.S. array of Cherenkov telescopes," *arXiv e-prints*, 2013.

[53] J. H. MacGibbon and B. J. Carr, "Cosmic Rays from Primordial Black Holes," *The Astrophysical Journal*, vol. 371, 1991.

[54] F. Halzen, B. Keszthelyi, and E. Zas, "Neutrinos from primordial black holes," *PRD*, vol. 52, no. 6, 1995.

[55] D. N. Page, "Particle emission rates from a black hole. II. Massless particles from a rotating hole," *PRD*, vol. 14, no. 12, 1976.

[56] ——, "Particle emission rates from a black hole. III. Charged leptons from a non-rotating hole," *PRD*, vol. 16, no. 8, 1977.

[57] A. Arbey and J. Auffinger, "BlackHawk: a public code for calculating the Hawking evaporation spectra of any black hole distribution," *European Physical Journal C*, vol. 79, no. 8, 2019.

[58] ——, "Physics beyond the standard model with BlackHawk v2.0," *European Physical Journal C*, vol. 81, no. 10, 2021.

[59] C. W. Bauer, N. L. Rodd, and B. R. Webber, "Dark matter spectra from the electroweak to the Planck scale," *Journal of High Energy Physics*, vol. 2021, no. 6, 2021.

[60] I. Esteban, M. C. Gonzalez-Garcia, M. Maltoni, T. Schwetz, and A. Zhou, "The fate of hints: updated global analysis of three-flavor neutrino oscillations," *Journal of High Energy Physics*, vol. 2020, no. 9, 2020.

[61] L. M. Brown, "The idea of the neutrino," *Physics Today*, vol. 31, no. 9, 1978.

[62] J. Cowan C. L., F. Reines, F. B. Harrison, H. W. Kruse, and A. D. McGuire, "Detection of the Free Neutrino: A Confirmation," *Science*, vol. 124, no. 3212, 1956.

[63] G. Danby *et al.*, "Observation of High-Energy Neutrino Reactions and the Existence of Two Kinds of Neutrinos," *PRL*, vol. 9, no. 1, 1962.

[64] R. Davis, D. S. Harmer, and K. C. Hoffman, "Search for Neutrinos from the Sun," *PRL*, vol. 20, no. 21, 1968.

[65] J. N. Bahcall, N. A. Bahcall, and G. Shaviv, "Present Status of the Theoretical Predictions for the ^{36}Cl Solar-Neutrino Experiment," *PRL*, vol. 20, no. 21, 1968.

[66] Particle Data Group *et al.*, "Review of Particle Physics," *Progress of Theoretical and Experimental Physics*, vol. 2020, no. 8, 2020.

[67] Y. Fukuda *et al.*, "Evidence for Oscillation of Atmospheric Neutrinos," *PRL*, vol. 81, no. 8, 1998.

[68] F. Suekane, *Neutrino Oscillations*. 2015, vol. 898.

[69] M. Katrin Collaboration Aker *et al.*, "Direct neutrino-mass measurement with sub-electronvolt sensitivity," *Nature Physics*, vol. 18, no. 2, 2022.

[70] K. N. Abazajian *et al.*, "Light Sterile Neutrinos: A White Paper," *arXiv e-prints*, 2012.

[71] M. G. Aartsen *et al.*, "eV-Scale Sterile Neutrino Search Using Eight Years of Atmospheric Muon Neutrino Data from the IceCube Neutrino Observatory," *PRL*, vol. 125, no. 14, 2020.

[72] S. L. Glashow, "Resonant Scattering of Antineutrinos," *Physical Review*, vol. 118, no. 1, 1960.

[73] M. G. IceCube Collaboration Aartsen *et al.*, "Detection of a particle shower at the Glashow resonance with IceCube," *Nature*, vol. 591, no. 7849, 2021.

[74] Y. Suwa *et al.*, "Observing Supernova Neutrino Light Curves with Super-Kamiokande. III. Extraction of Mass and Radius of Neutron Stars from Synthetic Data," *The Astrophysical Journal*, vol. 934, no. 1, 2022.

[75] J. Ahrens *et al.*, "Muon track reconstruction and data selection techniques in AMANDA," *Nuclear Instruments and Methods in Physics Research A*, vol. 524, no. 1-3, 2004.

[76] M. Ageron *et al.*, "ANTARES: The first undersea neutrino telescope," *Nuclear Instruments and Methods in Physics Research A*, vol. 656, no. 1, 2011.

[77] S. Aiello *et al.*, "Sensitivity of the KM3NeT/ARCA neutrino telescope to point-like neutrino sources," *Astroparticle Physics*, vol. 111, 2019.

[78] G. Safronov, *Baikal-gvd: Status and first results*, 2020.

[79] B. Collaboration *et al.*, *Diffuse neutrino flux measurements with the baikal-gvd neutrino telescope*, 2022.

[80] E. Resconi and P-ONE Collaboration, "The Pacific Ocean Neutrino Experiment," in *37th International Cosmic Ray Conference*, 2022.

[81] M. G. Aartsen *et al.*, "The IceCube Neutrino Observatory: instrumentation and online systems," *Journal of Instrumentation*, vol. 12, no. 3, 2017.

[82] S. L. Miller, "Clathrate Hydrates of Air in Antarctic Ice," *Science*, vol. 165, no. 3892, 1969.

[83] M. G. Aartsen *et al.*, "Efficient propagation of systematic uncertainties from calibration to analysis with the SnowStorm method in IceCube," *Journal of Cosmology and Astroparticle Physics*, vol. 2019, no. 10, 2019.

[84] G. Mie, "Beiträge zur Optik trüber Medien, speziell kolloidaler Metallösungen," *Annalen der Physik*, vol. 330, no. 3, 1908.

[85] M. G. Aartsen *et al.*, "Measurement of South Pole ice transparency with the IceCube LED calibration system," *Nuclear Instruments and Methods in Physics Research A*, vol. 711, 2013.

[86] "South Pole glacial climate reconstruction from multi-borehole laser particulate stratigraphy," *Journal of Glaciology*, vol. 59, no. 218, 2013.

[87] D. Chirkin, *In-ice systematics: Ice models*, Accessed: 2023-04-02. [Online]. Available: `https://events.icecube.wisc.edu/event/148/contributions/7833/`.

[88] M. Rongen, D. Chirkin, and IceCube Collaboration, "Advances in IceCube ice modelling & what to expect from the Upgrade," *Journal of Instrumentation*, vol. 16, no. 9, 2021.

[89] D. Chirkin and W. Rhode, "Propagating leptons through matter with Muon Monte Carlo (MMC)," *arXiv e-prints*, 2004.

[90] M. G. Aartsen *et al.*, "Energy reconstruction methods in the IceCube neutrino telescope," *Journal of Instrumentation*, vol. 9, no. 3, 2014.

[91] M. G. Aartsen *et al.*, "Flavor Ratio of Astrophysical Neutrinos above 35 TeV in IceCube," *PRL*, vol. 114, no. 17, 2015.

[92] R. Abbasi *et al.*, "Calibration and characterization of the IceCube photomultiplier tube," *Nuclear Instruments and Methods in Physics Research A*, vol. 618, no. 1-3, 2010.

[93] R. Abbasi *et al.*, "The IceCube data acquisition system: Signal capture, digitization, and timestamping," *Nuclear Instruments and Methods in Physics Research A*, vol. 601, no. 3, 2009.

[94] M. G. Aartsen *et al.*, "Improvement in fast particle track reconstruction with robust statistics," *Nuclear Instruments and Methods in Physics Research A*, vol. 736, 2014.

[95] N. van Eijndhoven, O. Fadiran, and G. Japaridze, "Implementation of a Gauss convoluted Pandel PDF for track reconstruction in neutrino telescopes," *Astroparticle Physics*, vol. 28, no. 4-5, 2007.

[96] N. Whitehorn, J. van Santen, and S. Lafebre, "Penalized splines for smooth representation of high-dimensional Monte Carlo datasets," *Computer Physics Communications*, vol. 184, no. 9, 2013.

[97] D. Heck, J. Knapp, J. N. Capdevielle, G. Schatz, and T. Thouw, *CORSIKA: a Monte Carlo code to simulate extensive air showers.* 1998.

[98] C. Andreopoulos *et al.*, "The GENIE Neutrino Monte Carlo Generator: Physics and User Manual," *arXiv e-prints*, 2015.

[99] A. Gazizov and M. Kowalski, "ANIS: High energy neutrino generator for neutrino telescopes," *Computer Physics Communications*, vol. 172, no. 3, 2005.

[100] A. M. Dziewonski and D. L. Anderson, "Preliminary reference Earth model," *Physics of the Earth and Planetary Interiors*, vol. 25, no. 4, 1981.

[101] D. Chirkin and W. Rhode, "Muon Monte Carlo: A High-precision tool for muon propagation through matter," 2004.

[102] H. Schwanekamp *et al.*, "Accelerating IceCube's Photon Propagation Code with CUDA," *Computing and Software for Big Science*, vol. 6, no. 1, 2022.

[103] D. Chirkin and IceCube Collaboration, "Photon tracking with GPUs in IceCube," *Nuclear Instruments and Methods in Physics Research A*, vol. 725, 2013.

[104] T. Kintscher, "Rapid response to extraordinary events: Transient neutrino sources with the icecube experiment," Ph.D. dissertation, Humboldt-Universität zu Berlin, Mathematisch-Naturwissenschaftliche Fakultät, 2020.

[105] C. F. Tung, "A multimessenger approach to neutrino astronomy," Ph.D. dissertation, Georgia Institute of Technology, 2021.

[106] S. Coenders, "High-energy cosmic ray accelerators: searches with IceCube neutrinos," Ph.D. dissertation, Munich, Tech. U., 2016.

[107] T. Carver, "Time integrated searches for astrophysical neutrino sources using the icecube detector and gender in physics studies for the genera project," ID: unige:120924, Ph.D. dissertation, 2019.

[108] IceCube Collaboration *et al.*, "IceCube Data for Neutrino Point-Source Searches Years 2008-2018," *arXiv e-prints*, 2021.

[109] R. Abbasi *et al.*, "Icecube high-energy starting event sample: Description and flux characterization with 7.5 years of data," *Phys. Rev. D*, vol. 104, 2 2021.

[110] R. Reimann, "Search for the sources of the astrophysical high-energy muon-neutrino flux with the IceCube neutrino observatory," Ph.D. dissertation, RWTH Aachen U., 2019.

[111] C. Bellenghi *et al.*, "A New Search for Neutrino Point Sources with IceCube," *arXiv e-prints*, 2021.

[112] G. Ke *et al.*, "Lightgbm: A highly efficient gradient boosting decision tree," in *Proceedings of the 31st International Conference on Neural Information Processing Systems*, ser. NIPS'17, Long Beach, California, USA: Curran Associates Inc., 2017, ISBN: 9781510860964.

[113] M. Wolf, "SkyLLH - A generalized Python-based tool for log-likelihood analyses in multi-messenger astronomy," in *36th International Cosmic Ray Conference (ICRC2019)*, ser. International Cosmic Ray Conference, vol. 36, 2019.

[114] J. Braun, J. Dumm, F. De Palma, C. Finley, A. Karle, and T. Montaruli, "Methods for point source analysis in high energy neutrino telescopes," *Astroparticle Physics*, vol. 29, no. 4, 2008.

[115] S. S. Wilks, "The large-sample distribution of the likelihood ratio for testing composite hypotheses," *The Annals of Mathematical Statistics*, vol. 9, no. 1, 1938.

[116] P. Virtanen *et al.*, "SciPy 1.0: Fundamental Algorithms for Scientific Computing in Python," *Nature Methods*, vol. 17, 2020.

[117] H. Dembinski and P. O. et al., "Scikit-hep/iminuit," 2020.

[118] F. James and M. Roos, "Minuit: A System for Function Minimization and Analysis of the Parameter Errors and Correlations," *Comput. Phys. Commun.*, vol. 10, 1975.

[119] J. Braun, M. Baker, J. Dumm, C. Finley, A. Karle, and T. Montaruli, "Time-dependent point source search methods in high energy neutrino astronomy," *Astroparticle Physics*, vol. 33, no. 3, 2010.

[120] W. Luszczak, J. Braun, and A. Karle, "A Method for an Untriggered, Time-Dependent, Source-Stacking Search for Neutrino Flares," in *36th International Cosmic Ray Conference (ICRC2019)*, ser. International Cosmic Ray Conference, vol. 36, 2019.

[121] R. Abbasi *et al.*, "Search for Multi-flare Neutrino Emissions in 10 yr of IceCube Data from a Catalog of Sources," *The Astrophysical Journal Letters*, vol. 920, no. 2, 2021.

[122] M. G. Aartsen *et al.*, "Time-Integrated Neutrino Source Searches with 10 Years of IceCube Data," *PRL*, vol. 124, no. 5, 2020.

[123] H. Cramér, "On the composition of elementary errors," *Scandinavian Actuarial Journal*, vol. 1928, no. 1, 1928.

[124] C. R. Harris *et al.*, "Array programming with NumPy," *Nature*, vol. 585, no. 7825, 2020.

[125] A. A. Abdo *et al.*, "Gamma-ray Light Curves and Variability of Bright Fermi-detected Blazars," *The Astrophysical Journal*, vol. 722, no. 1, 2010.

[126] J. Ballet, T. H. Burnett, S. W. Digel, and B. Lott, "Fermi Large Area Telescope Fourth Source Catalog Data Release 2," *arXiv e-prints*, 2020.

[127] Z. Šidák, "Rectangular confidence regions for the means of multivariate normal distributions," *Journal of the American Statistical Association*, vol. 62, no. 318, 1967.

[128] M. G. Aartsen *et al.*, "IceCube-Gen2: the window to the extreme Universe," *Journal of Physics G Nuclear Physics*, vol. 48, no. 6, 2021.

[129] M. G. Aartsen *et al.*, "Search for Sources of Astrophysical Neutrinos Using Seven Years of IceCube Cascade Events," *The Astrophysical Journal*, vol. 886, no. 1, 2019.

[130] K. M. Górski *et al.*, "HEALPix: A Framework for High-Resolution Discretization and Fast Analysis of Data Distributed on the Sphere," *The Astrophysical Journal*, vol. 622, 2005.

[131] A. Zonca *et al.*, "Healpy: Equal area pixelization and spherical harmonics transforms for data on the sphere in python," *Journal of Open Source Software*, vol. 4, no. 35, 2019.

[132] A. Escrivà, "PBH Formation from Spherically Symmetric Hydrodynamical Perturbations: A Review," *Universe*, vol. 8, no. 2, 2022.

[133] M. Oncins, "Constraints on PBH as dark matter from observations: a review," *arXiv e-prints*, 2022.

[134] B. J. Kavanagh, *Bradkav/pbhbounds: Release version*, version 1.0, Accessed: 2023-02-18. [Online]. Available: `https://doi.org/10.5281/zenodo.3538999`.

[135] R. López-Coto, M. Doro, A. de Angelis, M. Mariotti, and J. P. Harding, "Prospects for the observation of Primordial Black Hole evaporation with the Southern Wide field of view Gamma-ray Observatory," *JCAP*, vol. 2021, no. 8, 2021.

[136] E. T. Linton and et al., "A new search for primordial black hole evaporations using the Whipple gamma-ray telescope," *Journal of Cosmology and Astroparticle Physics*, vol. 01, 2006.

[137] D. E. Alexandreas and et al., "New limit on the rate-density of evaporating black holes," *Physical Review Letters*, vol. 71, no. 16, 1993.

[138] M. Amenomori *et al.*, "Search for 10 TeV Gamma Bursts from Evaporating Primordial Black Holes with the Tibet Air Shower Array," in *Proceedings, 24th International Cosmic Ray Conference (ICRC1995): Rome, Italy, August 28 - September 8, 1995*, 1995.

[139] S. Archambault, "Search for Primordial Black Hole Evaporation with VERITAS," *PoS*, vol. ICRC2017, 2018.

[140] Baikal Collaboration *et al.*, "Diffuse neutrino flux measurements with the Baikal-GVD neutrino telescope," *arXiv e-prints*, 2022.

VITA

Pranav Dave was born in India in 1991 and was raised there. He attended Gujarat Technological University as an undergrad where he received a Bachelor of Engineering in Information Technology. After graduating, he moved to Massachusetts for a Master's degree in Physics and contributed to research in computational astrophysics, particularly Type Ia Supernovae. He then moved to Georgia and enrolled in the Ph.D. degree program at Georgia Tech where he began his research in particle astrophysics.